

Universität Stuttgart - Institut für Wasserbau  
**Lehrstuhl für Hydromechanik und Hydrosystemmodellierung**  
Prof. Dr.-Ing. Rainer Helmig  
**Versuchseinrichtung zur Grundwasser- und Altlastensanierung**  
Prof. Dr. rer.nat. Dr.-Ing. András Bárdossy  
Jürgen Braun Ph. D.  
Dr.-Ing. Hans-Peter Koschitzky



Diplomarbeit

# Steam Injection Technique for In Situ Remediation of Chlorinated Hydrocarbons from Low Permeable Saturated Zones - Experiment and Numerical Approach

presented by  
cand.-Ing. Simon Matthias Kleinknecht  
Matrikelnummer: 2292366

Stuttgart, the 18th of January 2011

Examiner: Dr.-Ing. Holger Class, Dr.-Ing. Jennifer Niessner  
Tutor: Dr.-Ing. Holger Class, Dipl.-Ing. Oliver Trötschler

# Contents

<b>List of Figures</b>	<b>V</b>
<b>List of Tables</b>	<b>VI</b>
<b>Nomenclature</b>	<b>VII</b>
<b>List of Acronyms</b>	<b>IX</b>
<b>Abstract</b>	<b>X</b>
<b>1 Introduction</b>	<b>1</b>
1.1 Motivation . . . . .	1
1.2 Aim of this Thesis . . . . .	2
1.3 Outline . . . . .	3
<b>2 Fundamentals</b>	<b>4</b>
2.1 Laws of Dalton, Raoult and Henry . . . . .	4
2.2 Scales and REV . . . . .	5
2.3 Porosity and Saturation . . . . .	5
2.4 Permeability and Darcy's Law . . . . .	6
2.5 Capillary Pressure . . . . .	7
2.6 Heat Transport . . . . .	9
2.7 Properties of Tetrachloroethene . . . . .	11
2.8 Saturation Vapour Pressure . . . . .	12
2.9 Steam Injection Technique . . . . .	13
2.9.1 General Principles . . . . .	13
2.9.2 Effect of Thermal Enhancement on Contaminant . . . . .	16
<b>3 Tank Experiment</b>	<b>18</b>
3.1 Experimental Set-up . . . . .	18
3.2 Sampling and Measurement Devices . . . . .	22
3.2.1 Temperature Measurement . . . . .	22
3.2.2 Steam, Soil Vapour and Groundwater Flow . . . . .	23
3.2.3 Contaminant Concentration Measurement . . . . .	23
3.3 Technical Installations . . . . .	24
3.4 Soil Properties . . . . .	30
3.5 Preliminary Investigations . . . . .	32

3.5.1	Former Experimental Investigation . . . . .	32
3.5.2	Steam Injection Pressure . . . . .	33
3.5.3	Energy Balance Calculations . . . . .	33
3.6	Slugtest . . . . .	35
3.7	Experimental Procedure . . . . .	37
3.7.1	Operating Phases . . . . .	37
3.7.2	Sampling and Parameter Data Acquisition Strategy . . . . .	38
3.8	Experimental Results . . . . .	39
3.8.1	Mass Flow . . . . .	39
3.8.2	Heat Distribution . . . . .	45
3.8.3	Contaminant Recovery . . . . .	51
3.8.4	Water Mass Balance . . . . .	56
3.8.5	Energy Balance . . . . .	58
3.8.6	Tank Heat Loss Estimation . . . . .	62
3.9	Comparison of 1D Numerical Model and Experiment . . . . .	64
3.10	Follow-Up Investigations . . . . .	67
<b>4</b>	<b>Numerical Simulation</b>	<b>68</b>
4.1	MUFTE-UG . . . . .	69
4.2	Primary Variables . . . . .	69
4.3	Mathematical Model of a Non-Isothermal System . . . . .	70
4.3.1	Continuity Equation . . . . .	70
4.3.2	Energy Equation . . . . .	70
4.4	Model Set-up . . . . .	72
4.4.1	Two-Dimensional Approach . . . . .	72
4.4.2	Grid . . . . .	75
4.4.3	Model Parameters . . . . .	75
4.4.4	Initial and Boundary Conditions . . . . .	76
4.4.5	Energy Loss Approach . . . . .	78
4.5	Simulation Results . . . . .	79
4.5.1	Estimates for Input Parameters . . . . .	79
4.5.2	Sensitivities of Input Parameters . . . . .	79
4.6	Comparison of Experiment and Simulation . . . . .	85
4.6.1	Comparison of Heat Distribution . . . . .	85
4.6.2	Effect of Steam Injection Discontinuity . . . . .	89
4.7	Shortcomings of Model . . . . .	91
<b>5</b>	<b>Summary and Conclusion</b>	<b>93</b>
	<b>Bibliography</b>	<b>96</b>
	<b>Appendix</b>	<b>98</b>
<b>A</b>	<b>PCE Concentrations</b>	<b>99</b>
A.1	Groundwater and FLS1 Samples . . . . .	100

---

A.2 Concentration Comparison of SVE and FLS1 . . . . .	102
<b>B Slugtest Data</b>	<b>103</b>

# List of Figures

2.1	Van Genuchten relative permeability - saturation relationship . . . . .	7
2.2	Van Genuchten capillary pressure - saturation relationship . . . . .	8
2.3	Saturation vapour pressure curve of water and <i>PCE</i> . . . . .	12
2.4	Principle of in situ steam injection technique remediation set-up . . . . .	14
2.5	Steam injection methods: <i>steam override</i> & <i>steam sandwich</i> . . . . .	15
2.6	Phase states and equilibrium mechanisms of NAPL-water-air system . . . . .	16
2.7	Determination of azeotropic temperature of PCE-water mixture . . . . .	17
3.1	Side view of tank . . . . .	19
3.2	Top view of tank . . . . .	20
3.3	R&I-Flowchart of steam injection installations . . . . .	25
3.4	R&I-Flowchart of soil vapour extraction installations . . . . .	27
3.5	R&I-Flowchart of experiment . . . . .	28
3.6	Technical installations of the experiment . . . . .	29
3.7	Grain size distribution of <i>site3</i> . . . . .	31
3.8	Grain size distribution of <i>M2</i> and its components . . . . .	31
3.9	<i>PCE</i> concentrations of the saturated zone, taken from LEUBE (2008) [24] . . . . .	32
3.10	Normalized head over time for injection well I1 and I2 . . . . .	36
3.11	Flow rates of steam injection and soil vapour extraction . . . . .	40
3.12	Flow rates and temperature of soil vapour extraction and groundwater . . . . .	40
3.13	Flow rates of steam injection, soil vapour extraction, groundwater and condensate tank . . . . .	42
3.14	Flow rates and temperature of groundwater . . . . .	42
3.15	Temperature trends of saturated, low permeable <i>M2</i> and unsaturated zone . . . . .	45
3.16	Heat distribution plots of remediation experiment (1 – 18d) . . . . .	46
3.17	Heat distribution plots of remediation experiment (28 – 63d) . . . . .	48
3.18	Temperature trends of profile <i>J</i> temperature sensors . . . . .	49
3.19	Effect of buoyancy forces on steam propagation ( $t = 3$ & $28$ d) . . . . .	50
3.20	Percentage distribution of contaminant recovery . . . . .	51
3.21	Contaminant discharge rate and total sum . . . . .	54
3.22	Contaminant concentration of groundwater and condensate tank . . . . .	54
3.23	Contaminant concentration of soil vapour extraction and groundwater . . . . .	55
3.24	Cumulative contaminant recovery . . . . .	55
3.25	Energy input and output quantities . . . . .	58
3.26	Energy input and output . . . . .	59
3.27	Energy loss percentage of single tank parts . . . . .	63

---

3.28	Set-up of 1D model for the tank simulation . . . . .	64
3.29	1D model spreadsheet for the simulation of the tank experiment . . . . .	65
3.30	Comparison of temperature trendlines of 1D model and experiment . . . . .	65
4.1	Phase states and mass transfer processes of a <i>2p2cni</i> model . . . . .	68
4.2	Topview of tank and cross-section . . . . .	73
4.3	Front view of cross-section . . . . .	73
4.4	Numerical steam rate determination approach . . . . .	74
4.5	Grid set-up . . . . .	75
4.6	Refined grid . . . . .	75
4.7	Effects of hydraulic conductivity modification on the heat propagation . . . . .	82
4.8	Effects of porosity modification on the heat propagation . . . . .	82
4.9	Effects of thermal conductivity modification on the heat propagation . . . . .	83
4.10	Effects of model domain energy loss modification on the heat propagation . . . . .	83
4.11	Temperature trend of simulation and experiment . . . . .	86
4.12	Heat distribution: simulation . . . . .	87
4.13	Heat distribution: experiment . . . . .	87
4.14	Heat distribution: simulation . . . . .	88
4.15	Heat distribution: experiment . . . . .	88
4.16	Pressure trend at injection node . . . . .	89
4.17	Effect of steam breakdown on heat distribution . . . . .	90
4.18	Effect of steam breakdown on water saturation . . . . .	90

# List of Tables

2.1	Properties of tetrachloroethene . . . . .	11
2.2	Antoine parameters of water and <i>PCE</i> . . . . .	12
2.3	Effect of temperature increase on properties of PCE . . . . .	16
3.1	Experimental set-up specifications . . . . .	21
3.2	Z-coordinates of temperature sensor profile “J” . . . . .	22
3.3	Physical parameters of used materials . . . . .	30
3.4	Operating phases . . . . .	37
3.5	Experiment flow rates of operating phases . . . . .	38
3.6	Mass balance of remediation experiment . . . . .	57
3.7	Energy balance of remediation experiment . . . . .	60
3.8	Averaged temperatures of porous medium ( $t = 28.81 d$ & $48.25 d$ ) . . . . .	61
3.9	Stored energy in porous medium ( $t = 28.81 d$ & $48.25 d$ ) . . . . .	61
3.10	Heat losses at steady state ( $t = 28.81 d$ ) . . . . .	63
4.1	Phase states and primary variables of the <i>2p2cni</i> model . . . . .	69
4.2	Physical parameters of wetting and non-wetting phase . . . . .	76
4.3	Physical parameters of soils . . . . .	76
4.4	Initial conditions of model domain . . . . .	77
4.5	<i>Dirichlet</i> Boundary conditions at east/west boundary . . . . .	77
4.6	Configuration of <i>M2</i> parameters . . . . .	80

# Nomenclature

Symbol	Meaning	Unit/Dimension
$c_p$	Specific heat capacity	$[\frac{J}{kgK}]$
$h$	Enthalpy	$[J]$
$f$	Factor	$[-]$
$k$	Thermal conductivity coefficient	$[\frac{W}{mK}]$
$k_f$	Hydraulic conductivity	$[\frac{m}{s}]$
$k_r$	Relative permeability	$[-]$
$l$	Characteristical length	$[m]$
$m$	Mass	$[kg]$
$\dot{m}$	Mass flow rate	$[\frac{kg}{s}]$
$x$	Mole fraction	$[-]$
	Van Genuchten parameter	$[-]$
$\dot{n}$	Molar flow rate	$[\frac{mos}{s}]$
$p$	Pressure	$[Pa]$
$q$	Flow rate	$[\frac{m^3}{s}]$
$\dot{q}$	Heat flux	$[\frac{W}{m^2}]$
$r$	Radius	$[m]$
$t$	Time	$[d]$
$A$	Area	$[m^2]$
$B$	General quantity transported with flow	
$D$	Diffusion coefficient	$[\frac{m^2}{s}]$
$Gr$	Gravity number	$[-]$
$H$	Height	$[m]$
$K$	Intrinsic permeability	$[m^2]$
$MW$	Molecular weight	$[\frac{g}{mol}]$
$Nu$	Nusselt number	$[-]$
$Pr$	Prandtl number	$[-]$
$\dot{Q}$	Energy flow rate	$[W]$
$Q$	Energy	$[kJ]$
$Ra$	Rayleigh number	$[-]$
$S$	Saturation	$[-]$
$T$	Temperature	$[K]$
$V$	Volume	$[m^3]$
$X$	Mass fraction	$[-]$
Greek Symbols:		
$\alpha$	Heat transfer coefficient	$[W/m^2K]$
	Van Genuchten parameter	$[\frac{1}{Pa}]$



Symbol	Meaning	Unit/Dimension
$\delta$	Wall thickness	$[m]$
$\epsilon$	Emission ratio	$[-]$
$\lambda$	Thermal conductivity	$[\frac{W}{mK}]$
$\mu$	Viscosity	$[\frac{kg}{sm}]$
$\phi$	Porosity	$[-]$
$\varphi$	Angle	$[^\circ]$
$\rho$	Density	$[\frac{kg}{m^3}]$
$\sigma$	Stefan-Boltzmann constant	$[-]$
$\vartheta$	Reference temperature	$[K]$
$\Gamma$	Boundary of control volume	
$\Omega$	Control volume	
Indices:		
$w$	Water	
$c$	Capillary	
$l$	Loss	
$g$	Gas	
$pm$	Porous medium	
$pw$	Pore water	
$r$	Residual	
	Radiation	
$s$	Soil	
$\alpha$	Phase	
$\kappa$	Component	

# List of Acronyms

2p2cni	2 phase 2 component non-isothermal model
3p3cni	3 phase 3 component non-isothermal model
AGL	Above ground level
BC	Boundary condition
C-UZ	Condensate extraction from unsaturated zone
D/C	Discharge
E	Extraction Well
GC-PID	Gas chromatograph-photoionization detector
GW	Groundwater
HDPE	High density polyethylene
I	Injection Well
IWS	Institut für Wasserbau
NAPL	Non aqueous phase liquid
PCE	Perchloroethylene (tetrachloroethene)
SERDP	Strategic Environmental Research and Development Program
SI	Steam injection
SVE	Soil vapour extraction
TCE	Trichloroethylene
VEGAS	Versuchseinrichtung für Grundwasser- und Altlasten sanierung
VZ	Vadose zone

# Abstract

Steam injection is a commonly applied technique to enhance soil vapour extraction for the remediation of contaminants in the subsoil. However, steam propagation is highly dependent on the permeability of the soils. This thesis describes investigations regarding the heat distribution in a low permeable, saturated zone and the contaminant removal efficiency. To this end, a large-scale tank experiment with two distinct steam injection methods was conducted: 1. steam injection in the saturated zone below the low permeable zone (override) and 2. an additional injection into the unsaturated zone (sandwich). The observed heat distribution was compared to 1D and 2D numerical simulations to evaluate reproducibility and applicability for dimensioning of field applications.

The experiment demonstrated the successful heating of the low permeable, saturated layer (thickness of 1.5 *m*) to about 90°C at the top of the layer after 16 days using the steam override method. A constant steamed zone below the low permeable zone was observed. The additional steam injection in the unsaturated zone showed only a limited effect on the heat distribution in the low permeable layer and achieved no significant increase in contaminant removal. A total mass of 3 kg of contaminant (46% of initial amount) was removed from the subsoil. 88% was removed by the soil vapour extraction, 11% by the groundwater outflow and 1% by the extracted condensate from the unsaturated zone. Contaminant concentrations decreased by 99% in the soil vapour extraction and by 85% in the groundwater. A persisting contamination of the saturated zone was evident.

The 1D model was not able to simulate the predominated conductive heating correctly and further model modifications regarding the relevant processes for heat distribution were necessary. The 2D numerical model reproduced satisfactorily the heat distribution in the low permeable, saturated layer for an adapted set of parameters. However, shortcomings resulted from the negligence of the third dimension and the estimation of the heat losses via the boundaries. Hence, the model can not be applied for different configurations of parameters and further investigations and calibration efforts are required.

# 1 Introduction

## 1.1 Motivation

Water is and will always be the most important resource to maintain a living planet. Due to the rising population over the last decades and, therewith, a significant rise in water consumption, it is every day more important to conserve the quantity of the underground water supply, but even more its quality. The main part of our drinking water is gained by the extraction of groundwater out of aquifers in the subsurface. However, aquifers are often endangered by contaminations caused by, e.g. industrial waste or accidents which release hazardous substances into the environment. Once a contamination in the subsurface is detected the legal situation demands actions to re-establish its previous state and prevent further contamination.

The most common contaminants are the so-called non aqueous phase liquids (*NAPL*). *NAPLs* denote mostly chlorinated solvents, aromatics, oils and polyaromatics which are immiscible and low soluble in water. In relation to the density of water one distinguishes between lighter (LNAPL) and denser (DNAPL) *NAPLs*. These show a different behaviour in the subsoil. *LNAPLs* tend to accumulate on the groundwater surface in the aquifer, leaving a trace of residual saturation behind, while *DNAPLs* may penetrate through unsaturated and saturated zones until a confining layer is reached, accumulate there and diffuse slowly into it. This behaviour of *DNAPLs* causes difficulties during an in situ remediation of low permeable layers, hence, different remediation techniques have been developed during the last decades. Comprising for example, *pump and treat*, *soil vapor extraction* (SVE) or thermally enhanced *SVE*.

One of the most promising technique is steam injection into the saturated as well as the unsaturated zones of the subsoil combined with soil vapour extraction to remove the prevailing contaminants. Steam has proven as a very efficient way of injecting energy into subsoil. The purpose is to heat the subsoil and, thereby, enhance the remediation. Hence, the heat distribution in the subsoil is of main importance for the remediation processes. My thesis, therefore, addressed in particular the issues of heat distribution in the subsoil.

## 1.2 Aim of this Thesis

This thesis has three major aims. The first part is the realization of an in situ remediation of a tetrachloroethene contamination by means of enhanced soil vapour extraction with the steam injection technique. A former physical model, cf. HIESTER & BAKER (2009) [19], was selected to conduct the large scale experiment in the VEGAS facility.

A specific focus will be on the heating process of a low permeable layer in the saturated zone where convective heat transfer is reduced due to the lower permeability. Further, the necessary steam injection rate (energy input) as well as the time duration of the heating process are of interest. Besides the recovery of the contaminant, the main criterion of the experiment is the maximum temperature at the top of the low permeable layer. The target temperature of 90°C was chosen as the boiling point of the water-tetrachloroethene mixture is at 88°C.

The second main focus will be on the build-up of a two-dimensional, two-phase, two-component, non-isothermal model to simulate the heat distribution observed in the experiment. The third aim is the comparison of the heat distribution of the experiment with the results of the two dimensional numerical simulation and a one dimensional numerical model which was set up by GUIDRY (2010) [15]).

The distinct aims can be listed as follows:

- 3D experiment to monitor the heating efficiency of the low permeable zone
  - Applied steam injection methods: *override* and *sandwich*
  - Variation of fluxes to enhance the recovery
- Comparison of the steam injection methods for prediction of:
  - Heat propagation
  - Remediation time
- Remediation efficiency control
  - Reduction of emissions
  - Mass removal
- Build-up of 2D numerical model
- Comparison of heat distribution of experiment with
  - 1D numerical model
  - 2D numerical model

---

## 1.3 Outline

This thesis is divided into three main parts, namely fundamental comments (Ch. 2), the experiment (Ch. 3) and the numerical simulation (Ch. 4).

Chapter 2 provides an overview of the definitions of physical and thermodynamical quantities which are the theoretical background for processes occurring during the experiment. These theoretical considerations will form the basis for the numerical model. In addition, physical and chemical key parameters of tetrachloroethene as well as principal methods of steam injection as a remediation technique are given and explained in detail.

Chapter 3 addresses the tank remediation experiment including description of the set-up parameters, the procedure and the discussion of the results.

The numerical simulation is depicted in Chapter 4. The set-up of the numerical model considering key parameters, primary variables and balance equation is explained and the results gained from the simulations are discussed.

Finally, a summary and the conclusions gained from this thesis (Ch. 5) complete the work.

## 2 Fundamentals

In order to describe and analyze the complex physical processes and align soil remediation by heat treatment, it is necessary to introduce certain concepts such as a description of the system on a specific scale. The scale is based on a predefined degree of abstraction and characterizes the accuracy of the reproduction of processes. The experiment and the numerical simulation are based on thermodynamical, physical and mathematical concepts and definitions which are partly introduced in this chapter. For further information on thermodynamic definitions, cf. BAEHR AND KABELAC (2010) [5]. BEAR AND CHENG (2010) [7] give detailed insight on fundamentals necessary for groundwater flow and contaminant transport modelling.

### 2.1 Laws of Dalton, Raoult and Henry

#### Dalton's Law

DALTON discovered in 1805 that the pressure of a gas mixture is equal to the sum of the partial pressures when ideal gases are considered. In the majority of cases the gas phase of a multiphase system consists of various gas components. DALTONS's law is then written as

$$p_g = \sum_{\kappa} p_g^{\kappa}. \quad (2.1)$$

#### Laws of Raoult and Henry

In multiphase systems a state of equilibrium is reached after a certain time for each component in each phase. This follows the definition of the *thermodynamic equilibrium*. At any point in time, the concentration of a substance in the gas phase can be described by means of its partial pressure  $p_i^{\kappa}$ , following the ideal gas law. The total gas phase pressure can be determined following RAOULT (Eq. 2.2) or HENRY (Eq. 2.3), respectively.

$$p_g = \sum_{\kappa} p_{sat}^{\kappa} x^{\kappa} \quad (2.2)$$

$$p_g = \sum_{\kappa} H_{\alpha}^{\kappa} x^{\kappa} \quad (2.3)$$

Where  $p_{sat}^{\kappa}$  denotes the saturation vapour pressure of the component,  $H_{\alpha}^{\kappa}$  the HENRY coefficient of the component  $\kappa$  in phase  $\alpha$  and  $x^{\kappa}$  its mole fraction. Generally, RAOULT's law can be applied to mixtures of chemically similar components. However, real mixtures show a deviation from the ideal behaviour and, therefore, RAOULT's law is only

valid for  $x^\kappa \rightarrow 1$ . Hence, HENRY's law has to be introduced and has to be applied for  $x^\kappa \rightarrow 0$ .

## 2.2 Scales and REV

A porous medium is defined as a portion of space that is occupied by a number of phases of which at least one is a solid. The space within the porous medium which is not occupied by the solid matrix is called void space or pores and filled with one or more fluids or gases (BEAR AND CHENG (2010) [7]). As already mentioned above, it is not possible to consider every process in every single pore of the porous medium due to differences in geometry even over small distances and the overwhelming complexity. Therefore, processes in a porous medium have to be considered on different scales, for example the molecular scale, the microscale or the local scale, depending on which mechanisms are of interest. On the local scale, a continuum approach is applied in which micro-scale parameters of the porous medium are integrated over a REV (Representative Elementary Volume). This yields an averaged flow description. The size of a REV has to be larger than the size of the heterogeneity but also small enough for spatial variations of the considered properties. This leads to averaged macroscopic values such as the porosity  $\phi$  and saturation  $S_\alpha$ , cf., for example, HELMIG (1997) [16].

## 2.3 Porosity and Saturation

Porosity  $\phi$  denotes the pore space of the porous media available for the fluids and gases. It is defined as the ratio of the pore volume  $V_{Pore}$  to the entire volume of the porous media  $V$ .

$$\phi = \frac{V_{Pore}}{V} \quad (2.4)$$

The saturation is defined as the ratio of the fluid volume  $V_{Fluid}$  to the volume of the pore medium. The term saturation has to be introduced because a determination of the exact spatial distribution of a fluid in the porous medium is not feasible. If more than one phase  $\alpha$  is present in the *REV*, the saturation of phase  $\alpha$  is defined in the following way:

$$S_\alpha = \frac{V_\alpha}{V_{Pore}}. \quad (2.5)$$

Considering more than one phase in the REV results in the constraint:

$$\sum_{\alpha} S_\alpha = 1 \quad (2.6)$$

Various material laws, e.g. relative permeability-saturation relation, do not refer to the saturation  $S_\alpha$ , but to the effective saturation  $S_{e,\alpha}$  denoted as the portion of a fluid displaceable by hydrodynamical processes.

$$S_{e,\alpha} = \frac{S_\alpha - S_{\alpha r}}{1 - S_{\alpha r}} \quad (2.7)$$



Residual saturation can be explained as follows. If a fully water saturated porous media is drained by a non-wetting fluid, e.g. a NAPL, a displacement of the entire amount of water can not be achieved as water is trapped in tiny pores by capillary pressure. The remaining amount of the not displaceable water denotes residual saturation. Furthermore, if the injected non-wetting fluid then is displaced by water also residual saturation remains in the porous media. The processes responsible for this behaviour are discussed in detail in HELMIG (1997) [16]. This explains the definition of the effective saturation  $S_{e,\alpha}$ .

## 2.4 Permeability and Darcy's Law

The permeability also denoted as hydraulic conductivity, characterizes flow behaviour of fluids in a porous medium or hydraulics, respectively. It was introduced by DARCY in 1856 and is defined as the ease with which fluids can move through pore spaces. The general DARCY equation is defined as

$$v = -k_f \nabla h, \quad (2.8)$$

where  $v$  is the velocity in  $[\frac{m}{s}]$ ,  $k_f$  the proportionality factor in  $[\frac{m}{s}]$  and  $\nabla h$  the hydraulic gradient  $[\frac{m}{m}]$ .

Equation (2.9) demonstrates, that the hydraulic conductivity is not only a soil parameter but also depends on the fluid itself.

$$k_f = \mathbf{K} \frac{\rho g}{\mu} \quad (2.9)$$

Where the intrinsic permeability  $K$  [ $m^2$ ] is a property of the soil and the density  $\rho$  and the dynamic viscosity  $\mu$  of the fluid.

DARCY's law (Eq. 2.8) is applied to calculate the flow of a fluid in a porous medium. However, considering multiphase flow one has to modify Equation (2.8) taking into account the resistance one fluid has on the mobility of the other(s). This implies the definition of the relative permeability which can be introduced as a reduction factor of the permeability in DARCY's law.  $k_{r,\alpha}$  varies between 0 and 1 at which a single phase condition is determined by  $k_{r\alpha} = 1$ . The extended form of DARCY's law is then written as

$$v_\alpha = \frac{k_{r,\alpha}}{\mu_\alpha} \mathbf{K} \cdot (\nabla p_\alpha - \rho g). \quad (2.10)$$

It is common to replace  $\frac{k_{r,\alpha}}{\mu_\alpha}$  by  $\lambda_\alpha$  which is denoted as the mobility of the fluid.

Considering two-phase flow, various approaches to quantify the relative permeability-saturation relation can be found in the literature. The approach developed by VAN GENUCHTEN is among the most famous and also implemented into the numerical

model introduced in Chapter 4. Relative permeability - saturation relationship is determined following two equations, one for the wetting (Eq. 2.11) and one for the non-wetting (Eq. 2.12) phase, respectively.

$$k_{r,w} = \sqrt{S_e} \left[ 1 - (1 - S_e^{1/m})^m \right]^2 \quad (2.11)$$

$$k_{r,n} = (1 - S_e)^{\frac{1}{3}} \left[ 1 - S_e^{1/m} \right]^{2m} \quad (2.12)$$

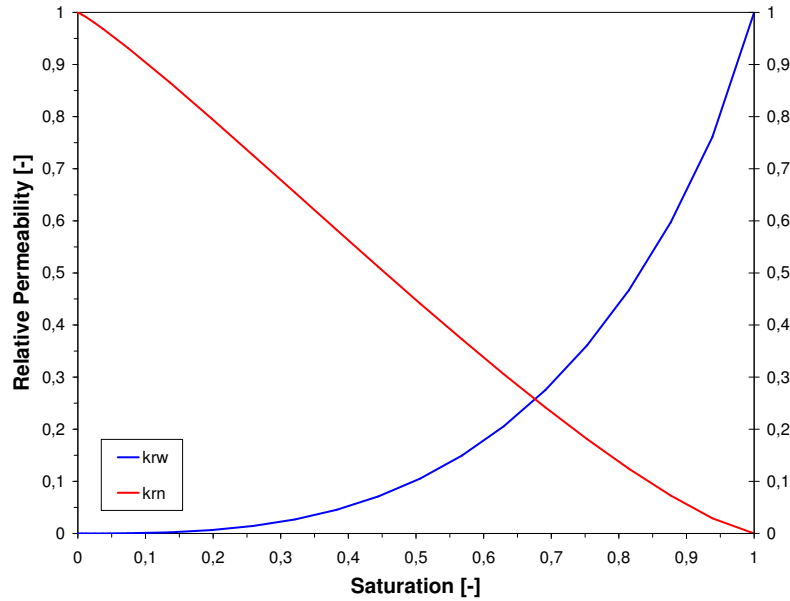


Figure 2.1: Relative permeability - saturation relationship for VG-parameters  $n = 6$ ,  $\alpha = 0.6$  and  $S_{w,r} = 0.19$  (porous medium (*site 3*) of saturated and unsaturated zone; cf. TROETSCHLER ET AL. (2004) [32])

## 2.5 Capillary Pressure

The presence of immiscible fluids in a state of equilibrium within, e.g. a capillary tube, results in a pressure difference between the wetting and the non-wetting phase. This behaviour can be explained by the effect of a fluid to minimize its surface in order to be in a state of minimized free energy. The resulting pressure difference between the fluid that occupies the *concave* side of the interface and the one that occupies the *convex* side is defined as capillary pressure.

$$p_c = \frac{2\gamma_{wn}\cos\Theta}{R} \quad (2.13)$$

where  $\gamma_{wn}$  denotes the interfacial tension between the fluids,  $\cos\Theta$  the contact angle and  $R$  the tube's radius. The wetting-phase tends to be as close to the solid as possible.

In contrary the non-wetting phase minimizes its contact with the soil surface.

$$p_c = p_{non-wetting} - p_{wetting} \quad (2.14)$$

In porous media, one relies on constitutive relationships in order to determine capillary pressure on a local scale. The saturation of the wetting phase is of importance in this aspect as a result of the affinity of the wetting phase to the solid matrix. As a result of this, for small saturations, the wetting phase accumulates first in the narrow pores before occupying the larger ones and vice versa considering the non-wetting phase. Consolidating this observation with Equation (2.13), one can state that for low wetting phase saturation the capillary pressure is accordingly high because of the smaller pore radius.

An approach for the determination of the capillary pressure as a function of the wetting phase saturation on a local scale was developed by, e.g. VAN GENUCHTEN following,

$$p_c = \frac{1}{\alpha} \left( S_e^{-\frac{1}{m}} - 1 \right)^{\frac{1}{n}}. \quad (2.15)$$

$S_e$  denotes the effective saturation (2.7),  $n$  expresses the uniformity of the soil (a high value of  $n$  characterizes an uniform soil) and  $\alpha$  is considered a scaling parameter of the capillary pressure's magnitude. The correlation between  $n$  and  $m$  follows  $m = 1 - \frac{1}{n}$  (CLASS (2001) [10]).

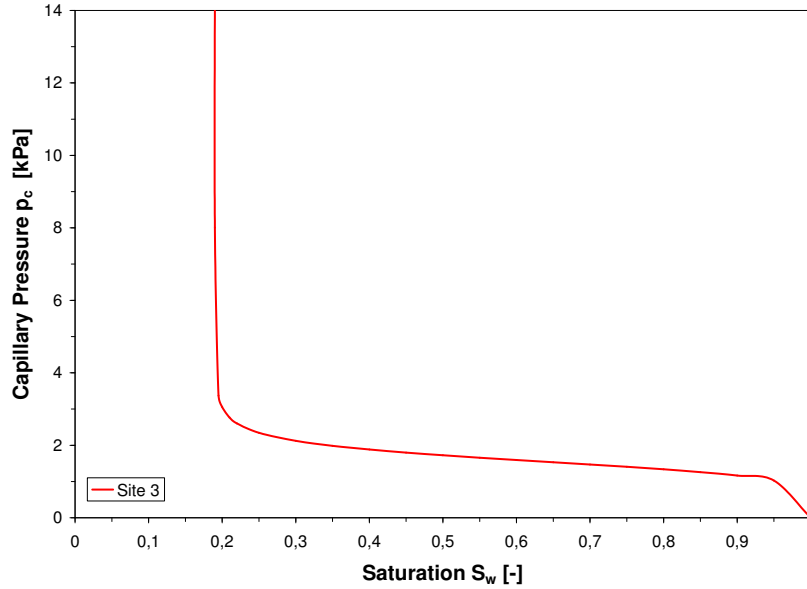


Figure 2.2: Capillary pressure - saturation relationship for VG-parameters  $n = 6$ ,  $\alpha = 0.6$  and  $S_{w,r} = 0.19$  (porous medium (*site 3*) of saturated and unsaturated zone; cf. TROETSCHLER ET AL. (2004) [32])

## 2.6 Heat Transport

The main interest of this thesis lies on heat transport in the aquifer and the low permeable zones. The relevant processes, concerning this matter, are introduced in the following. Heat describes the energy transferred over the system boundary. It is forced only by a temperature gradient between the system and the environment, cf. BAEHR AND STEPHAN (2010) [6]. Considering heat transport, one distinguishes between heat conduction, convection and radiation. In an aquifer heat is distributed mainly by conduction, through fluids and the soil matrix, and convection, i.e. flow of fluids. Whereas in solid matter heat can only be transported by conduction. In general, radiation can be neglected in porous media. Radiation and convection are considered in order to estimate heat losses via the tank walls. Concerning heat transport, absolute temperature  $T$  in most cases plays a minor role, and is replaced by the temperature difference

$$\vartheta = T - T_0 \quad (2.16)$$

where  $t_0$  denotes the reference temperature and can be chosen independently. Setting the reference temperature to  $T = 273.15\text{K}$ , corresponding to  $0^\circ\text{C}$ , is convenient to use the temperatures in  $^\circ\text{C}$ .

### Heat Conduction

Heat is transferred by adjoining molecules as a result of a temperature gradient in the matter. Hence, heat conduction in fluids and solids is of higher importance than in gases due to the smaller intermolecular distance. This results in a heat flux defined by FOURIER written as

$$\dot{q} = -\lambda \nabla \vartheta. \quad (2.17)$$

The factor  $\lambda$  is a material property influenced by temperature  $\vartheta$  and pressure  $p$ .

To determine the thermal conductivity of a porous medium, different calculation approaches exist. The approach by SOMERTON (1974) [31] based on a root function was chosen also to be implemented in the numerical simulation following

$$\lambda_{pm} = \lambda_{pm}^{S_w=0} + \sqrt{S_w} (\lambda_{pm}^{S_w=1} - \lambda_{pm}^{S_w=0}), \quad (2.18)$$

where  $\lambda_{pm}^{S_w=1}$  and  $\lambda_{pm}^{S_w=0}$  denote thermal conductivity of the porous medium at fully saturated and unsaturated condition, respectively.

### Heat Convection

Heat convection is based on transport induced by macroscopical movement of a fluid, cf. BAEHR AND STEPHAN, 2010 [6]. It has to be differentiated between free and forced movement. Free fluid movement is a result of buoyancy because of the difference in

density generated by the different temperatures within the fluid. Whereas forced convection is caused by external forces such as pumps, turbines or phase transformations, e.g. boiling. The considered heat flux  $\dot{q}$  [ $\frac{W}{m^2}$ ] at a wall then can be determined by

$$\dot{q} = \alpha(\vartheta_{Wall} - \vartheta_{Fluid}). \quad (2.19)$$

Equation (2.19) introduced the heat transfer coefficient  $\alpha$  as a function of the fluid properties, the fluid flow and the geometry. The heat transfer coefficient can be calculated by the correlation of NUSSELT.

$$Nu = \frac{\alpha l}{\lambda_i} \quad (2.20)$$

With the dimensionless Nusselt number  $Nu$ , the thermal conductivity of the fluid  $\lambda_{Fluid}$  [ $\frac{W}{mK}$ ] and the characteristic length  $l$  [ $m$ ]. The determination of the Nusselt number  $Nu = f(Pr, Gr)$  is based on empirical approaches and can be calculated by means of the Grashof number and the Prandtl number (2.22). The product of Grashof number and Prandtl number is also known as Rayleigh number (Eq. 2.21),

$$Ra = Gr Pr = \frac{\beta_{Fluid} g (\vartheta_{Wall} - \vartheta_{Fluid}) l^3}{\nu^2} Pr, \quad (2.21)$$

where  $\beta_{Fluid}$  for ideal gases follows  $\beta_{Fluid} = \frac{1}{T_{Fluid}}$ . Prandtl number for the corresponding fluid parameters is defined as

$$Pr = \frac{\eta c_p}{\lambda}. \quad (2.22)$$

## Heat Radiation

The main difference between heat radiation and conduction/convection is the fact, that no matter is needed to transport the heat. Further it is determined by the emissivity of the participating bodies, radiating electromagnetically. The emission of a radiating solid body is limited by its thermodynamic temperature. The maximal heat flux, radiating from the surface of a body, has been defined by STEFAN & BOLTZMANN, cf. BAEHR AND STEPHAN (2010) [6] in the following way

$$\dot{q} = \sigma T^4, \quad (2.23)$$

where  $T$  [ $K$ ] denotes the thermodynamic temperature of the body. The universal Stefan-Boltzmann constant is defined  $\sigma = (5.67040 \pm 0.00004) \times 10^{-8}$  [ $\frac{W}{m^2 K^4}$ ]. A body which reaches the maximum of Equation (2.23) is called full radiator. Not only radiating, but also absorbing perfectly, it can not be exceeded by another body with the same temperature. This fact introduces the emission ratio  $\epsilon \leq 1$  as a function of material properties, which reduces the radiation for a real body, cf. Eq. (2.24).

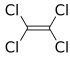
$$\dot{q} = \epsilon(T) \sigma (T_1^4 - T_2^4) \quad (2.24)$$

## 2.7 Properties of Tetrachloroethene

Tetrachloroethene (*PCE*) denotes a chlorinated hydrocarbon solvent. Commercially used as dry cleaning or degreasing agent, as a solvent for gases and fats and as a heat-transfer medium, for example. At normal conditions, *PCE* is liquid and highly volatile. The importance of *PCE* as an industrial product reflected in the frequency at contaminated industrial sites and, therefore, ranks among the main contaminants of groundwater resource. It is furthermore classified as a *DNAPL*. Considering these circumstances, *PCE* was chosen as the representative contaminant in the experiments.

Therefore, the main physical, chemical and thermodynamic properties of *PCE*, of importance for the remediation processes are presented. Property values are taken from the HANDBOOK OF CHEMISTRY AND PHYSICS (2010) [25] and the RISK SCIENCE PROGRAM REPORT (1994) [3].

Table 2.1: Properties of tetrachloroethene

Description	Symbol	Unit	Value
Chemical formula	$C_2Cl_4$		
CAS-NR			127 – 18 – 4
Molecular weight	$MW$	$[\frac{g}{mol}]$	165.8
Density	$\rho$	$[\frac{g}{cm^3}]$	1.6230
Solubility in water	S	$[\frac{mg}{L}]$	287
Vapour pressure at 25°C	$VP$	$[Pa]$	2600
Henry's law constant	$H$	$[\frac{Pa \times m^3}{mol}]$	1460
Boiling point at 1.013 bar	$T_B$	$K$	121.2
Enthalpy of evaporation at 100°C	$\Delta h_v$	$[\frac{kJ}{kg}]$	214.4
Diffusion coefficient in pure air	$D_{Air}$	$[\frac{m^2}{d}]$	0.66
Diffusion coefficient in pure water	$D_{Water}$	$[\frac{m^2}{d}]$	$8.8 \times 10^{-5}$
Distribution coefficient in:			
Groundwater-zone soil	$K_{d,q}$	$[-]$	$K_{oc}^1 \times f_{oc,s}^2$
Vadose-zone soil	$K_{d,v}$	$[-]$	$K_{oc}^1 \times f_{oc,q}^3$

<sup>1</sup>Soil organic carbon partition coefficient  $K_{OC} = 160$ , cf. KARICKHOFF (1981) [21]

<sup>2</sup>Fraction organic carbon in the groundwater-zone soil

<sup>3</sup>Fraction organic carbon in the vadose-zone soil

## 2.8 Saturation Vapour Pressure

Saturation vapour pressure is strongly related to the temperature and of importance considering phase transition (e.g. vaporization and condensation) and phase change (e.g. displacement or change in pressure/temperature). Taking into account these processes, one has to consider that a chemical compound, appearing in the gas and in the liquid phase is dependent on its mole/mass fractions and interaction between the phases. To be able to describe the occurring physical processes, laws of DALTON and RAOULT are consulted, cf. Section 2.1. The saturation vapour pressure curve divides the liquid phase and gaseous phase (steam) area. In Figure 2.3 the saturation vapour pressure curves of water and tetrachloroethene are given, using the ANTOINE equation,

$$p_{sat} = 10^{A - \frac{B}{T+C}}, \quad (2.25)$$

where A, B and C denote empirical parameters. Table 2.2 contains the parameters for water (DORTMUND DATABANK [1]) and *PCE* (REID ET. AL (1987) [29]).

Table 2.2: Antoine parameters of water and *PCE*

Substance	A	B	C
Water	8.07131	1730.63	233.426
PCE	16.1642	3259.29	-52.15

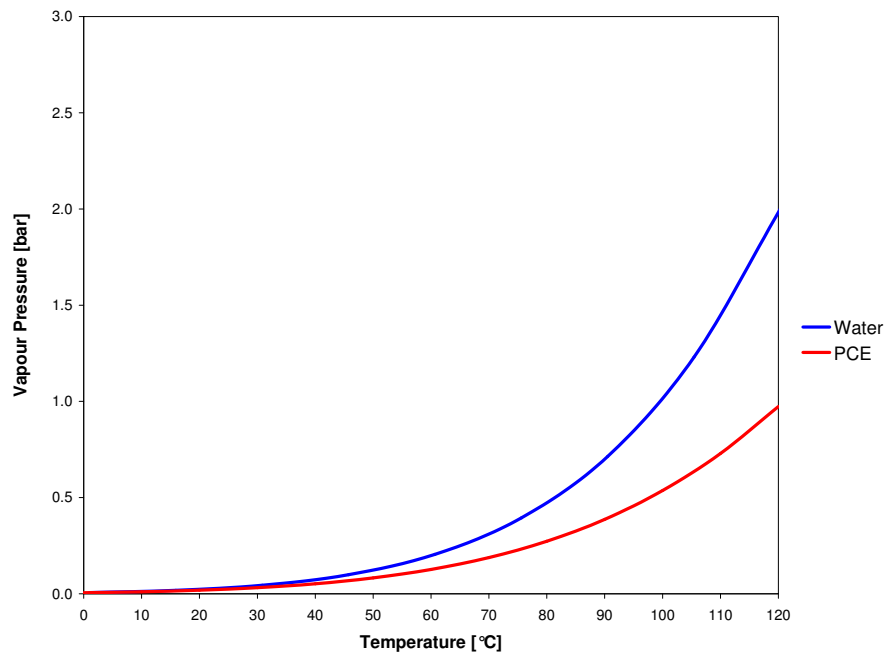


Figure 2.3: Saturation vapour pressure curve of water and *PCE*

## 2.9 Steam Injection Technique

### 2.9.1 General Principles

The injection of steam was developed originally by the petroleum industry to increase the recovery of oils from the ground repositories. Nowadays, steam injection is used as a remediation technique for chlorinated solvents in subsoils, enhancing soil vapour extraction. Taking advantage of the heat capacity of steam to achieve a higher heat input than hot air, for example, providing dissolution, vaporization and mobilization of contaminants and thereby a more efficient recovery.

One essential aspect considering steam injection is the distinct behaviour of the heat propagation in unsaturated and saturated zones due to the influence of buoyancy. In the saturated zone the density of steam and the liquid water of the aquifer differs significantly, whereas in the unsaturated zone the difference of density of steam and ambient air is of minor difference. The vertical-oriented buoyant forces interact with the viscous forces induced by the steam injection (pressure), responsible for the radial propagation of the steam. Considering this, the shape of the steam propagation is dominated by the ratio of the viscous forces to the buoyancy forces. This ratio is defined as the dimensionless gravity number ( $Gr$ ) by VAN LOOKEREN (1983) and has been modified for steam injection into an unconfined aquifer by OCHS (2007) [28].

Generally, the standard remediation set-up consists of soil vapour and/or groundwater extraction wells located at the contaminated zone surrounded by steam injection wells or vice versa. Figure 2.4 gives an example of the principle of a remediation set-up using the steam injection technique, demonstrating the difference the saturated and unsaturated zone have on the propagation. For further information on engineering considerations of remediation set-up, cf. TRÖTSCHLER ET AL. (2004) [32].



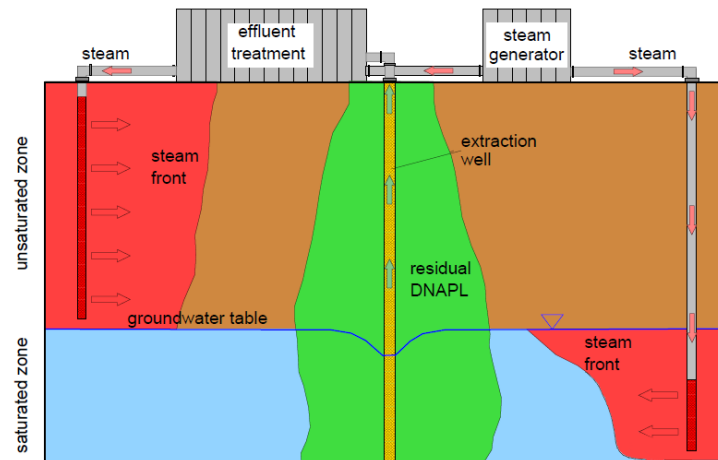


Figure 2.4: Principle of in situ steam injection technique remediation set-up, taken from CLASS (2001) [10]

Former investigations on heat propagation with steam injection, for example FÄRBER (1997) [14] already characterized the processes, occurring in the subsoil where steam is injected. Saturated steam enters the subsoil and condenses as the surrounding sand particles are still cold. This can be explained by the definition of saturated steam: a finite change in temperature is sufficient to trigger condensation. While condensing, the steam transfers its enthalpy of vaporization to the subsoil, heating the sand particles up to boiling point of water.

The relatively high heat transfer during condensation provides a stabilization of the condensation front as steam can only pass regions already at boiling point of water, impeding disequilibrium between the gaseous, liquid and solid phase. The steam is distributed mainly by convection, passing the porous media until it reaches the area where the condensation takes place and the heat is passed to the colder regions. This area is a more or less definable transition zone called steam front. The steam front is characterized by high contaminant concentrations in the vapour phase behind the front and the aqueous phase ahead of the front pushing towards the extraction wells.

Inside of fluids and between sand particles one can observe heat conduction, but only at the steam front, as a temperature gradient is necessary following the definition of FOURIER. In low permeable zones convection is reduced and other processes, such as thermal diffusion and heat conduction are dominating. However, steam injection is limited by the permeability of the subsoil and best applicable to zones of moderate to high permeability. GUIDRY (2010) [15] investigated heat distribution in the low permeable zone by steam injection from below in a two-dimensional experiment, demonstrating applicability but also constrictions.

The experiment includes the investigation of two different steam injection techniques, denoted as *steam override* and *steam sandwich*. Both techniques take aim at the heating of the low permeable saturated zone in order to exceed a temperature of about 90°C within the zone. The relevant processes for heat distribution are heat conduction or diffusive convection, respectively. During *steam override*, steam is injected into the saturated zone below the low permeable zone. The *steam sandwich* includes additionally the steam injection into the unsaturated zone above the low permeable zone. Both methods are illustrated in Figure 2.5.

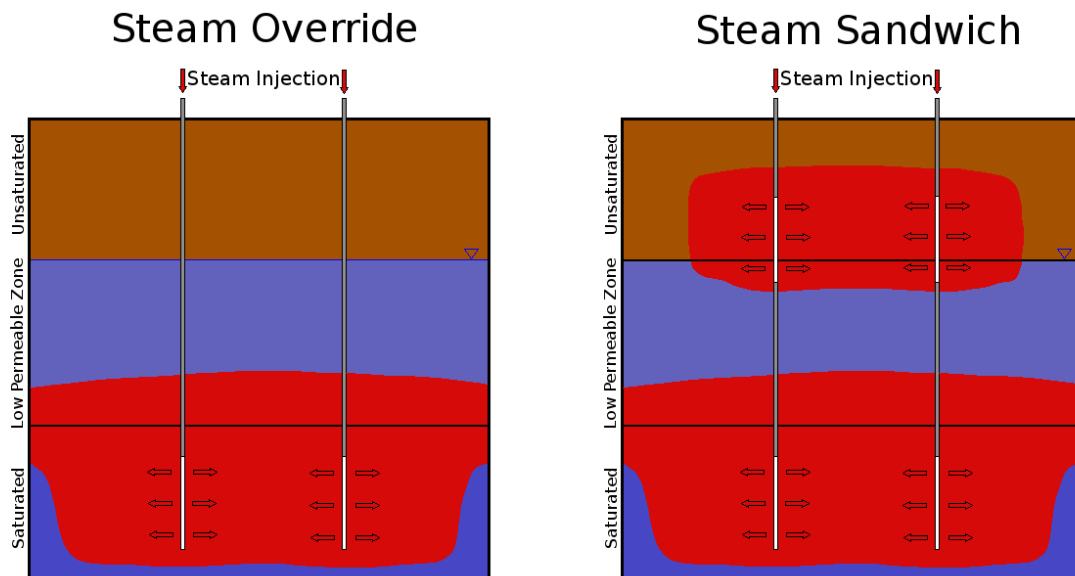


Figure 2.5: Steam injection methods: *steam override* & *steam sandwich*

## 2.9.2 Effect of Thermal Enhancement on Contaminant

The injection of heat has an enormous effect on the key physical and chemical properties of the organic contaminants, benefiting a more or less significant change in fate and transport (EPA (2004) [4]). Figure 2.6 describes the phase transition mechanisms of a NAPL to reach the state of equilibrium, considering three phases and three components.

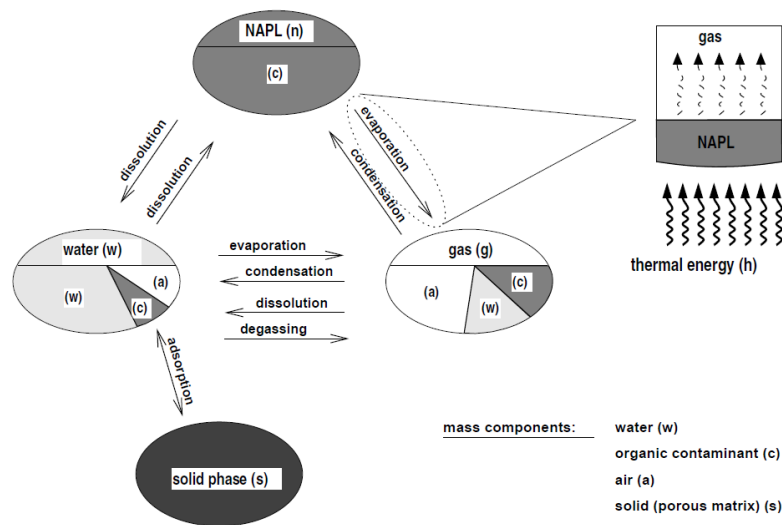


Figure 2.6: Phase states and equilibrium mechanisms of NAPL-water-air system (CLASS (2001) [11])

The properties of *PCE* given in Table 2.1 are generally based on normal conditions, means 25°C. Table 2.3 derived from DAVIS (1997) [13] demonstrates changes in properties of *PCE* at increasing temperature.

Table 2.3: Effect of temperature increase on properties of PCE

Property	Effect
Liquid density	decreases moderately (less than 100 percent)
Vapour pressure	increases significantly (10 to 20 fold)
Liquid viscosity	decreases for $T < T_{boiling}$
Solubility	increases as temperature increases
Henry's coefficient	increases (more likely to volatilize from water)
Partition coefficient	decreases (less likely to partition to organic matter in soil)
Degradation	increases

The mentioned changes in properties present positive effects on the remediation (DAVIS (1997) [13]). For example, liquid viscosity decreases about 1% per 1°C of increased temperature up to the boiling point, enhancing the mobility of *PCE*. Furthermore, as temperature increases, also vapour pressure increases exponentially and *PCE* tends to partition to the gas phase. The mass of chlorinated solvents occupies a larger volume in the gas phase than in the liquid phase, resulting in expansion and advective flow. Solubility in water increases by a factor of two or more and the partitioning from the aqueous phase to the soil is generally decreased at higher temperature.

One of the main benefits which thermal effects have on the remediation progress is the reduced boiling temperature of the mixture of chlorinated solvent and water, featuring heterogeneous azeotropic properties. This is marked by the boiling of the mixture at a constant temperature (azeotropic temperature) without a corresponding change in composition. The azeotropic temperature can be determined by the method of BADGER-MCCABE. The intersection point between the vapour pressure curve of *PCE* and the curve obtained by subtracting the vapour pressure curve of water from the atmospheric pressure curve, determines the azeotropic temperature (cf. Figure 2.7). The azeotropic temperature of a system consisting of water and tetrachloroethene at 101 *kPa* is about 361 to 362 *K*, approximately 88°C (DORTMUND DATA BANK [1]).

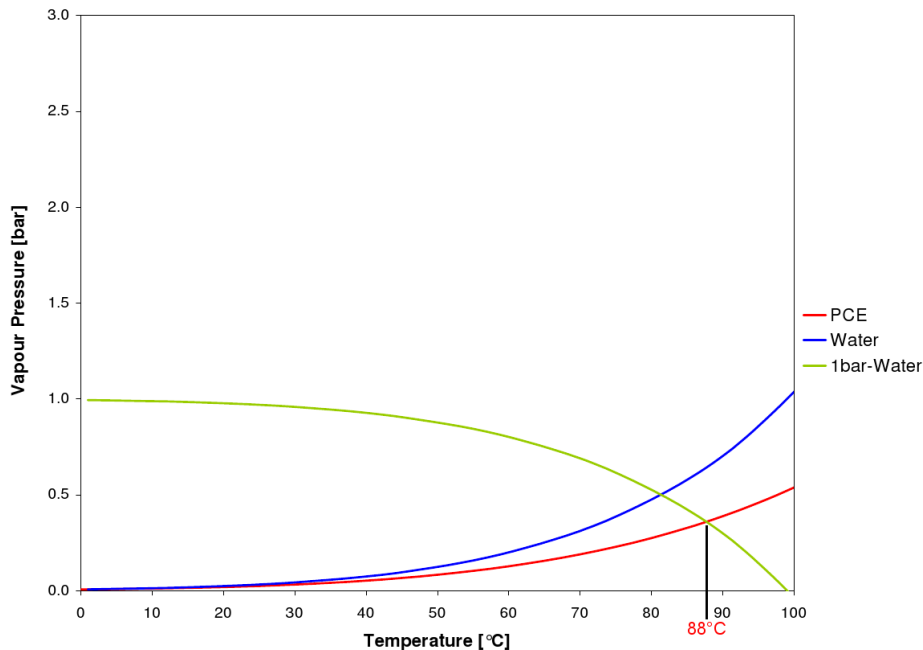


Figure 2.7: Determination of azeotropic temperature of PCE-water mixture

## 3 Tank Experiment

### 3.1 Experimental Set-up

The in situ remediation experiment was realized at the *Versuchseinrichtung für Grundwasser- und Altlastensanierung* (VEGAS) at the *Institut für Wasserbau* of the *University of Stuttgart*. VEGAS provides a large tank which is divided into four separate smaller tanks with different dimensions and aquifer models. The experiment was conducted in a tank that has a length of 6 m, a width of 3 m and 4.5 m of height. The tank is filled with two different soils which differ in grain size (coarse and fine). Different permeabilities are used to represent a low permeable layer enclosed by two high permeable layers. Further, it is equipped with PT100 temperature sensors in two cross-sections and over the entire height to measure the temperature distribution during the experiment. Four steam injection wells ( $1\frac{1}{4}$  in), two in the saturated zone and two in the unsaturated zone, respectively. Furthermore, two soil vapor extraction wells (3 in) are installed.

To provide a groundwater flow, two horizontal wells (inlet and outlet) are located at the far-out ends at the bottom of the tank. Waste water treatment, steam generator, pumping systems, soil vapour extraction system, gas phase chromatograph as well as an activated carbon filter to treat the extracted soil vapour complete the set-up. The temperature monitoring and the gas phase chromatograph are connected to an electronic data processing system. Detailed figures of the top view (Fig. 3.1) and the side view (Fig. 3.2) of the set-up are given.

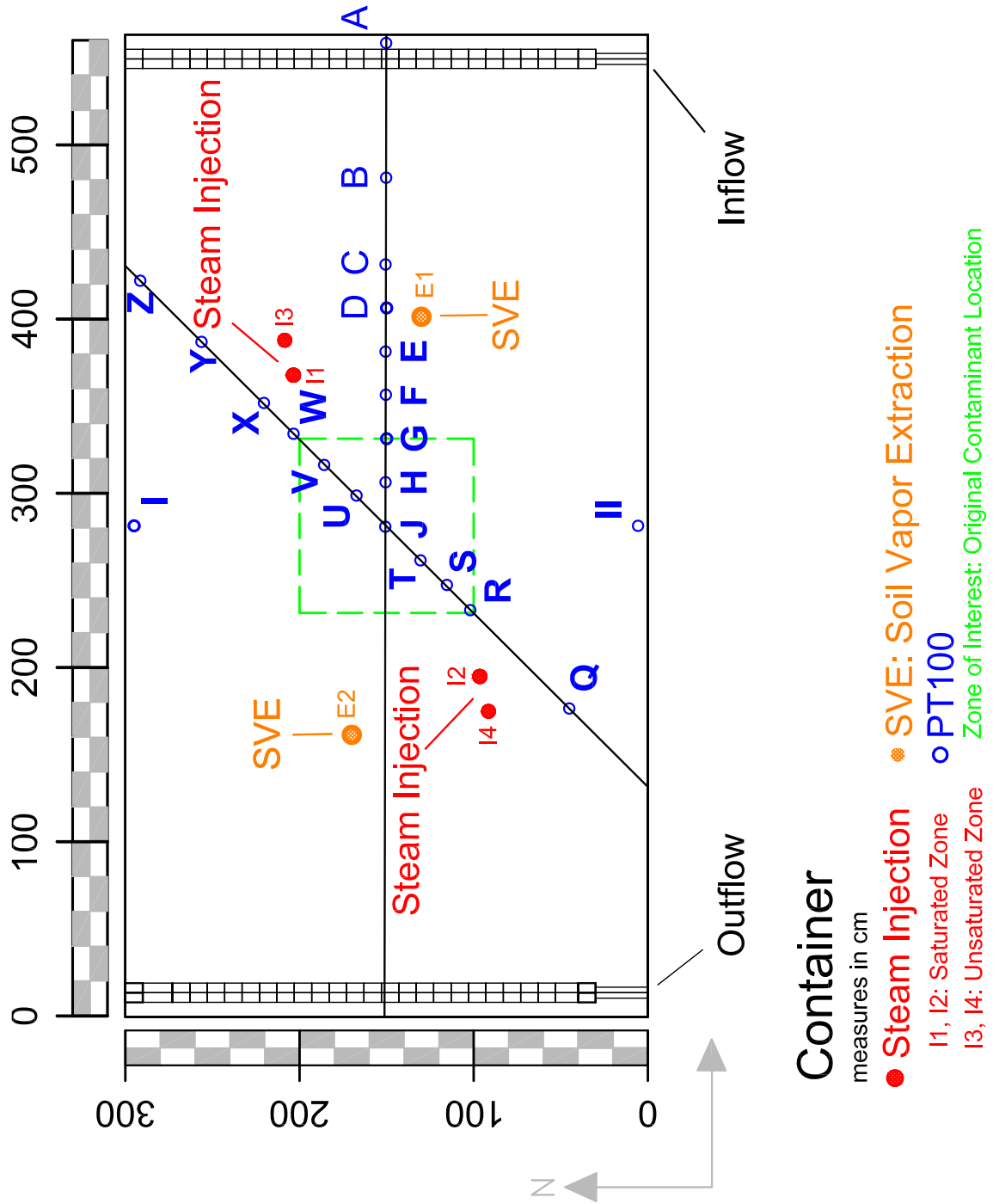


Figure 3.1: Side view of tank

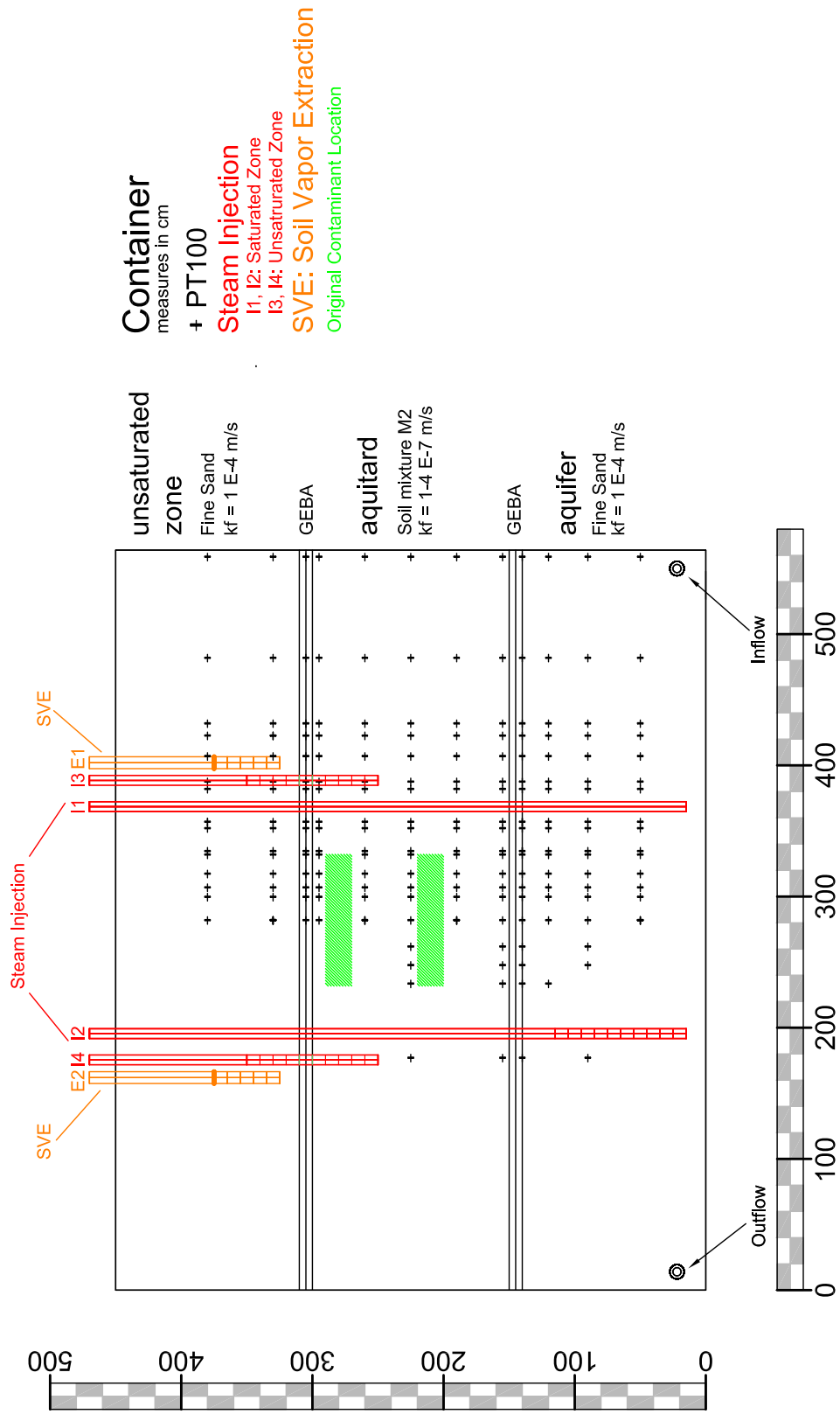


Figure 3.2: Top view of tank

## Injection, Extraction and Groundwater Wells

The term *thermally enhanced in situ remediation* includes different techniques to inject thermal energy into the subsoil. The applied steam injection technique requires wells to inject the steam at the desired location in the subsoil. The installed wells are manufactured from stainless steel and have a diameter of  $1\frac{1}{4}$  in. Two wells (*I1* and *I2*) were pile driven into the saturated zone (aquifer) with a filter screen length of about 1 m, which is located between 0.15 m and 1.15 m of height above ground level. *I3* and *I4* reach into the aquitard/unsaturated zone and its filter screen is located between 2.75 m and 3.75 m above ground level. Detailed information concerning the location can be gained in Figure 3.1 and 3.2. Investigations concerning the heating process of the aquitard conducted by GUIDRY (2010) [15] demand the additional wells *I3* and *I4* in order to reach a temperature of about 90°C at the top of the aquitard.

Former investigations, e.g. BETZ (1998) [8], revealed, that it is necessary to always combine a thermally enhanced in situ remediation with a soil vapour extraction. Therefore, the tank is equipped with two soil vapour extraction wells with a diameter of about 4 in and a filter screen length of 0.5 m at a height of 3.2 m to 3.7 m above ground level. The exact locations are given in Figure 3.1 and 3.2.

At the bottom of the tank two groundwater drainage tubes (inlet and outlet) with a diameter of 4 in are installed. Its purpose is to maintain a constant head boundary condition to simulate an infinite, wide-spread aquifer.

Table 3.1: Experimental set-up specifications

Ground area [ $m^2$ ]	$3 \times 6$ m	18
Height [m]		4.5
Water level [m AGL]		3.1
SVE wells		2
Steam injection wells		4
Horizontal groundwater wells		2
Porous media	Soil type	Mass [kg]
Aquifer	<i>site 3</i>	42970
Transition layers	<i>GEBA</i>	5150
Aquitard	<i>M2</i>	42820
Vadose zone	<i>site 3</i>	42970



## 3.2 Sampling and Measurement Devices

The observation of an experiment is indispensable and, therefore, the tank was equipped with monitoring systems to record the parameters of interest including temperature, contaminant concentration, hydrostatic pressure and flow.

### 3.2.1 Temperature Measurement

To be able to measure the steam front or heat propagation, respectively, 216 temperature sensors (PT100 and temperature receiving element) are installed on a longitudinal semi-axis cross-section and a transversal cross-section with a  $45^\circ$  angle at 12 vertical levels. The temperature sensors are connected to measurement boxes transmitting the amplified signal via a *CAN-Bus* to a computer. The x-y-locations are shown in Figure 3.1 and 3.2. In Table 3.2, one can gain an overview of the altitudinal distribution of the temperature sensors which are the same for every profile, except profiles *Q*, *R*, *S* and *T*, which were installed additionally and only consist of four sensors, installed at 90, 140, 155 and 225 *cm* above the ground level (AGL).

Table 3.2: Z-coordinates of temperature sensor profile “J”

Sensor	Height AGL [cm]
J380	380
J330	330
J305	305
J295	295
J260	260
J225 Q225	225
J190	190
J155 Q155	155
J140 Q140	140
J120	120
J90 Q90	90
J50	50

Further, temperatures of the tank walls as well as the steam injection and soil vapour extraction temperatures at the orifice plates were recorded. Temperatures of the tank front wall were measured once a day at three different heights of the front wall (height

of saturated zone (90 cm), aquitard (225 cm) and unsaturated zone (380 cm)). The model tank is embedded in a thin layer of water between the inner (*HDPE*) and outer wall (stainless steel), serving as a cooling gap without hydraulic connection and heat boundary to the other surrounding tanks. The temperature in the cooling gap was measured and recorded likewise. The temperatures of the walls are required to estimate the heat losses in order to be able to complete the energy balance of the experiment.

### 3.2.2 Steam, Soil Vapour and Groundwater Flow

An exact determination of the steam flow and the extracted soil vapour flow is necessary for mass and energy balancing. As already described in Section 3.3, pressure difference was measured at the orifice plates by an U-tube and can be read in water column which corresponds to millibar. Including the injection pressure and the vacuum, respectively, and the temperature one can calculate the flow rate in kilogram per hour and the energy in kilowatt (EN ISO 5167-1, VDI-WÄRMEATLAS (2006) [20]). While groundwater inflow was detected by the magnetic induction flow meter (*FI-GW*), the outflow had to be metered manually in liters.

Due to the fact that those values were not recorded automatically by a data monitoring system, they were recorded twice a day.

### 3.2.3 Contaminant Concentration Measurement

#### 3.2.3.1 Gas Phase

Contaminant concentrations of the extracted soil vapour were measured and recorded in a time interval of 30 minutes by a process gas chromatograph using a photoionisation detector (*GC-PID*, 001/11/2000, Meta Messtechnische Systeme GmbH). A determined amount of soil vapour is injected by means of the carrier gas (nitrogen) onto the separating column of the gas phase chromatograph. The calibration of the gas phase chromatograph had to be performed in frequent intervals to assure a correct measuring and balance the shifting of the *GC-PID*. The calibration was realized with the contaminants trichloroethene and tetrachloroethene once a week. The detection limit (minimum concentration) of contaminants was set to  $0.1 \frac{mg}{m^3}$ .

#### 3.2.3.2 Liquid Phase

The contaminant was not only recovered from the tank by the extracted soil vapour, but also with the groundwater outflow. Hence, groundwater outflow and *FLS1* samples were taken twice a week and stored in the cooling room (8°C) to determine the contaminant concentration in the groundwater outflow. This was realized by means of a *GC-ECD/GC-FID* (HP 6890 GC System) at the chemical laboratory of *VEGAS*. The concentrations of the groundwater outflow and the *FLS1* are listed in the appendix (A.1)

### 3.3 Technical Installations

The experimental installations are divided into four parts. The tank itself, the steam injection, the soil vapour extraction and the groundwater containment system. Detailed information and dimensions of the tank are given in Section 3.1, while the R&I-Flowcharts of the technical installation are shown in Figure 3.5, 3.3 and 3.4.

- Part I: Steam Injection, Fig. 3.3

Fresh water is filtrated (*F1*) and passes the ion exchanger (*FIAT1*) before entering steam generator (*D1*). The total power consumption of the steam generator of about 48 kW is used to produce saturated steam at a pressure of 4 to 6 bar. Steam is carried through steam tubes to the tank, passing a distribution and measurement system and is injected into the aquifer via the injection wells in the saturated zone (*I1*, *I2*) and in the unsaturated zone (*I3*, *I4*). The steam flow is adjusted by valves (*HV-D*, *HV-I*, *HV-I1* and *HV-I2*) while the pressure reduction valve (*DM-D*) maintains a constant pressure in the system. Measuring and recording of steam temperature (*TIR-I1/I2*) as well as the pressure difference at the orifice plates (*FI-I1/I2*) and the injection pressure at the head of the wells (*PI-I1* to *PI-I4*) provide the data to determine steam flow rate and energy input.

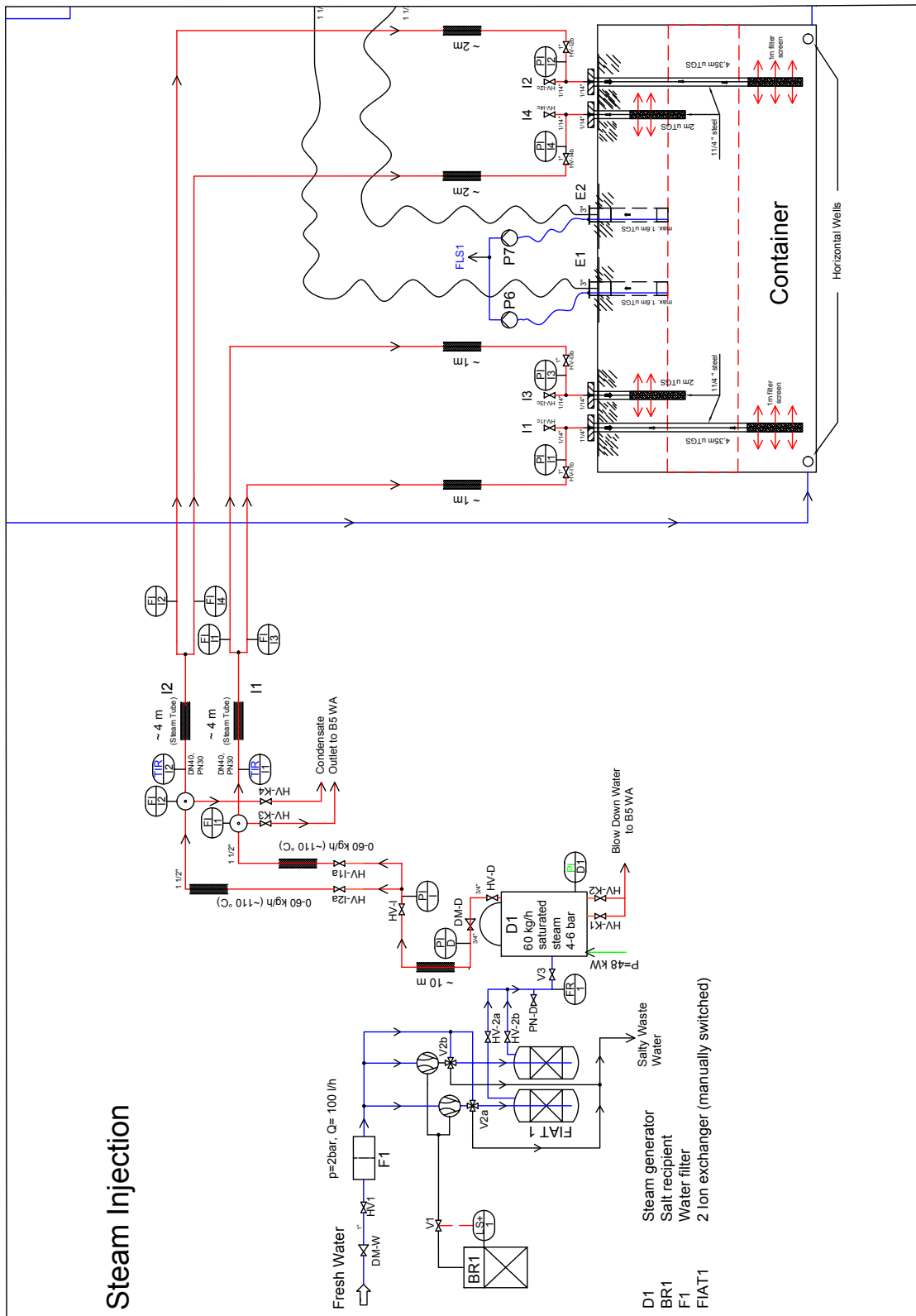


Figure 3.3: R&I-Flowchart of steam injection installations

- Part II: Soil Vapour Extraction, Fig. 3.4  
Soil vapour is extracted via the extraction wells  $E1$  and  $E2$  and carried through hoses, passing the similar distribution and measurement system as for the steam. Afterwards, the heat exchanger ( $WT1$ ) is passed to condense the soil vapour to dewatered hot air before it is mixed with bypass air by the blower ( $C1$ ) and transported to the activated carbon filter ( $FA1$ ). Cooling water is pumped by the pump  $P1$  from the cooling water tank  $B1$  and flows through the heat exchanger in order to enhance the condensation of the extracted soil vapour. The temperature ( $TIR-E1/2$ ), the pressure difference at the orifice plates ( $FI-E1/E2$ ) as well as the vacuum ( $PN-E1/E2$ ), applied by the compressor, are measured and recorded to determine extraction flow rate and energy output. Condensed water from the orifice plates as well as from the heat exchanger runs to the condensate tank ( $FLS1$ ) where the incoming amount is measured by the flow meter ( $FI-K$ ). By adjusting the bypass air valve ( $HV-A$ ) the vacuum can be regulated. Between the heat exchanger and the compressor an additional cycle with a gas phase chromatograph was set up to measure continuously the extracted contaminant concentrations in the soil vapour. Two pumps ( $P6/P7$ ) are installed to pump the condensate from the unsaturated zone to  $FLS1$ .
- Part III: Groundwater Containment System, Fig. 3.5  
Degassed water of the groundwater tank ( $B5$ ) produced by the degassing installation is pumped into the model tank via the horizontal well (*Inflow*) by the groundwater pump ( $P2$ ). After reaching the opposite site of the tank due to the hydraulic gradient, groundwater leaves the tank via the horizontal well (*Outflow*). The water level at the outflow is adjusted by the height of the outflow tank ( $GBW2$ ) operating as gravity flow. The amount of inflow ( $FI-GW$ ), outflow (unit volume per unit time) as well as their temperatures ( $TI-GW1/2$ ) are measured to determine energy input and output. Finally, the discharged water is collected in the tank  $B5 WA$  at the waste water treatment plant before it is purified by an adsorption unit comprising activated carbon filters ( $FA2,3$ ). Afterwards, the purified water can either be dumped into the communal sewage system or collected to be reused in further experiments.

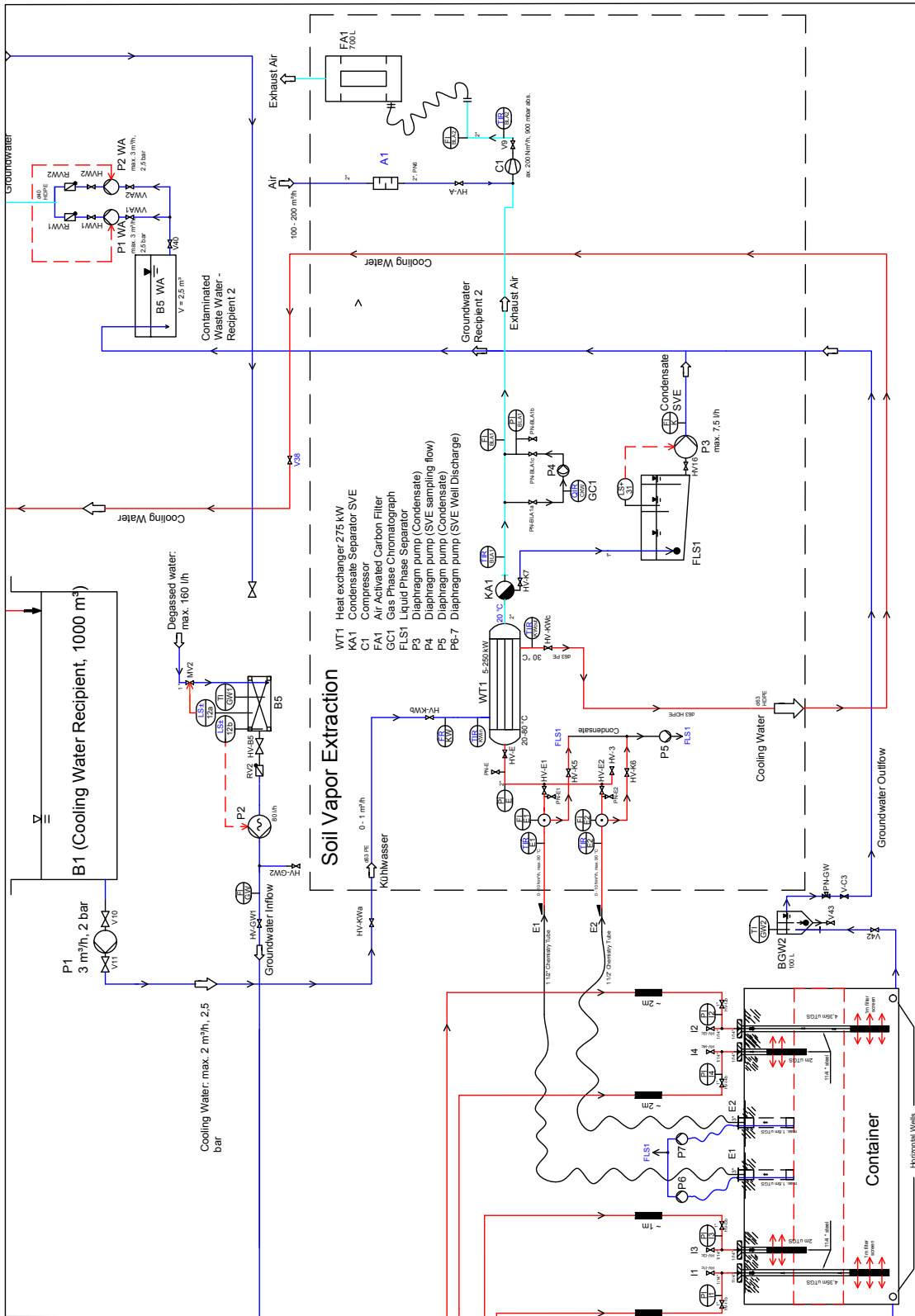


Figure 3.4: R&I-Flowchart of soil vapour extraction installations

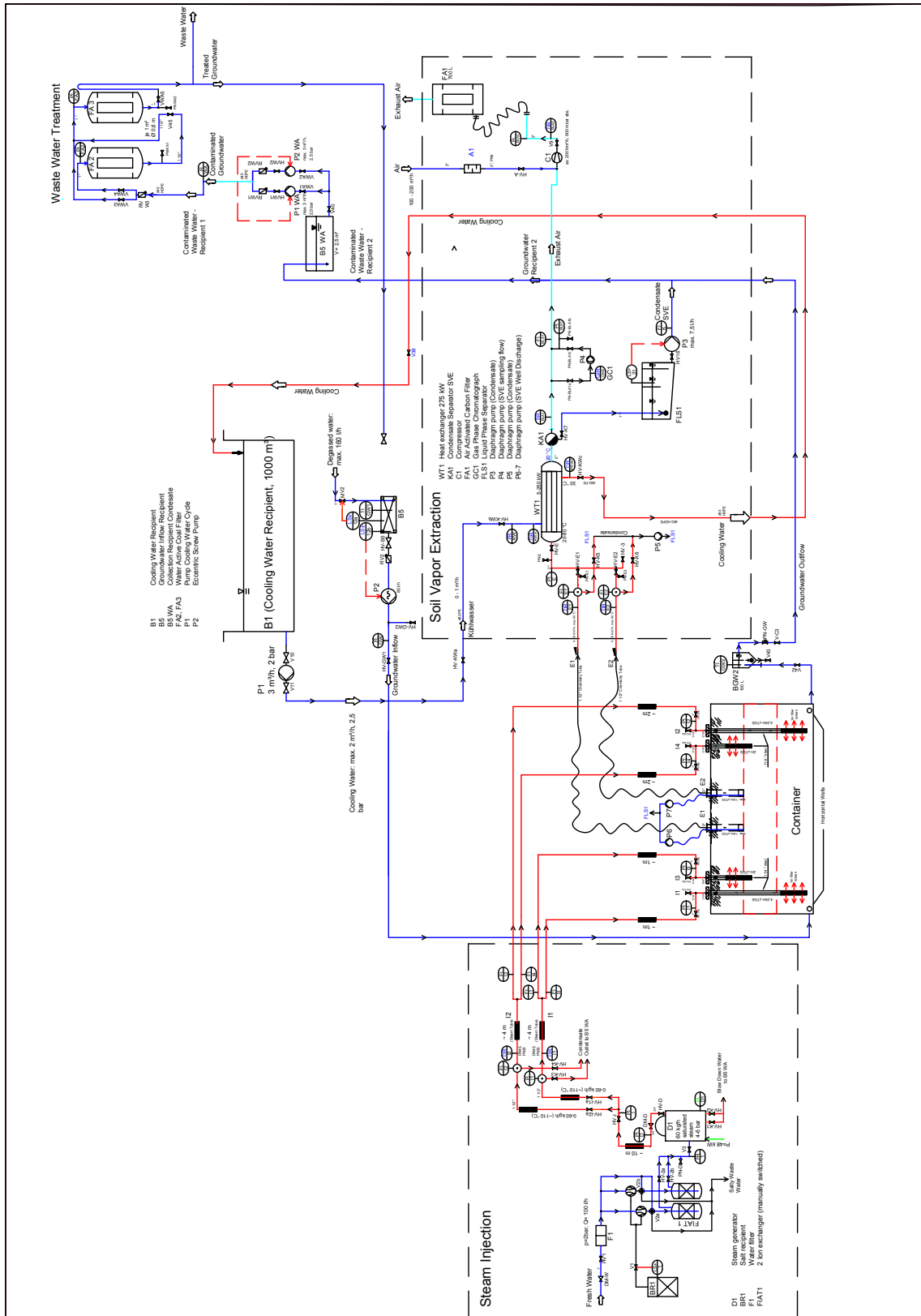


Figure 3.5: R&I-Flowchart of experiment

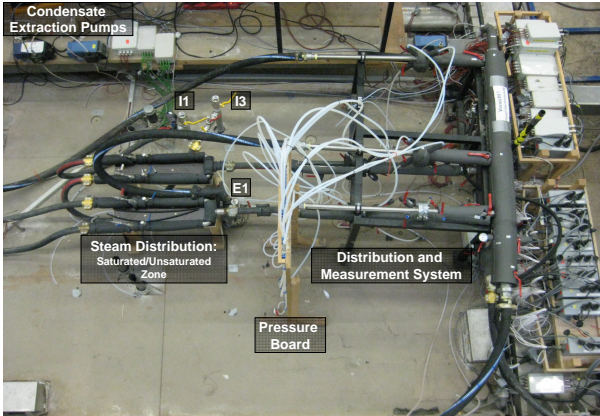
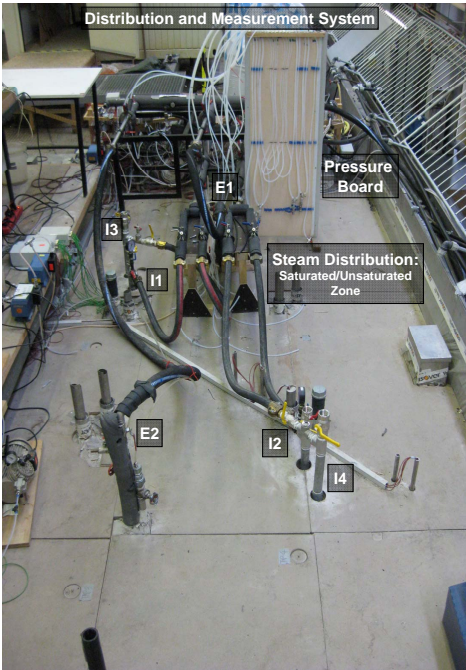


Figure 3.6: Technical installations of the experiment



### 3.4 Soil Properties

The tank was set up to mimic a natural aquifer with a saturated aquitard on top, followed by an unsaturated zone. Due to the fact that filling was realized by depositing one horizontal layer after the other, one can assume that vertical anisotropy of conductivity was caused. LEUBE (2008) [24] stated that the vertical hydraulic permeability is reduced by a factor of 5 - 20 compared to the horizontal hydraulic permeability. All of the three zones, aquifer, aquitard and unsaturated zone have a thickness of 1.5 m. The aquifer zone and the unsaturated zone consist of the soil called *site 3*, whereas the in-between aquitard zone is a mixture of different sands labelled *M2*. The mixture *M2* is a composition of 24% *GEBA*, 16% *Dorsilit*<sup>1</sup> 2500, 40% *Dorsilit* 4900 and 20% *Dorsilit* 10000 to gain a sand mixture with a very low permeability. To avoid eluviation of fine material into the coarser zones, two layers with a height of about 10 cm consisting of the sand *GEBA* separate the *M2* layer from the *site 3* layers. The following Table 3.3 gives an overview over the physical parameters of the embedded materials determined by HIESTER & BAKER (2009) [19].

Table 3.3: Physical parameters of used materials

Soil	Bulk density $\rho_{Bulk}$ [ $\frac{kg}{m^3}$ ]	Porosity $\phi$ [-]	Hydraulic conductivity $k_f$ [ $\frac{m}{s}$ ]	Specific heat capacity $c_p$ [ $\frac{J}{kgK}$ ]
site 3	1680-1730	0.3-0.32	$1.6 - 1.9 \cdot 10^{-4}$	960
M2	1586	0.4	$1 - 4 \cdot 10^{-7}$	920
GEBA	1430	0.46	$1.1 \cdot 10^{-4}$	840

Observations during the experiment and analysis of simulation results suggested a better hydraulic conductivity  $k_f$  of the *M2* soil than measured by HIESTER & BAKER (2009) [19]. GUIDRY (2010) [15] determined the horizontal hydraulic conductivity of *M2* via DARCY's equation in the flume experiment to about  $k_f = 4.6 \cdot 10^{-6} \frac{m}{s}$ . As a result of the significance of hydraulic conductivity concerning heat distribution, a better permeability would result in a faster heat distribution. In Section 4.5.2 of the simulation results, the influence of changes in permeability was investigated by means of simulation runs with altered intrinsic permeability.

Grain size distribution of *site 3* soil, mixture *M2* and the component sands of *M2* are given in the Figures 3.7 and 3.8.

<sup>1</sup>Dorsilit is trademark of *Dorfner Group*, Hirschen, Germany

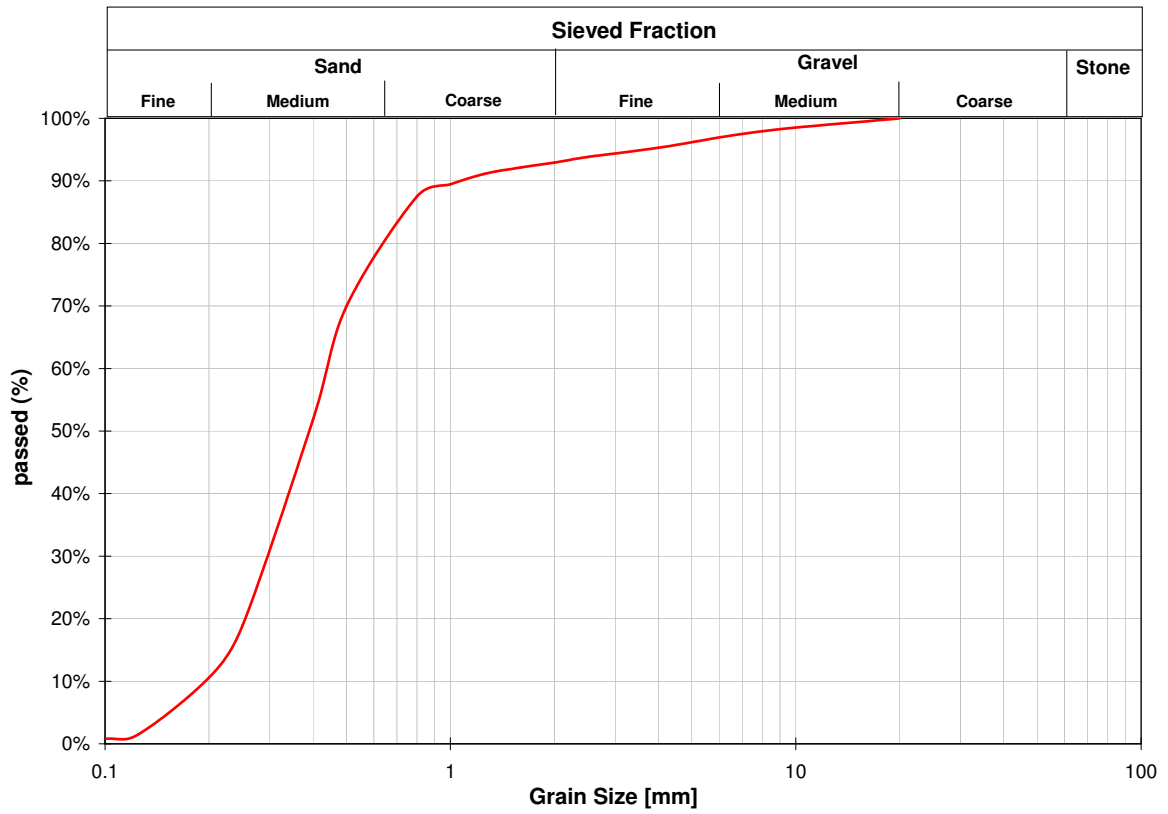


Figure 3.7: Grain size distribution of *site3*

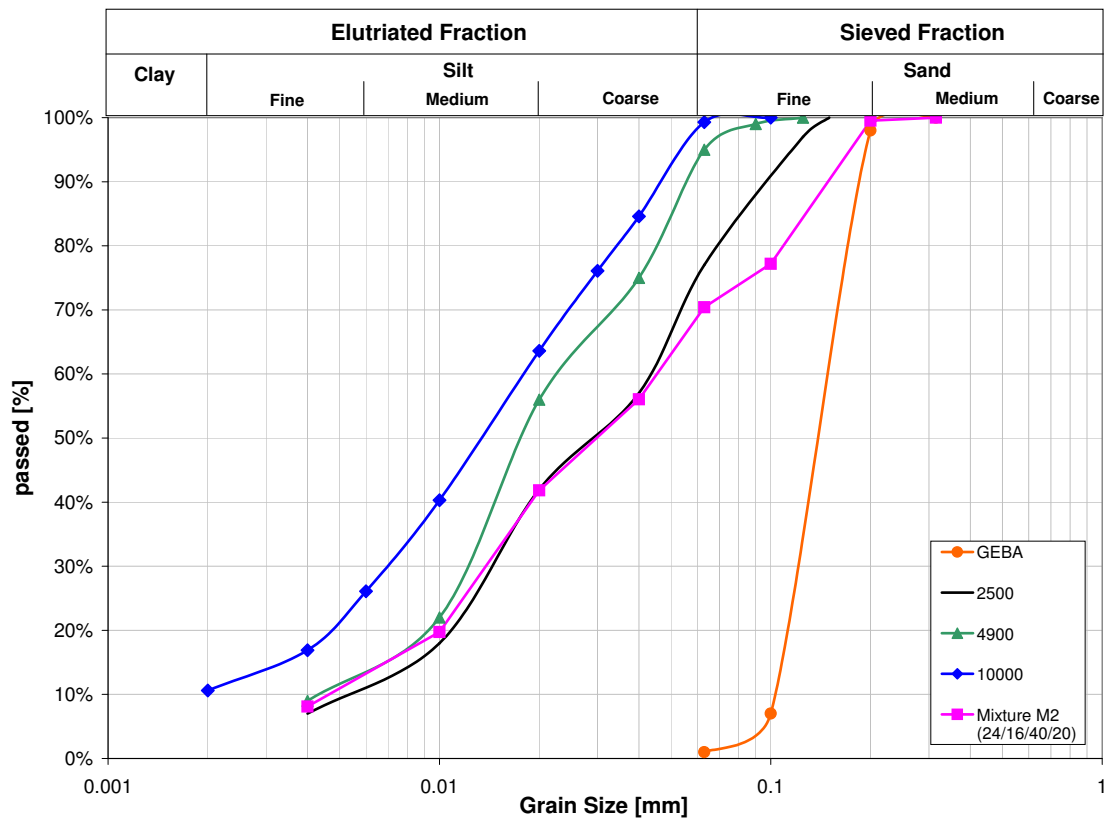


Figure 3.8: Grain size distribution of *M2* and its components

## 3.5 Preliminary Investigations

Prior to the realization of experiments, possible physical limitations and technical expertise have to be taken into account. Furthermore, this section contains the energy balance equations used to evaluate the results of the experiment.

### 3.5.1 Former Experimental Investigation

The tank was set up to conduct various in situ remediation experiments. Prior to the steam drive remediation approach, LEUBE (2009) [24] conducted soil remediation experiments using electrically driven heating elements in order to heat up the subsoil and extract the contaminants. During the experiment a total mass of 20 kg of *PCE* was injected into the low permeable *M2* layer at two different heights (zone of interest (3.2)). The experiment concluded with a total removal of *PCE* 56.4% , hence, a remaining amount of about 8.72 kg in the tank. The concentration in the groundwater outflow was determined to  $7.1 \frac{mg}{l}$ . Measurement of *PCE* concentrations in the saturated zone of the tank at the end of the experiment showed a deposition of the contaminant on the side of the groundwater outflow (Fig. 3.9). *PCE* concentrations exceeding  $100 \frac{mg}{m^3}$  were measured at a height of one meter above the ground in the saturated zone.

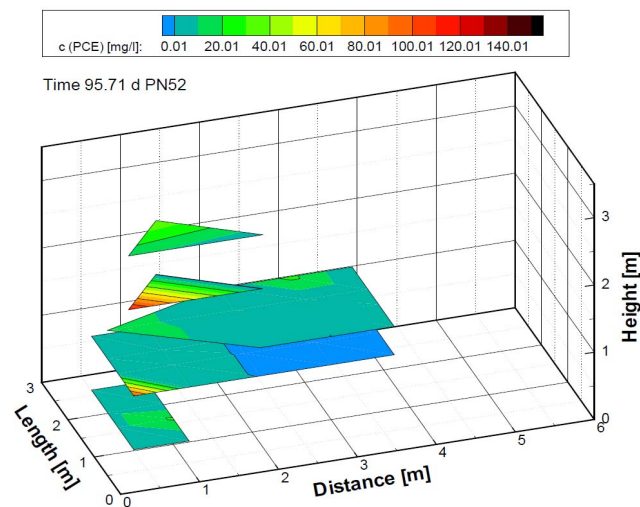


Figure 3.9: *PCE* concentrations of the saturated zone, taken from LEUBE (2008) [24]

This can be explained by contaminant transport with the condensation front towards the walls, which resulted in the displacement of *PCE* towards the margins of the tank. In addition, it is assumed that the contaminant gravitated partly from the original target zone within the low permeable layer into the saturated zone (aquifer). During 880 days after accomplishing the experiment, *pump and treat* technique was applied and achieved further contaminant removal. A mass balance considering groundwater

outflow samples and a groundwater flow rate of  $30 \frac{l}{h}$  yield  $2.13 \text{ kg}$  of additional contaminant removal. The estimated contaminant mass at the beginning of this experiment was  $6.6 \text{ kg}$ .

### 3.5.2 Steam Injection Pressure

Injection of steam into a saturated porous medium causes a displacement of water. Considering this, it becomes clear that a certain pressure is necessary in order to displace the water from the pores. The pressure  $p_w$  depends on the hydrostatic head above the injection screen of the well. However, it is of top priority not to exceed the maximum injection pressure to avoid shear failure and fractures in the subsurface where flow is preferred. Maximum injection pressure  $p_{inj}$  is calculated as follows:

$$p_{inj} = p_w + \sum_{i=1}^j p_{sj} = \rho_w g h_w + \sum_{i=1}^j \rho_{sj} g z_j, \quad \forall j \equiv \text{number of soils.} \quad (3.1)$$

$\rho_w$  is the density of water,  $h_w$  the hydrostatic head above the injection,  $\rho_s$  the soil bulk density and  $z$  the thickness of the respective soil layer. Assuming the lower limit of the maximum injection pressure at the top of the well screen, the parameters yield to  $\rho_w = 998.2 \frac{\text{kg}}{\text{m}^3}$ ,  $h_w = 1.95 \text{ m}$ ,  $z_{site3} = 1.65 \text{ m}$ ,  $z_{GEBA} = 0.2 \text{ m}$  and  $z_{M2} = 1.5 \text{ m}$ . Bulk densities of the soil materials are given in Table 3.3. Minimum injection pressure for this configuration so that steam is able to displace the water yields  $p_w = 1.19 \text{ bar}$ . The maximum injection pressure is determined to  $p_{inj} = 1.73 \text{ bar}$ .

### 3.5.3 Energy Balance Calculations

The total amount of energy input is provided by the released energy during condensation ( $\Delta h_v$ ) plus the enthalpy of water at  $100^\circ\text{C}$  (condensed steam), cf. TRÖTSCHLER ET AL. (2003) [32]

$$Q_{in} = m_{SI} \cdot (\Delta h_v + c_{p,w} (T_x - T_{init})) \quad (3.2)$$

The individual energy output of the component *SVE* is determined following Equation (3.3) written as

$$Q_{out,1} = m_{SVE} \cdot (h_w(T) x_w + h_a(T) x_a) \quad (3.3)$$

where  $m_{SVE}$  denotes the total mass of the extracted soil vapour and the enthalpy of *SVE* is composed of the enthalpy of air and water at the respective temperature.  $h_w$  includes in addition the enthalpy of vaporization  $\Delta h_v$ .

The energy content of the groundwater inflow and outflow as well as the condensate extraction from the unsaturated zone is determined following

$$Q_{out,2} = (m_{GWout} c_{p,w} \Delta T_{GWout} - m_{GWin} c_{p,w} \Delta T_{GWin}) + m_{C-UZ} c_{p,w} \Delta T_{C-UZ}, \quad (3.4)$$

where  $c_{p,w}$  denotes the specific heat capacity of water.

A certain part of the energy input caused by the steam injection is stored and distributed within the system. The remaining percentage is reckoned among the energy output comprising the soil vapour extraction, the groundwater and condensate outflow and the energy losses via the tank walls.

The stored energy within the system at a specific point in time can be determined following the Equations (3.5), (3.6) and (3.7). Consisting of the energy stored in the solid matrix  $Q_s$ , in the groundwater of the aquifer and the aquitard  $Q_{gw}$  and in the pore water of the vadose zone  $Q_{pw}$ .

$$Q_s = \sum_i c_{p,s} (1 - \Phi) \rho_s V_i (T_x - T_{init}) \quad (3.5)$$

$$Q_{gw} = \sum_i c_{p,w} \Phi \rho_w V_i (T_x - T_{init}) \quad (3.6)$$

$$Q_{pw} = \sum_i c_{w,s} \Phi \rho_w V_i (T_x - T_{init}) \quad (3.7)$$

Where  $c_p$  denotes the specific heat capacity of the soil and water ( $c_{p,w} = 4.2 \frac{kJ}{kgK}$ ), the respective porosity  $\phi$ , the density  $\rho$ , the volume  $V_i$  and the temperatures at initial state  $T_{init}$  and at the considered point in time  $T_x$ .

## 3.6 Slugtest

Hydraulic permeability or transmissivity, respectively, of aquifers is an important parameter for hydrogeologists to calculate flow and transport processes in the aquifer. Different methods for confined (COOPER ET AL. (1967) [12]) and unconfined (BOUWER AND RICE (1976) [9]) aquifers are available in order to gain parameters of the aquifer. One common method is the slug test, in which water is suddenly removed from or poured into the well to observe the hereby caused rise or fall, respectively, of the water level to its initial state over time. The measured data can then be used to determine hydraulic permeability or transmissivity of the aquifer. For further information on slug test and its realization, cf. KRUSEMAN AND DE RIDDER (2000) [23].

As soil parameters of *site 3* soil are available, a slug test would not be necessary to describe the hydraulic system. It was used to evaluate the hydraulic connection of the wells to the aquifer. Hence, slug tests were conducted for the steam injection wells *I1* and *I2* applying the method of HVORSLEV for a confined aquifer. Performing the slug test, water level in the well is suddenly increased and the rate of descent of the waterlevel ( $h$ ) is measured. The measured data of the slugtest is listed in the appendix (Ch. B) HVORSLEV developed various equations to meet certain conditions, the most commonly used is Equation (3.8):

$$k_f = \frac{r^2 \ln\left(\frac{L}{R}\right)}{2Lt_0} \quad (3.8)$$

where  $k_f$  is the hydraulic conductivity [ $\frac{m}{s}$ ],  $R$  the radius of the screen (i.e. effective radius),  $r$  the well casing radius and  $L$  the screen length in meters.  $t_0$  is the time it takes the water level to fall to 37% of the initial maximum  $H_0$ . The amount of water which was poured into the well can be determined following

$$V = (H - H_0)\pi r^2, \quad (3.9)$$

where  $H$  is the static head. The equation can be applied for any case where  $\frac{L}{R} > 8$ .

The normalized head  $\frac{H-h}{H-H_0}$  on the ordinate in log scale versus the linear scale time should yield a straight line for the recovery development with the exception of the initial lowering and the very late phase where head differences become difficult to measure.  $H - h$  denotes the drawdown and  $H - H_0$  the initial water level difference. Figure 3.10 show the plots for the steam injection wells *I1* and *I2*.

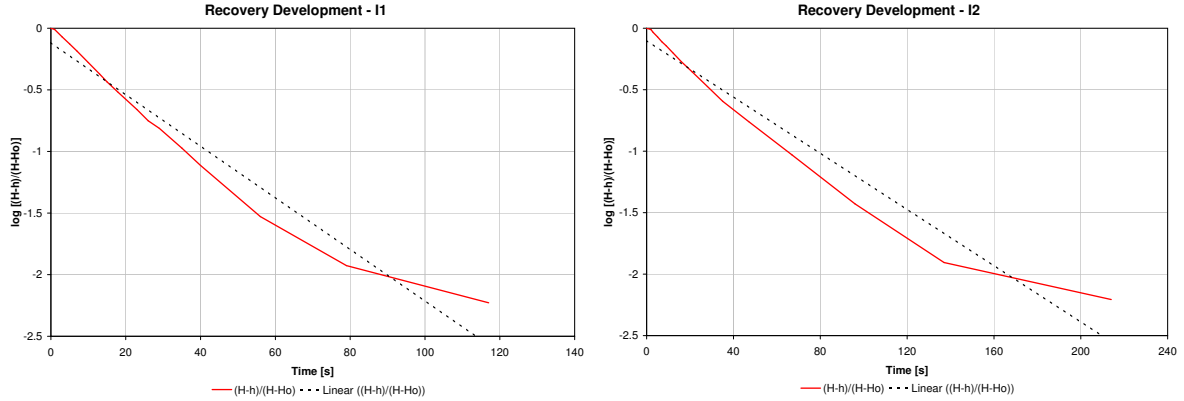


Figure 3.10: Normalized head over time for injection well I1 and I2

The hydraulic conductivities at the steam injection wells *I1* and *I2* were determined to  $4.0 \cdot 10^{-5} \frac{m}{s}$  and  $2.4 \cdot 10^{-5} \frac{m}{s}$ , respectively, following the method introduced in this section. Comparing the determined hydraulic conductivities to the hydraulic conductivity of the soil *site 3* ( $k_f = 1.6 - 1.9 \cdot 10^{-4}$ ) determined by HIESTER & BAKER (2009) [19], a decline in permeability of almost a magnitude is observed. This might result from compression of the porous medium at the well or clogging of the filter screen during the piling of the wells.

The hydraulic conductivity of the unsaturated zone at the extraction wells *E1* and *E2* can be calculated using the DUPUIT-THIEM well formula.

$$Q = \frac{K k_r 2\pi l \Delta p}{\eta \ln\left(\frac{R}{r}\right)}, \quad (3.10)$$

where  $K$  is the permeability [ $m^2$ ],  $k_r$  the relative permeability [-],  $l$  the filter screen length [ $m$ ],  $\Delta p$  the extraction pressure [ $bar$ ],  $\eta$  the dynamic viscosity [ $Pa \cdot s$ ],  $R$  the range of the well and  $r$  the well radius [ $m$ ]. Taking account of the extraction pressure and the mass flow observed during cold soil vapour extraction yield a hydraulic conductivity of  $5.4 \cdot 10^{-4} \frac{m}{s}$  and  $4.8 \cdot 10^{-4} \frac{m}{s}$  at well *E1* and *E2*, respectively.

## 3.7 Experimental Procedure

### 3.7.1 Operating Phases

Remediation with steam injection has to be considered a process with high variability. The occurrence and overlapping of processes, e.g. the breakthrough of steam at the soil vapour extraction wells requires a constant observation and adjustment of quantities. As a result of this, the remediation experiment is divided into six operation phases concerning significant changes of quantities.

Table 3.4: Operating phases

Phase	Duration	Characteristic	Purpose
I	$-42 - 0 d$	cold soil vapour extraction (medium extraction rate) and high groundwater inflow	background processes
II	$0 - 8.8 d$	high steam injection rate into saturated zone ( $I1$ and $I2$ ) and medium groundwater inflow	enhanced remediation and steam breakthrough
III	$8.8 - 28.8 d$	high soil vapour extraction rate by reason of steam breakthrough at extraction wells and medium steam injection rate ( $I1$ and $I2$ )	upkeep of thermal steady state and continuous heating of low permeable zone
IV	$28.8 - 48.25 d$	low steam injection into saturated zone ( $I1$ and $I2$ ) and unsaturated zone ( $I3$ and $I4$ )	<i>sandwich</i> heating to accelerate heating plateau temperature
V	$48.25 - 64 d$	medium steam injection into saturated zone ( $I1$ and $I2$ ) and shut down of steam injection into unsaturated zone ( $I3$ and $I4$ )	<i>steam override</i> to expand steamed zone again
VI	$64 - 65.8 d$	shut down of steam injection and continuous soil vapour extraction	cooling phase and capture of contaminant rebound

The operating conditions applied during the individual phases are listed in Table 3.5. However, the values given herein are averaged per phase for better visualization. The accurate parameter trends of the experiment procedure are shown in the Charts 3.11 to 3.14 in this section.



Table 3.5: Flow rates of operating phases

Parameter	Value						Unit
	I	II	III	IV	V	VI	
Groundwater level	3.08	3.08	3.08	3.08	3.08	3.08	[m]
Groundwater inflow rate	2	1.2	1.2	1.2	1.2	2.3	$[\frac{m^3}{d}]$
SVE - E1	17	15	30	30	30	39	$[\frac{kg}{h}]$
SVE - E2	18	17	40	40	40	39	$[\frac{kg}{h}]$
SI - I1	0	25	22	18.5	23	0	$[\frac{kg}{h}]$
SI - I2	0	25	22	18.5	23	0	$[\frac{kg}{h}]$
SI - I3	0	0	0	5	0	0	$[\frac{kg}{h}]$
SI - I4	0	0	0	5	0	0	$[\frac{kg}{h}]$
Total energy si	0	38	31	36	36	0	[kW]

### 3.7.2 Sampling and Parameter Data Acquisition Strategy

The performance of experiments requires an efficient strategy concerning sampling and parameter acquisition. The acquired data is utilized to determine the experimental progress and for basic calculations. In order to be able to determine the total recovered contaminant mass subsequent to the experiment, every contaminant discharge path has to be considered. The to-be-considered paths in the conducted experiment consisted of the soil vapour, the condensate, the groundwater outflow and the condensate extraction.

The observation of heat distribution requires the measurement of temperatures. Therefore, the measuring devices (Sec. 3.2) of the experiment worked automatically, recording temperatures of the tank and the contaminant concentration in the extracted soil vapour. The intervals of the collection of temperature data and the contaminant concentration were about 15 and 30 minutes, respectively. Data required to define energy and flow rate of steam injection, groundwater and soil vapour extraction was collected twice a day. Finally, chemical analysis of the discharged groundwater and the condensate/extraction well discharge was conducted twice a week by the chemical laboratory of the *VEGAS* to determine contaminant concentrations. The data for the determination of mass and energy flow was evaluated twice a day and the heat distribution was visualized once a day.

## 3.8 Experimental Results

In this section, I will discuss the essential parameters of the remediation experiment. These are the mass flow (Sec. 3.8.1) of steam injection, soil vapour extraction and groundwater, the heat distribution (Sec. 3.8.2) caused by the injected steam and the thereby induced contaminant recovery (Sec. 3.8.3).

### 3.8.1 Mass Flow

The operating phases introduced in Section 3.7.1 are the main sections of the experimental procedure and the occurring processes are discussed in detail in the following.

#### Phase I

After flooding the tank with carbon dioxide to achieve displacement of trapped air within the porous medium, start of phase **I** ( $t = -42 d$ ) was initialized. The activation of groundwater containment with a corresponding inflow of  $80 \frac{l}{h}$  resulted in a piezometric head difference between the groundwater inlet and outlet of about 18 centimeters corresponding to an average water level of 3.08 m (Tab. 3.5). The aim of the application of cold soil vapour extraction ( $m_{SVE} = 33 \frac{kg}{h}$ ) was to dewater the unsaturated zone and stabilize the capillary fringe above the water level. As a result of the surface sealing at the top of the tank, contaminant in the unsaturated zone was extracted instantly after starting the *SVE*. This is visualized in Figure 3.21 as the first peak of the *SVE* curve.

Due to problems concerning the measuring of the contaminant in the gas phase a shutdown of the soil vapour extraction was inevitable. After six days, SVE was reactivated and a continuous measuring of the contaminant in the gas phase was launched. At  $t = -33.8 d$  and  $t = -27 d$  first tests of steam injection with a flow rate of 25 and  $20 \frac{kg}{h}$ , respectively, were conducted and resulted in new installations of steam injection wells for reasons of poor hydraulic connection to the aquifer, cf. the slug test (Sec. 3.6). The effect of these tests was the increase of temperature within the tank to about 24°C (Fig. 3.16) and a short-term rise of contaminant discharge in the soil vapour extraction (Fig 3.21).

#### Phase II

Phase **II** ( $t = 0d$ ) characterizes the start of steam injection into saturated zone via injection wells *I1* and *I2* and a total injection rate of approximately  $50 \frac{kg}{h}$ . Simultaneously to the start of the steam injection, the groundwater inflow was reduced from 100 to  $50 \frac{l}{h}$  ( $1.2 \frac{m^3}{d}$ ) which was then kept constant during the ongoing experiment. In general, groundwater flow serves not only as a possibility to control the flow of heat

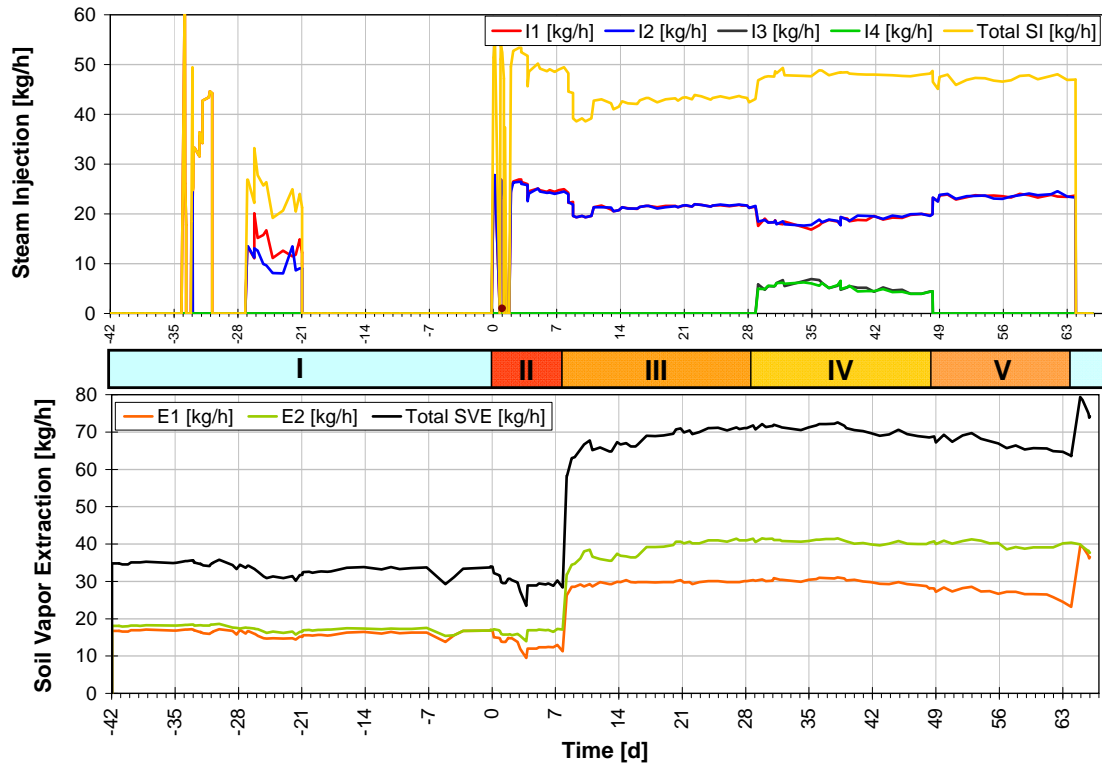


Figure 3.11: Flow rates of steam injection and soil vapour extraction

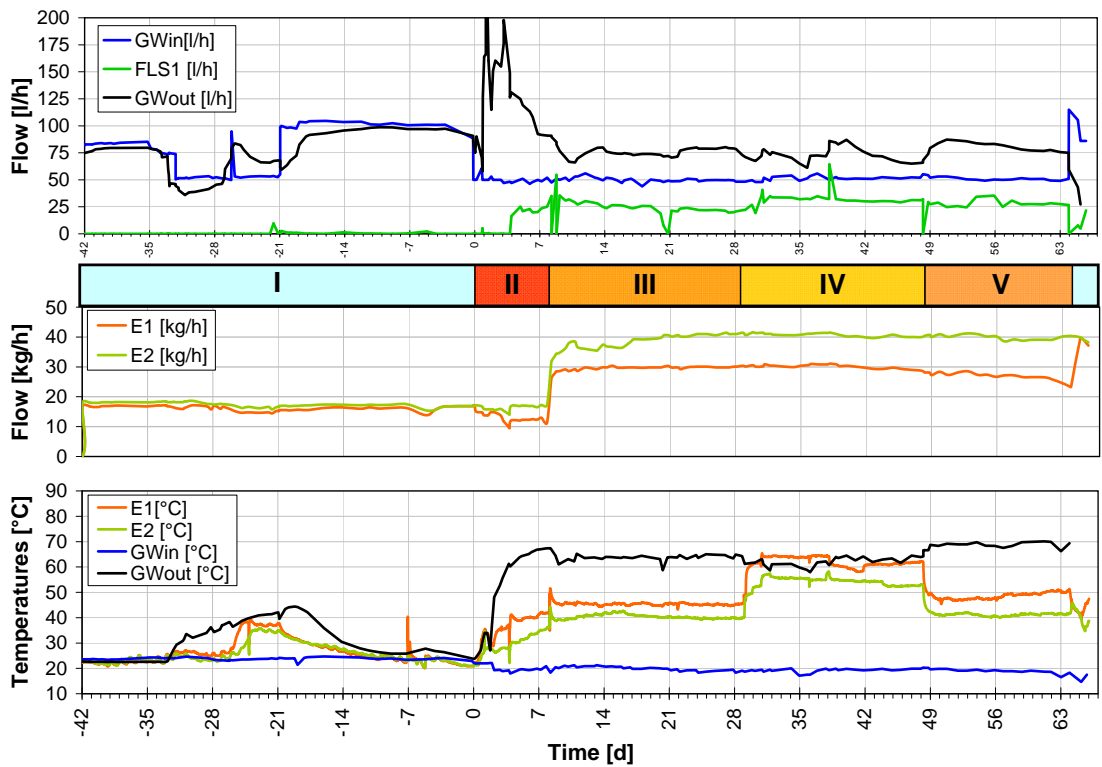


Figure 3.12: Flow rates and temperature of soil vapour extraction and groundwater

but also to recover the aqueous solubilized contaminants. A reduction of groundwater inflow decreases the cooling effect and thereby increase the heat distribution. The applied groundwater containment system is commonly used to gain hydraulic control of contaminant plumes, discussed in Section 3.8.3.

The unsteadiness of the injection rate at the beginning (day 1 to 4) was caused by breakdowns of the steam generator. Figure 3.11 shows plots of steam injection and soil vapour extraction rates over time. When steam entered the aquifer, the extending steam bubble caused a displacement of groundwater within the porous medium resulting in a rise of groundwater outflow. This effect is visualized by the peak of the groundwater outflow in Figure 3.12 (upper graph). Along with the beginning of steam injection, a steep climb of the groundwater outflow temperature (Fig. 3.12, lower graph) as condensing steam transferred heat to the passing groundwater flow was observed. The lowering of the groundwater inflow temperature had origin in the switching of previous used groundwater cycle to now fresh water supply by the degasing installation.

After four days of steam injection a significant increase of the soil vapour extraction temperature suggested the beginning of steam breakthrough at the extraction wells *E1* and *E2* (Fig. 3.11, lower graph). The significant reduction of the steam injection rate from 52 to 40  $\frac{kg}{h}$  was to prevent steam from climbing at the long sides of the tank and the therein resulting endangering of the pneumatic containment. By reason of the requirement of pneumatic containment, modifications were applied to the soil vapour extraction equipment in order to provide an increase of the extraction rate. A significant rise of the total extraction rate from 30 to 65  $\frac{kg}{h}$  (Fig. 3.11) yielded finally the steam breakthrough and led to the increase of energy output of the *SVE* to 3.75 kW, marking the start of phase **III**. This is visualized in Figure 3.26 (energy balance).

### Phase III

The self-adjusted higher extraction flow rate at *E2* (from  $t = 8.8 d$  forward) indicates a better connection of the well to the vadose zone or a better hydraulic conductivity, respectively. The difference of these flow rates was kept in order to capture the preferred vertical pathway of the steam propagation on the side of the extraction well *E2* of the tank. The established pneumatic capture reduced the problems of steam breakthrough after three days ( $t = 11.1 d$ ). Then the steam rate was increased to around 43  $\frac{kg}{h}$  and held constant during the rest of the phase. The renewed increase of steam injection resulted in a new displacement of groundwater, indicated by the raise of the groundwater outflow in Figure 3.13. Accompanying the increased extraction rate and the steam breakthrough is the rising of the outflow of *FLS1* as shown in Figure 3.13.

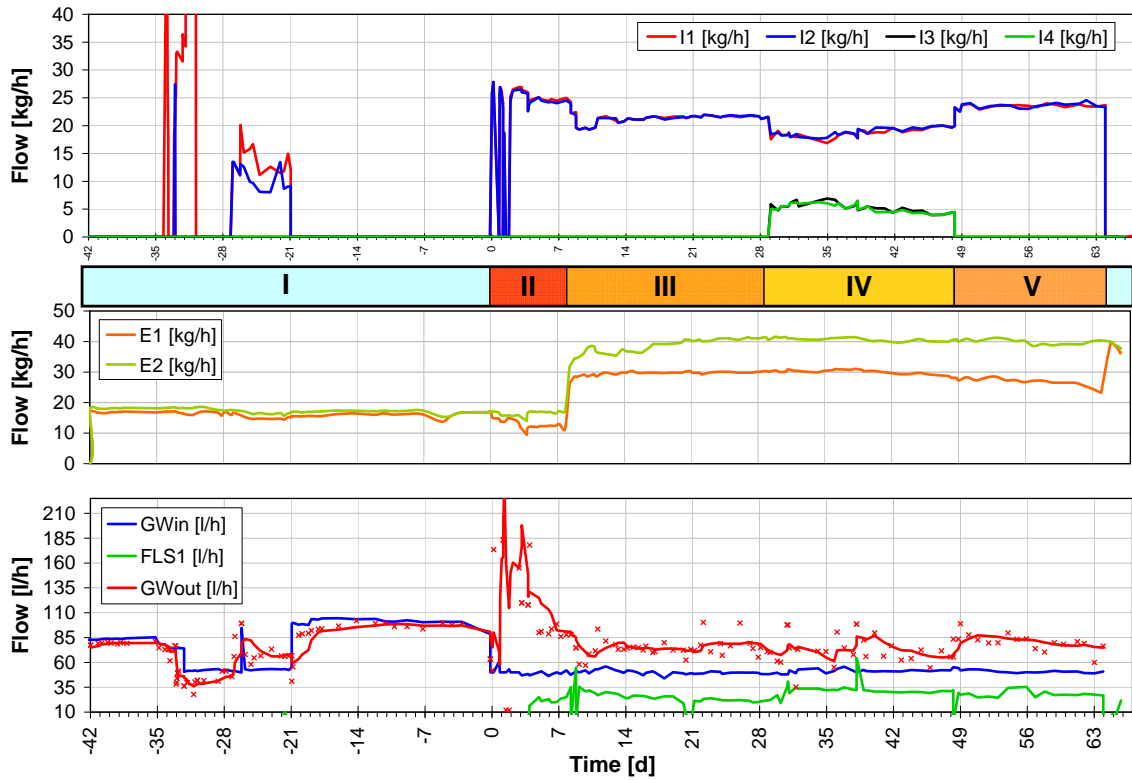


Figure 3.13: Flow rates of steam injection, soil vapour extraction, groundwater and condensate tank

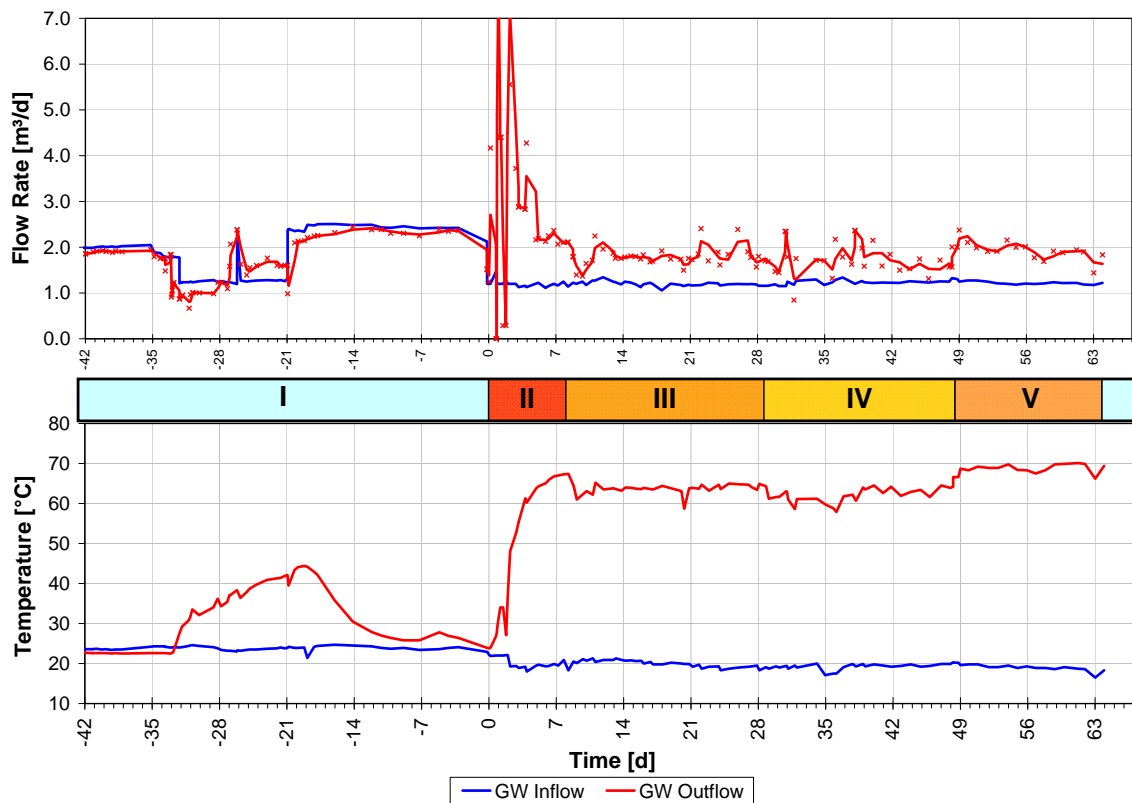


Figure 3.14: Flow rates and temperature of groundwater

In addition, the condensate extraction from the unsaturated zone, collected as well in *FLS1*, increased the outflow rate. The amount of water is composed on the one hand by condensed steam and on the other by water pushed from the lower to the upper zones as a result of the applied pressure from the steam injection. By means of DARCYS law, the upward flux in the center of the tank is determined by taking into account the pressure gradient  $\nabla p = \frac{\Delta h}{\Delta y}$ . The pressure head difference of about 0.695 m between 1.8 and 2.6 meters above ground level resulted in a flux calculated to  $0.76 \frac{l}{h \cdot m^2}$  at steady state at the end of phase **III** ( $t = 28.81 d$ ).

#### Phase IV

The achievement of a steady state condition concerning vertical heat distribution induced the beginning of phase **IV**, which was characterized by the investigation of effects of additional steam injection into the unsaturated zone via the injection wells *I3* and *I4*. Contrary to the initial expectations, the injection of steam only into the saturated zone achieved a temperature increase to about 90°C at the top of the low permeable *M2* layer in the center of the tank. At  $t = 28.8 d$  a total steam injection flow rate in the unsaturated zone of about  $12 \frac{kg}{h}$  and a corresponding energy input of about 9 kW caused a reduction of steam injection rate in the saturated zone to  $36 \frac{kg}{h}$  (23 kW). A simultaneous increase of the energy output via soil vapour extraction from previous 3.7 to around 8.5 kW was observed, indicating a fast steam breakthrough in the unsaturated zone (Fig. 3.26).

Comparing steam injection rates and groundwater outflow in Figure 3.13, one can observe a decrease of the groundwater outflow resulting from the collapse of the steam bubble in the saturated zone which was induced by the reduction of the steam flow rate ( $t = 28.8 d$ ). After two days from the start of the unsaturated steam injection, one observes an increase of the outflow rate and the energy output of the *FLS1*, cf. Figure 3.13 and 3.26. The close distance of the injection wells *I3* and *I4* to the extraction wells *E1* and *E2*, respectively, as well as the instantaneous rise of the *SVE* energy output indicated a limited expansion of heat in the unsaturated zone as the main part of the energy input left directly via the *SVE*. According to this thermal shortcut and since no further significant change in heat distribution in the unsaturated zone was observed, the injection into the unsaturated zone was shut down after 13 days ( $t = 44.9 d$ ) of operation.

Furthermore, no significant rise in the contaminant discharge via *SVE* during the steam injection into the unsaturated zone was observed and confirmed the complete remediation of the unsaturated zone. In addition, the contaminant discharge in the groundwater outflow stagnated at the end of phase **III** at an unsatisfactory concentration of approximately  $700 \frac{mg}{m^3}$ , cf. Figure 3.22. This reinforced the assumption of subsidence of contaminant from its original location within the low permeable *M2* layer into the aquifer (saturated zone) and required further remediation of the saturated zone.

**Phase V**

Since neither mass extraction nor heat distribution was enhanced by the *steam sandwich* technique, the reinitiating of steam injection only into the saturated zone in order to achieve further contaminant recovery from the saturated zone was started. The steam injection flow rate was increased from 38 to 47  $\frac{kg}{h}$  (35 kW) in order to re-expand the steamed zone in the aquifer which resulted again in the displacement of groundwater (Fig. 3.13) and temperature increase (Fig. 3.14).

**Phase VI**

After 14 days, at  $t = 64 d$ , the steam injection was shut down and the cold soil vapour extraction was maintained in operation for another two days in order to capture the contaminant concentration rebound. An increase of the *SVE* flow rate after the shutdown of the steam injection was observed. This can be explained by the reduced amount of steam in the *SVE* which reduced the viscosity and caused an increase of relative permeability as the temperature of the soil vapour decreased. The remediation experiment was terminated after 65.8 days.

### 3.8.2 Heat Distribution

Heat distribution is the main concern of a thermally enhanced in-situ soil remediation. This section discusses the distribution observed during the different phases of the remediation experiment, shown in Figure 3.16 and 3.17. The plots were drawn by means of *Tecplot 360 2009<sup>TM</sup>* (Tecplot, Inc., Bellevue, USA) from the acquired temperature data at the two cross-sections (Fig. 3.1). The temperature plots show the three-dimensional view of the tank with six horizontal planes at different heights and one vertical plane in the center of the tank. As there are only these two cross-sections, temperature profiles *H* to *A* were mirrored at profile *J* to the other side of the tank to improve the visualization of the heat propagation in the tank. Furthermore, the measured groundwater inflow and outflow temperatures were set at the location of the horizontal groundwater inflow and outflow well, respectively. Groundwater inflow is located at the right hand side and outflow on the left hand side, respectively. The temperature ranges from 20 to 100°C. The vertical black lines represent the location of the steam injection wells *I1*, *I2*, *I3* and *I4* as well as the extraction wells *E1* and *E2*. The initial temperature within the tank at the beginning of phase **II** was measured to be 24°C (Fig 3.16).

Figure 3.15 shows the averaged temperature of the saturated zone ( $0 \leq y \leq 1.5 \text{ m}$ ), the low permeable *M2* zone ( $1.5 \leq y \leq 3 \text{ m}$ ) and the unsaturated zone ( $3.0 \leq y \leq 4.5 \text{ m}$ ) from  $t = 0 \text{ d}$ .

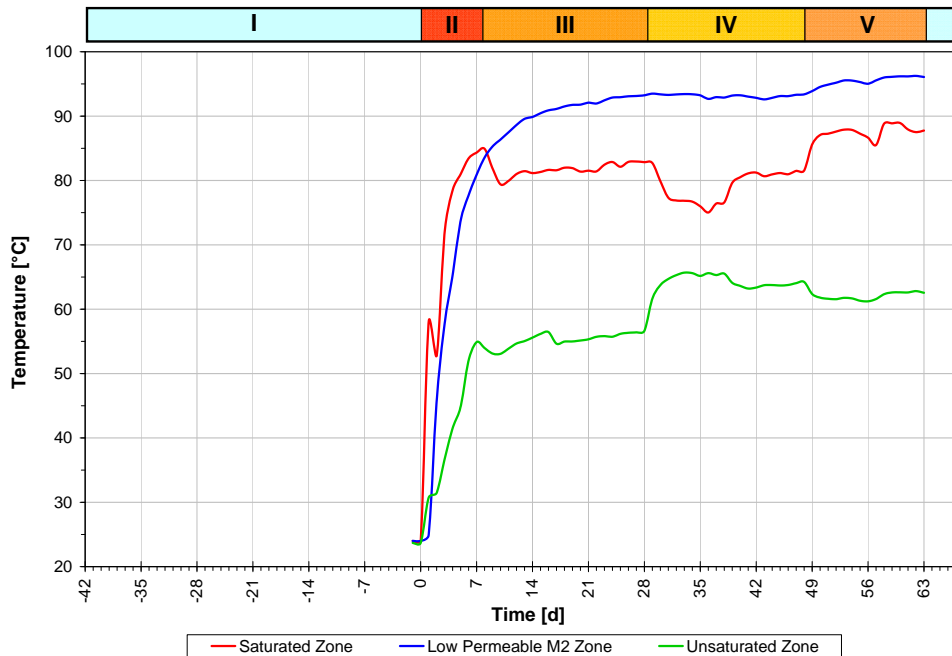


Figure 3.15: Temperature trends of saturated, low permeable *M2* and unsaturated zone



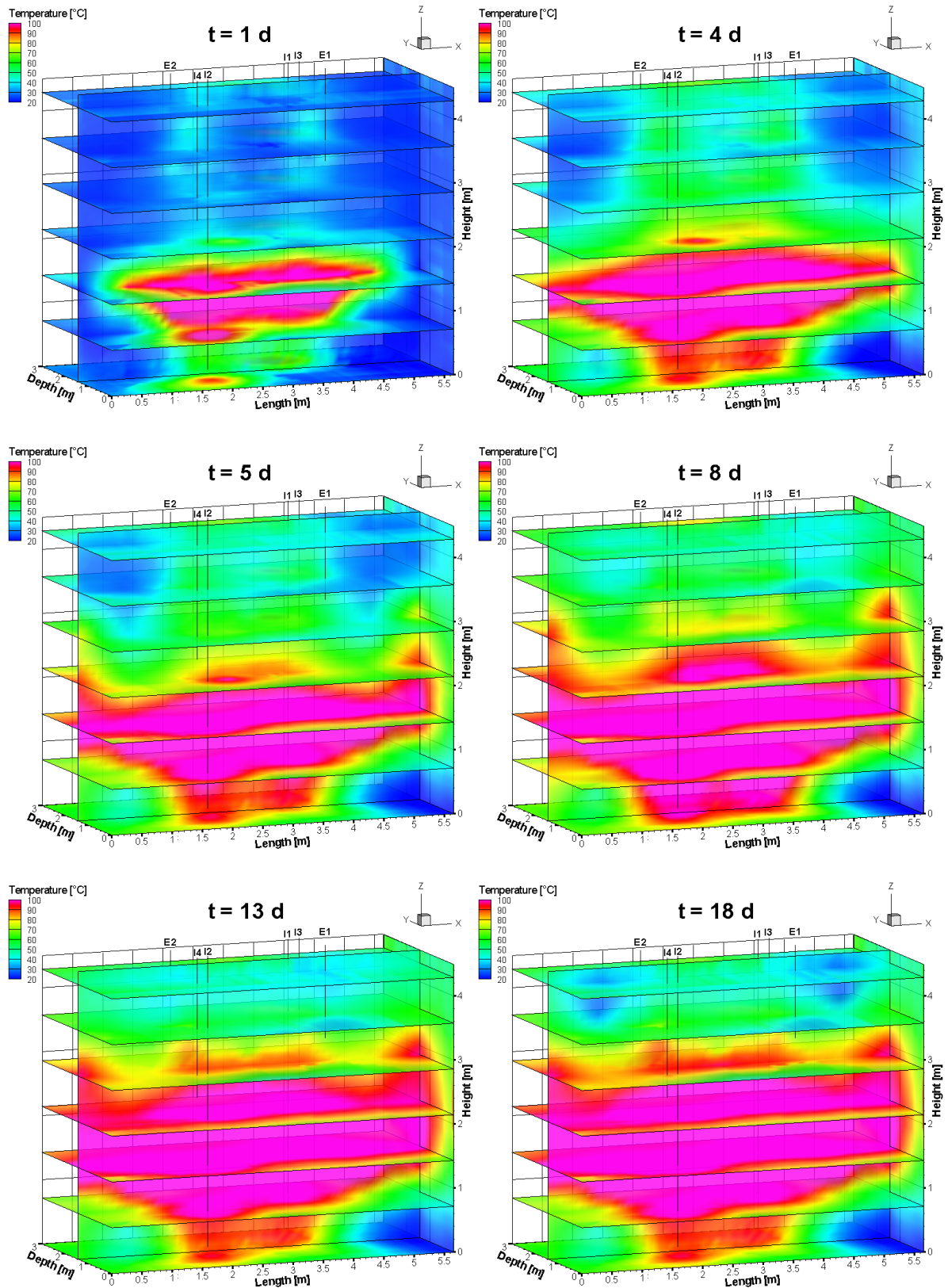


Figure 3.16: Heat distribution plots of remediation experiment (1 – 18d)

After one day of steam injection, a horizontal distribution was observed as the ascent of the steam caused by buoyancy effects was hindered by the presence of the low permeable  $M2$  layer. Furthermore, a slight warming alongside the injection wells caused by heat conduction was observed. The steam front reached the long sides of the tank at  $t = 4 d$  establishing an expanded steamed zone below the aquitard layer.

At  $t = 8 d$ , one can observe the consequence of the *steam override* process below the low permeable layer, heating the latter. As a result of the heated aquifer, groundwater inflow at a temperature of about  $18.5^{\circ}C$  is visible demonstrating the cooling effect on the heating process. As a consequence of the high steam injection rate and therewith a relative high injection pressure, a fast ascending of the steam at the long sides of the tank was observed. In order to prevent this effect, the steam injection rate was reduced significantly while the soil vapour extraction rate was increased at  $t = 8.8 d$ , illustrated in Figure 3.11 (Phase **II**).

Temperature plots at  $t = 13 - 23 d$  illustrate the continuous heating process of the low permeable  $M2$  layer over the almost entire ground area. After 28 days of steam injection into the saturated zone with a total energy input of about  $22 kWh$ , steady state was reached concerning the heat distribution. The corresponding plot demonstrates the successful warming-up of the low permeable layer up to the top at  $H = 3 m$  above ground level, exceeding the temperature of  $90^{\circ}C$ . However, this region was constricted to the area between the injection wells  $I1$  and  $I2$  which was in fact the original target zone where the contaminant had been infiltrated in 2007.

The combined steam injection into the saturated and the unsaturated zone (*steam sandwich*) at the beginning of phase **IV** ( $t_{abs} = 28.8 d$ ) demonstrated a significant effect on the heat distribution (Fig. 3.17). Comparing the temperature plots after 28 and 31 days of steam injection, a clear decrease of the steam front expansion in the aquifer at a height of about  $0 \leq H \leq 0.7 m$  was observed, which came along with an expansion of the cold groundwater inflow region. Furthermore, an increase of temperature in the vadose zone above the low permeable layer at the injection wells  $I3$  and  $I4$  was detected.

At  $t = 38 d$ , after 9 days of combined steam injection, no further temperature expansion in the vadose zone was noticeable as a result of the close distance to the soil vapour extraction wells. Hence, the steam flow rate into the unsaturated zone was reduced from this point in time until such time as the complete shut-down of the steam injection into the unsaturated zone at  $t = 48.25 d$ . In order to achieve again a wide-spread expansion of the steam front in the aquifer, the steam injection rate into the saturated zone was increased once again (phase **V**). At the end of the steam injection at  $t = 64 d$  no further heat expansion was noticeable.

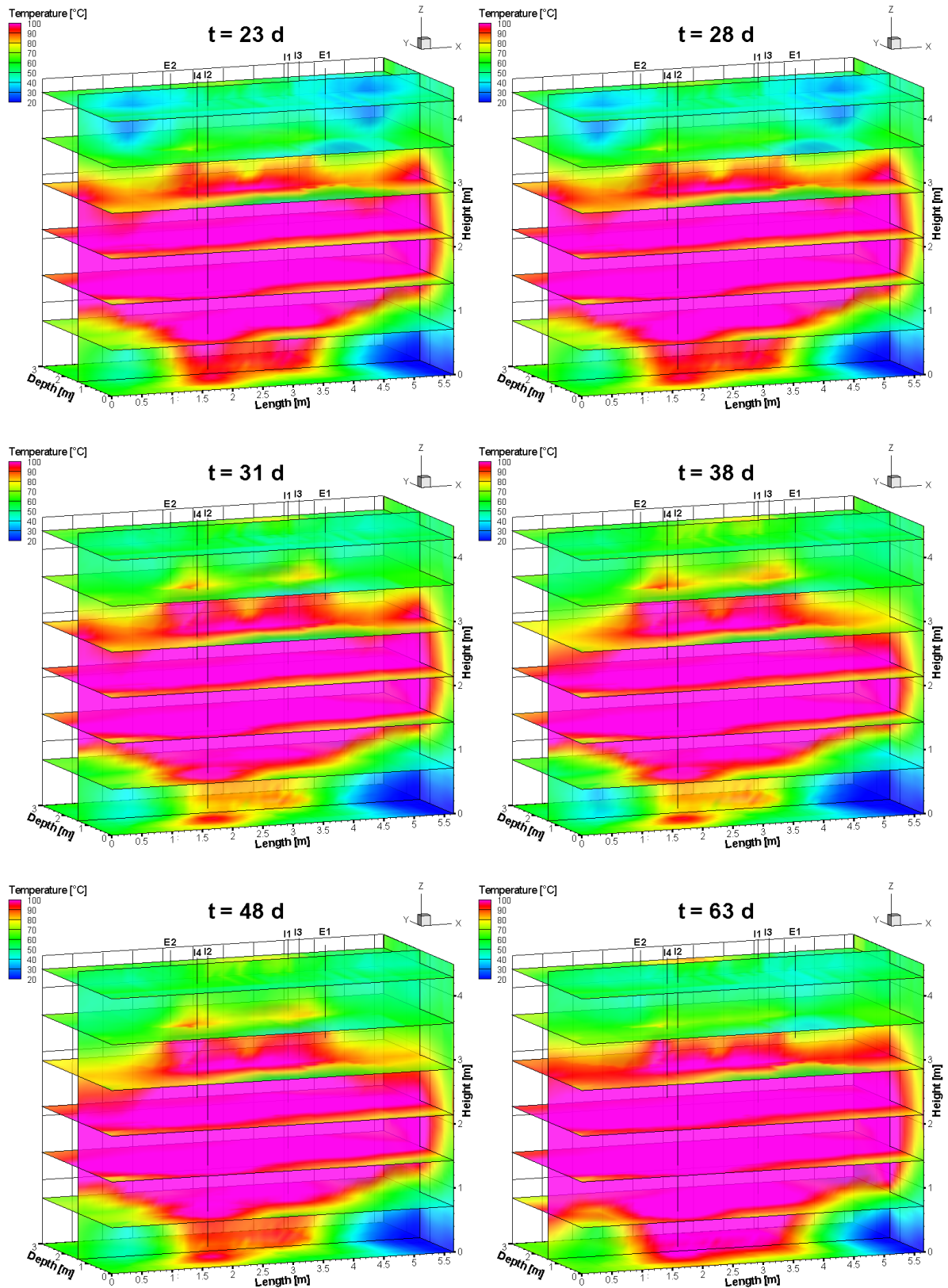


Figure 3.17: Heat distribution plots of remediation experiment (28 – 63d)

Figure 3.18 shows the temperature trend of selected temperature sensors of the profile  $J$  in the center of the tank at 1.55 (bottom of  $M2$ ), 2.25 (middle of  $M2$ ), 2.95 (top of  $M2$ ) and 3.30 m (unsaturated zone) above ground level. Observing a strong rise of temperature in phase **II** at each sensor, then was reduced during phase **III**. Due to buoyancy forces effecting vertical steam propagation the temperature at  $H = 1.55$  m, at the bottom side of the low permeable  $M2$  layer, reached  $100^{\circ}\text{C}$  after the first day of steam injection. The abrupt temperature fall was a result of the short-time steam generator breakdown. In the center of the aquitard ( $H = 2.25$  m), a constant temperature of about  $102.7^{\circ}\text{C}$  was reached at the end of phase **II**. At  $t = 15.9$  d, the zone of interest ( $J-295$ ) was heated to the target temperature of about  $90^{\circ}\text{C}$ . At the end of phase **III**,  $J-295$  at the top of the aquitard displayed a temperature at this point in time of about  $99.6^{\circ}\text{C}$  at  $H = 2.95$  m and and  $79.4^{\circ}\text{C}$  at  $H = 3.30$  m.

The combined steam injection only affected the temperature in the vadose zone, cf.  $J-330$ , showing a significant rise at the beginning of phase **IV** and an instantaneous temperature decrease caused by the shut-down of the injection wells  $I3$  and  $I4$ . However, the  $J-330$  reached a maximum temperature of  $90.6^{\circ}\text{C}$  although steam was injected into the unsaturated zone. The closer distance of the injection wells  $I3$  and  $I4$  to the extraction wells  $E1$  and  $E2$ , respectively, than to the temperature sensor  $J-330$  was responsible for this behaviour.

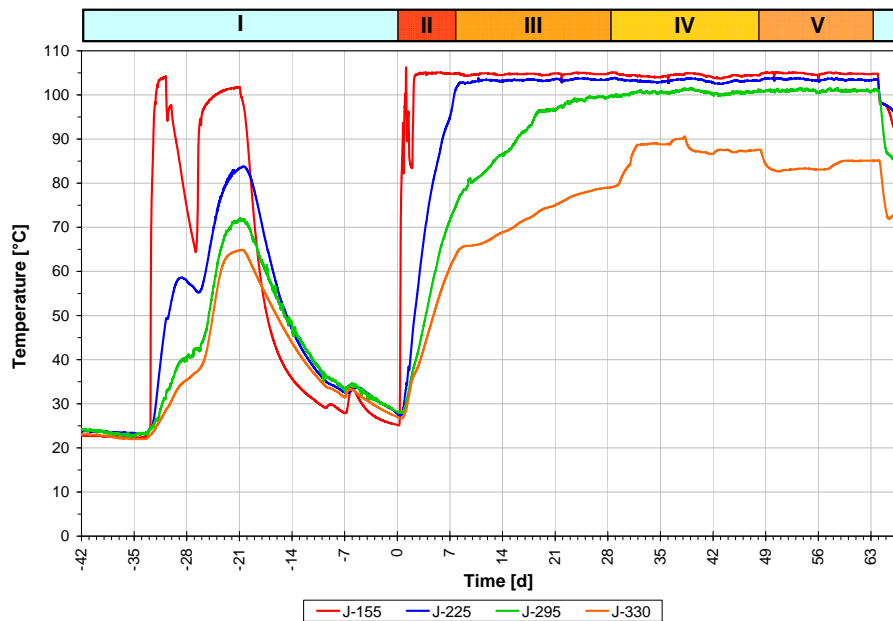


Figure 3.18: Temperature trends of profile  $J$  temperature sensors

In Section 2.9 the typical behaviour of steam propagation in saturated zones was discussed. Figure 3.19 depicts the impact of buoyancy forces on the injected steam observed after three and 28 days of steam injection. The heat distribution plot is illus-

trating the cross-section in the center of the tank. Contaminants are transported with the condensation front ahead of the steam front. Hence, fractions of the contaminant in the saturated zone were pushed to the margins of the tank and deposited there as the steam could not propagate further to the walls. The two ellipses mark the location of the potential contaminant deposition.

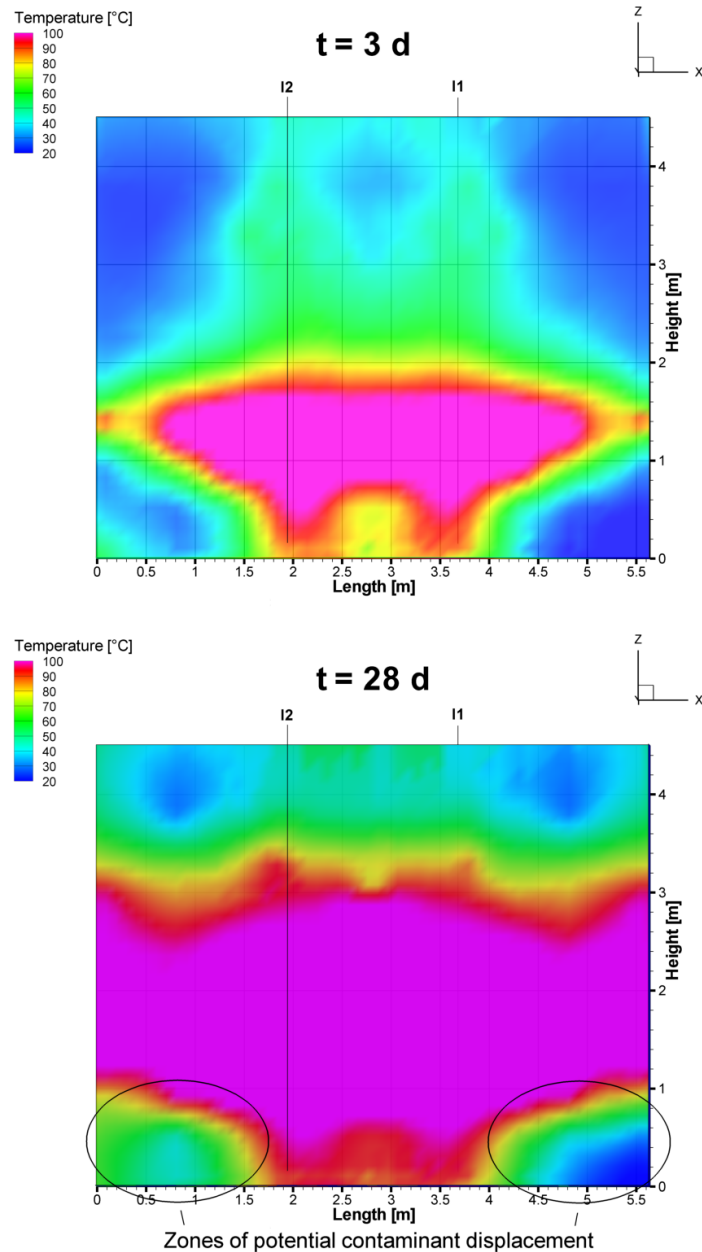


Figure 3.19: Effect of buoyancy forces on steam propagation ( $t = 3$  &  $28 d$ )

### 3.8.3 Contaminant Recovery

The energy input by steam injection in the tank enhanced significantly the recovery of contaminant (*PCE*). After 65.8 days of remediation, a total amount of about 3.03 *kg* was removed from the subsoil in the tank. This matches 45.8% of the initial total amount previously estimated (Sec. 3.5). Chart 3.20 depicts the percentage of the individual discharge path concerning the total contaminant recovery sum.

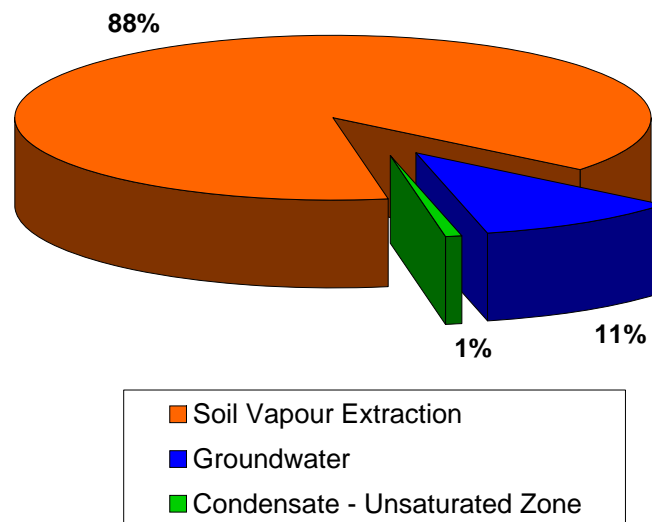


Figure 3.20: Percentage distribution of contaminant recovery

The main discharge path was the soil vapour extraction with a removal of 2.68 *kg* (88%). The groundwater outflow removed 0.33 *kg* (11%). 0.02 *kg* (1%) of the contaminant was extracted with the condensate from the unsaturated zone. The relation between the recovered contaminant and the steam energy input yielded a thermal effort of about 17.2 *MWh*, which corresponds to 1440 €, per recovered kilogram of contaminant. A *pump and treat* technique would need about six years with a flow rate of  $Q = 30 \frac{l}{h}$  (energy consumption: 300W) to remove 3 *kg* of contaminant from the tank. The energy effort would be 5.568 *MWh* (1114 €) per kilogram of contaminant.

Figure 3.21 depicts the contaminant removal in unit mass per unit time of the *SVE* and the *GW* as well as the total sum of the recovered contaminant amount. Figure 3.23 and 3.22 show *PCE* concentrations of the *SVE* and the groundwater outflow as well as the groundwater outflow and the *FLS1*, respectively. Furthermore, the cumulative sums of the contaminant of the individual contaminant recovery paths are shown in Figure 3.24.

At the beginning of the experiment, an initial concentration of *PCE* of about  $1.8 \frac{mg}{l}$  was measured in the groundwater outflow (Fig. 3.22). Preliminary to the start of the steam injection (phase **II**), the extracted soil vapour measured no *PCE* concentrations. The steam injection tests during phase **I** (cf. Sec. 3.8.1), however, caused concentration peaks in the extracted soil vapour for a short time. The increase of contaminant removal in the groundwater outflow may be related to the steam tests.

Simultaneous to the start of the remediation experiment ( $t = 0 d$ ), a significant rise of the contaminant removal in the groundwater was observed (Fig. 3.21). The input of heat into the porous medium provoked a fast recovery at the already heated area around the injection wells. The fast recovery was caused by the better solubility of *PCE* in water and the reduced residual saturation of *PCE* due to the increased temperature. This effect benefited the drift of *PCE*, which was induced by the groundwater flow. As a result of this, the maximum concentration measured in the groundwater outflow was about  $3.29 \frac{mg}{l}$  (Fig. 3.22,  $t = 2.8 d$ ). The peak in Figure 3.21 demonstrates the importance of the groundwater containment system (*GCS*) concerning contaminant removal and protection of downstream located areas. The *GCS* not only provided a possibility to control contaminant plumes but also represented a minor remediation path (max. 11%).

After 2.8 days of steam injection, the concentration of *PCE* in the gas phase of the *SVE* began to rise observably to the highest discharge rate of about  $240 \frac{g}{d}$  at  $t = 8.5 d$ . With the increase of the soil vapour extraction rate at the steam breakthrough ( $t = 4 d$ ), a simultaneous removal rise of *FLS1* with a maximum discharge concentration of about  $2.4 \frac{g}{d}$  after 8.8 days from the beginning of *SI* was observed. By theory, the recovered contaminant mass in *FLS1* was extracted by the *SVE* and removed during offgas treatment. Within phase **III**, the comparative constant effective energy input (Fig. 3.26) characterized a decline concerning the contaminant discharge rate in every discharge path.

Comparing Figure 3.23 from  $t = 28.8 d$  on, the additional steam injection into the unsaturated zone (*steam sandwich*) caused no supplemental contaminant recovery. This confirmed the assumption that contaminants gravitated from its original location within the *M2* layer towards the bottom of the tank since the performance of the previous remediation experiment in 2008.

The shut-down of the unsaturated steam injection wells at the beginning of phase **V** and the increase of the steam flow rate into the saturated zone resulted again in an increase of contaminant discharge concentration in the *SVE* and the groundwater outflow (Fig. 3.22). Finally, at  $t = 64 d$ , the contaminant concentration of *SVE*, groundwater outflow and *FLS1* stagnated at around  $c_{SVE} = 9.5 \frac{mg}{m^3}$ ,  $c_{GWout} = 360 \frac{mg}{m^3}$  and  $c_{FLS1} = 110 \frac{mg}{m^3}$ . The steam injection was therefore ceased. The shut down induced a high vacuum in the steamed zone, which mobilized additionally previous trapped contaminant. Thus, a concentration rise in the extracted soil

vapour could be observed reaching a maximum value of about  $50 \frac{mg}{m^3}$ . Along with the increase of concentration in the extracted soil vapour, a raised concentration in the outflow of the *FLS1* was observed (Fig. 3.23). After two days of cold soil vapour extraction, the contaminant concentration in the soil vapour decreased to  $0.5 \frac{mg}{m^3}$  and indicated the end of the remediation and the termination of the experiment.

The steam injection was responsible for the significant increase of the contaminant removal (Fig. 3.22). The contaminant concentration in the groundwater decreased by 85% compared to the initial contaminant concentration. However, compared with the *SVE* (99%), the relative contaminant removal remained at a comparative high value. The persisting contamination of the saturated zone is evident. The aqueous equilibrium concentration of the measured *SVE* concentrations can be determined by means of HENRY coefficient of *PCE*. The dimensionless HENRY coefficient at 20°C (gas temperature at the heat exchanger outflow) is  $H = 0.579$  (EPA SITE ASSESSMENT CALCULATION TOOL [2]). The calculated aqueous concentration in comparison with the measured concentrations of the *FLS1* showed a significant discrepancy, cf. appendix (A.2). Contaminant concentrations of the *FLS1* were 10 to 40-fold higher. Although condensate was removed from the unsaturated zone, it is possible that fractions of condensed contaminant accumulated there as steam propagation was limited in the unsaturated zone. This expressed the need for condensate extraction from the unsaturated zone.



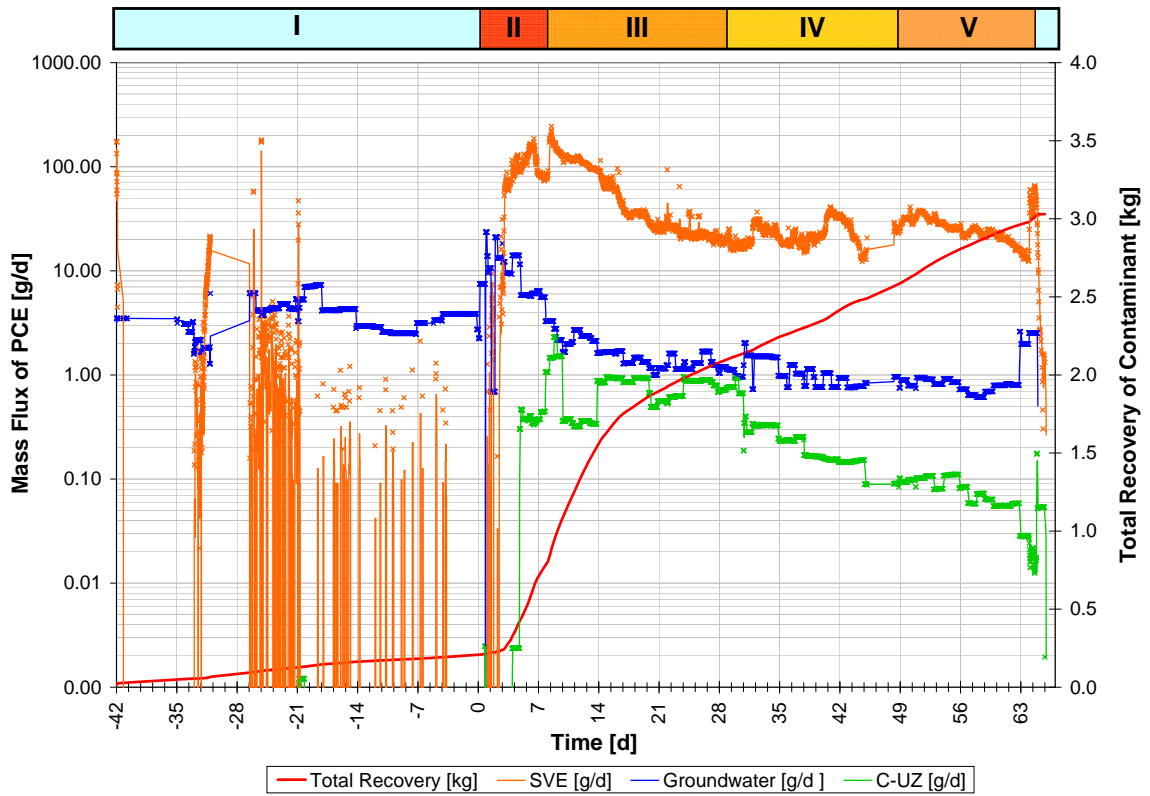


Figure 3.21: Contaminant discharge rate and total sum

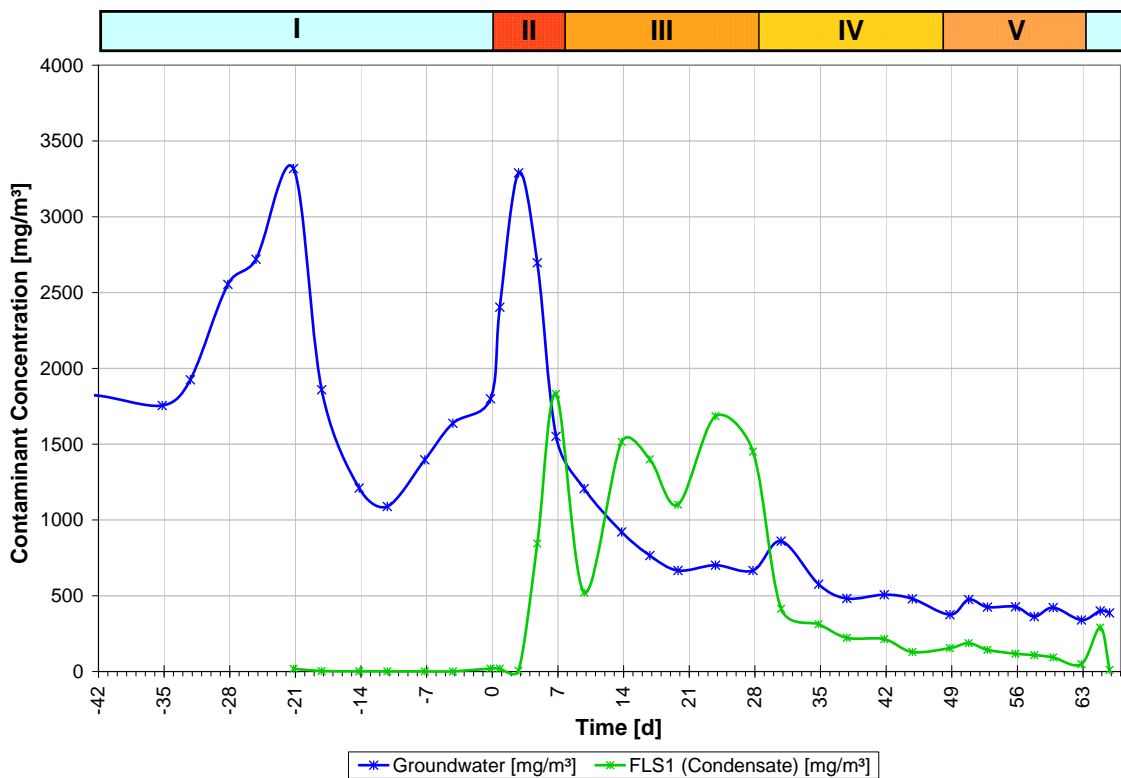


Figure 3.22: Contaminant concentration of groundwater and condensate tank

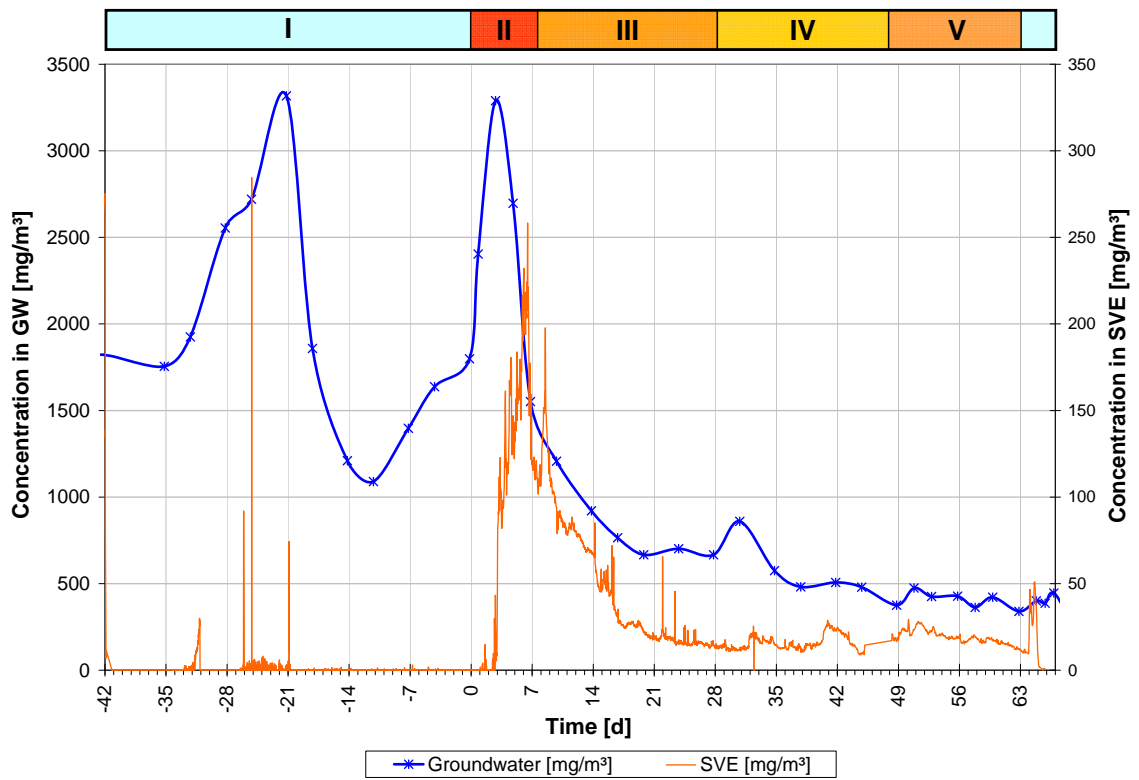


Figure 3.23: Contaminant concentration of soil vapour extraction and groundwater

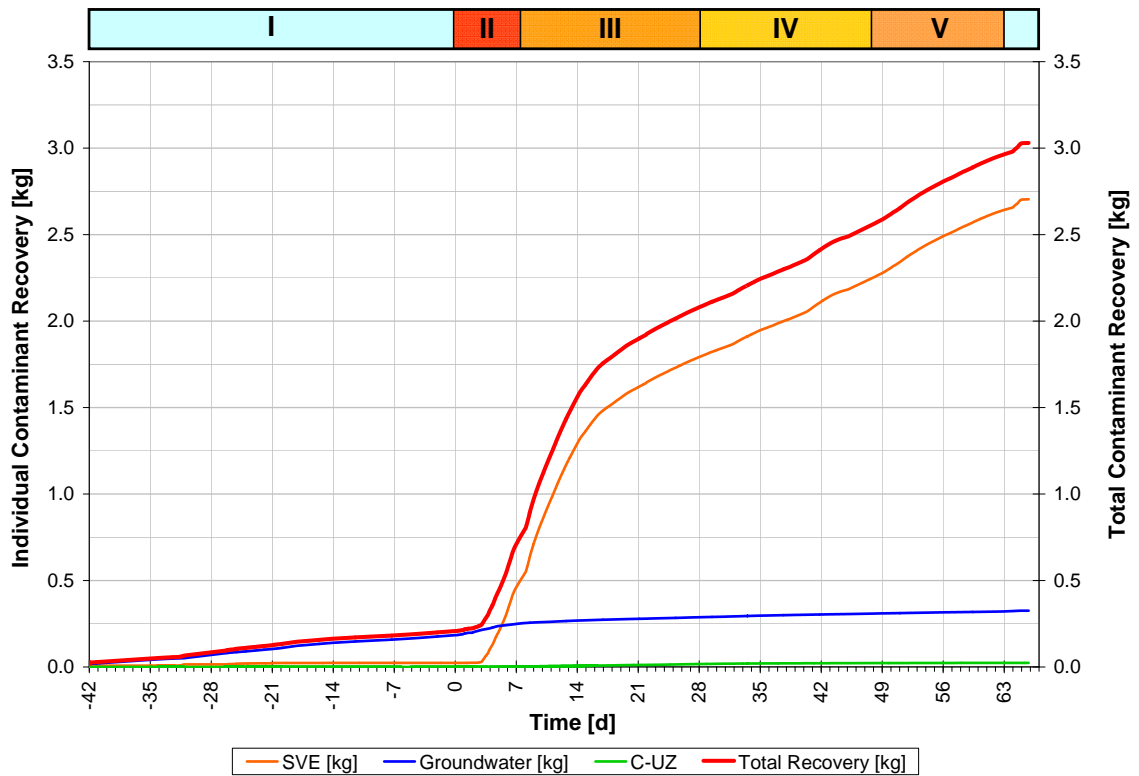


Figure 3.24: Cumulative contaminant recovery

### 3.8.4 Water Mass Balance

The remediation experiment using steam injection technique was dominated by significant water flows compared to the air flow. Not only the groundwater flow but also the steam injection and the soil vapour extraction caused a water mass flow. In order to be able to quantify the water displacement by the injected steam and determine the amount of condensed steam, the water mass balance for the tank (saturated and unsaturated zone) was determined considering the relevant quantities. The total amount of water in the tank at  $t = 0$  d can be determined by means of the geometry of the tank, the porosity of the soils and the initial water level or water saturation, respectively.

Full saturation in the aquifer and the aquitard as well as in the two transition layers below and above of it was assumed. The water saturation of the vadose zone was estimated to  $S_{VZ} = 0.15$ . During steam injection water was displaced from the tank caused by the expanding steam zone. The water displacement is calculated from the difference between the input and output water mass. The amount of condensed steam in the tank is defined as the difference between steam mass and soil vapour condensate. Table 3.6 contains the water mass balance of phase **II-III** and **II-IV** as well as the total mass balance after the termination of the remediation experiment.

At the end of phase **III** and **IV**, respectively, approximately 90% of the injected steam condensed in the tank. 20% of the water in the pore volume was replaced by the steam at the end of phase **III** and 7% at the end of phase **IV**.

Table 3.6: Mass balance of remediation experiment (phase **II-III**, **II-IV** & **total**)

Phase	<b>II-III</b>	<b>II-IV</b>	<b>Total</b>	Unit
Container specifications				
Duration	28.81	48.25	65.80	<i>d</i>
Volume of tank		81		<i>m</i> <sup>3</sup>
Pore volume		20.27		<i>m</i> <sup>3</sup>
Initial water content		21.35		$\cdot 10^3 kg$
Remaining water content	15.54	17.62	15.76	$\cdot 10^3 kg$
Removed water percentage	27.2	17.5	26.2	%
Total mass				
Steam	30.10	52.44	70.20	$\cdot 10^3 kg$
Groundwater inflow	34.38	58.40	77.60	$\cdot 10^3 kg$
Groundwater outflow	-59.66	-92.63	-122.72	$\cdot 10^3 kg$
Condensate	-2.20	-6.48	-8.20	$\cdot 10^3 kg$
Extraction well d/c	-12.51	-23.11	-32.17	$\cdot 10^3 kg$
Displaced water	-5.81	-3.73	-5.59	$\cdot 10^3 kg$
Condensed steam in soil	27.90	45.97	62.0	$\cdot 10^3 kg$
Ratio (displaced water / injected steam)	19.3	7.1	7.7	%

### 3.8.5 Energy Balance

The application of steam injection into the saturated and unsaturated zone was successfully accomplished concerning the main objective of heating the top of the aquitard up to 90°C (Sec. 3.8.2). Comparing the experiment charts and the temperature plots, it is evident that the energy input of the injected steam and the energy output show a highly interdependent behaviour during the entire experimental procedure. Hence, Figure 3.25 visualizes the input and output quantities in a schematic sketch, derived from TRÖTSCHLER ET AL. (2004) [32].

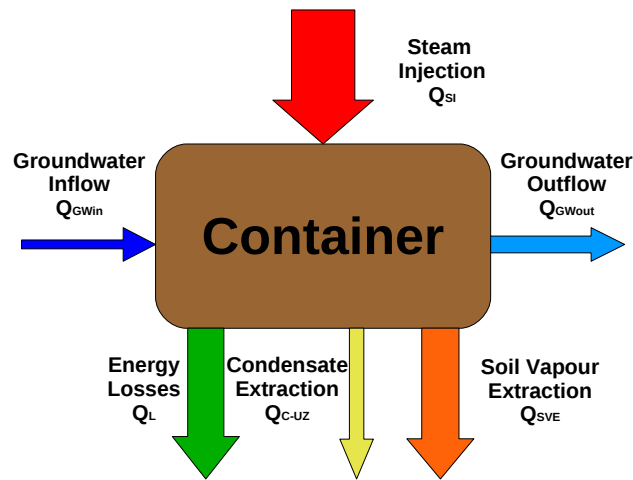


Figure 3.25: Energy input and output quantities

The thermal energy input includes the steam injection  $\dot{Q}_{SI}$  and the groundwater inflow  $\dot{Q}_{GWin}$ . The extraction of soil vapour  $\dot{Q}_{SVE}$  and the groundwater outflow  $\dot{Q}_{GWout}$  contribute to the energy output. The extraction wells water discharge  $\dot{Q}_{C-UZ}$  (condensate from unsaturated zone) counts in addition to the regular energy output quantities. The effective energy input is then determined by the difference between the input and output quantities and denotes the remaining energy quantity delivered to the porous medium. The outcome of the high energy input was an extensive heat expansion as far as the tank walls. Considering this, energy losses via the tank walls must not be neglected and, therefore, will be discussed in Section 3.8.6.

Figure 3.26 depicts the energy input and energy output over the duration of the remediation experiment. The effective energy input corresponds to the steam injection energy, influenced by the changes in the groundwater energy output. These changes can be traced back to the sensitivity of the steamed zone concerning even minor changes in the steam injection rate, e.g. caused by re-adjustments of the flow rate or maintenances of the steam generator.

A major difference was observed in phase **IV** ( $t = 28.8 d$ ) during combined steam injection into the saturated and unsaturated zone. In spite of an increased energy input ( $SI$ ), the effective energy input decreased slightly. This is explained by the major increase of the energy output in the soil vapour extraction and the resulting condensate. From  $t = 40 d$  on, the injection into the saturated zone was slightly increased and the flow rate into the unsaturated zone decreased as illustrated in Figure 3.11. Herefrom resulted the rise of the effective energy input as a result of the drop of energy output of the  $SVE$  and the condensate ( $t = 39 d$ ).

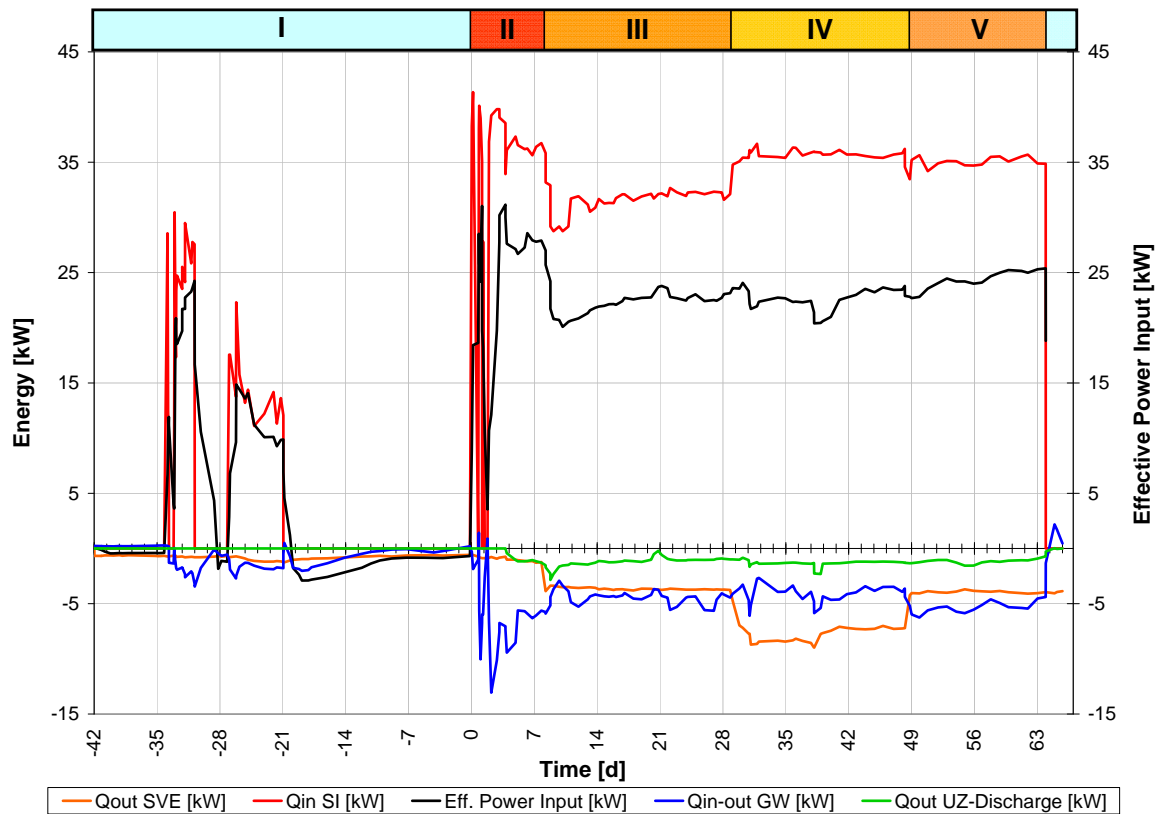


Figure 3.26: Energy input and output

At the end of phase **III**, steady state of heat distribution was reached, cf. Section 3.8.2. In state of equilibrium no more energy is used to heat the soil and pore water of the tank. The difference between input and output quantities represents the effective energy input which was used to heat up the tank. However, at steady state the input-output difference denotes the energy losses via the tank walls. Table 3.7 lists the total cumulative input and output (**II-III**, **II-IV** and **Total**) since start of steam injection at  $t = 0d$  and the averaged momentary energy input and output at the end of phase **III** ( $t = 28.8d$ ).

Table 3.7: Energy balance of remediation experiment (phase **II-III**, **II-IV** & **total**)

Phase	<b>II-III</b>		<b>II-IV</b>		<b>Total</b>	
Duration [d]	28.81		48.25		65.80	
Sum	Mass [ $\cdot 10^3 kg$ ]	Energy [ $MWh$ ]	Mass [ $\cdot 10^3 kg$ ]	Energy [ $MWh$ ]	Mass [ $\cdot 10^3 kg$ ]	Energy [ $MWh$ ]
Steam	30.1	22.4	52.4	39.4	70.2	52.2
Groundwater inflow	34.4	0.80	58.4	1.35	77.6	1.76
Groundwater outflow	-59.7	-4.39	-92.6	-6.81	-122.7	-9.13
Soil vapour extraction	-39.4	-1.99	73.3	-5.64	-97.6	-7.09
Condensate	-2.20	-1.64	-6.48	-4.90	-8.20	-6.11
Extraction well d/c	-12.5	-0.70	-23.1	-1.33	-32.2	-1.75
Effective energy	-	16.1	-	27.0	-	35.9
Flow rate	[ $\frac{kg}{h}$ ]	[ $kW$ ]				
Steam	43.21	31.6				
Groundwater inflow	49.22	1.10				
Groundwater outflow	-56.73	-5.81				
Soil vapour extraction	-70.34	-3.72				
Condensate	-4.10	-3.05				
Extraction well d/c	-16.84	-0.97				
Heat loss	-	22.3				

The energy stored within the porous medium of the tank can be calculated by means of Equations (3.5), (3.6) and (3.7). Therefore, the porosity and the bulk density of the soil (Tab. 3.3) and the initial temperature of about 24°C are needed. The average temperature at the end of phase **III** ( $t = 28.81 d$ ) and **IV** ( $t = 48.25 d$ ) of the steam injection of each layer was calculated by means of the program *Tecplot 360 2009<sup>TM</sup>* and listed in Table (3.8).

Taking into account the temperature difference, the total amount of the stored energy within the tank at the end of the respective phase yield  $Q_{pm}^{III} = 12.12 GJ$  (3.37  $MWh$ ) and  $Q_{pm}^{IV} = 12.27 GJ$  (3.4  $MWh$ ). Considering the total effective energy input of about  $Q_{eff} = 97.26 GJ$  and the stored energy at the end of phase **III**, yield a difference of about  $Q_t = 84.99 GJ$  (23.6  $MWh$ ) which is the total amount of energy losses across the system boundaries. Table (3.9) lists the amount of stored energy of the single parts within the tank and the corresponding percentage.

Table 3.8: Averaged temperatures of porous medium ( $t = 28.81 d$  &  $48.25 d$ )

Phase		<b>III</b>	<b>IV</b>
Layer	Height [ $m$ ]	Temperature [ $^{\circ}C$ ]	
Vadose zone ( <i>site 3</i> )	$3.1 \leq y \leq 4.5$	56.3	63.2
Transition layer 1 ( <i>GEBA</i> )	$3.0 \leq y \leq 3.1$	75.8	27.2
Aquitard ( <i>M2</i> )	$1.5 \leq y \leq 3.0$	93.1	93.4
Transition layer 2 ( <i>GEBA</i> )	$1.4 \leq y \leq 1.5$	98.3	98.1
Aquifer ( <i>site 3</i> )	$0.0 \leq y \leq 1.4$	83.0	80.3

Table 3.9: Stored energy in porous medium ( $t = 28.81 d$  &  $48.25 d$ )

Phase		<b>III</b>		<b>IV</b>	
Part		Energy [ $GJ$ ]	Percentage [%]	Energy [ $GJ$ ]	Percentage [%]
Soil	$Q_s$	6.45	53.2	6.64	54.1
Groundwater	$Q_{gw}$	5.51	45.5	5.44	44.3
Pore water in vz	$Q_{pw}$	0.16	1.3	0.19	1.6
Total	$Q_{pm}$	12.12	100	12.27	100



### 3.8.6 Tank Heat Loss Estimation

In Section 3.8.2 the horizontal expansion of the steam front extending to the walls of the tank is discussed. Hence, heat losses via the surrounding tank walls, namely the sides, the top and the bottom of the tank were determined by means of the equations given in Section 2.6. The determination of the heat losses required the separate consideration of the tank parts due to the occurrence of different processes and the set-up of the tank. Heat loss calculations are taken from VDI-WÄRMEATLAS (2006) [20].

- **Front:** Free convection at vertical plate (CHURCHILL AND CHU) and radiation

$$Nu = \{0.852 + 0.387[Ra \cdot f_1(Pr)^{1/6}]^2\}^2 \quad (3.11)$$

$$f_1(Pr) = \left[ 1 + \left( \frac{0.942}{Pr} \right)^{9/16} \right]^{-9/16} \quad (3.12)$$

- **Top:** Free convection at horizontal plate (heat emission at top face) and radiation  
Determination of Nusselt number for laminar flow,  $Ra \cdot F_2(Pr) \leq 7 \cdot 10^4$ , defined by CHURCHILL

$$Nu_m = 0.15 [Ra \cdot f_2(Pr)]^{1/3} \quad (3.13)$$

$$f_2(Pr) = \left[ 1 + \left( \frac{0.322}{Pr} \right)^{11/20} \right]^{-20/11} \quad (3.14)$$

- **Bottom:** Free convection at horizontal plate (emission at rear side) and radiation  
To determine the Nusselt number after CHURCHILL:

$$Nu_m = 0.6[Ra \cdot f_1(Pr)]^{1/5} \quad (3.15)$$

where  $f_1(Pr)$  can be calculated, cf. Equation (3.12) and the characteristic length is determined as  $l = (ab)/(2(a+b))$ .

- **Back and Sides:** Conduction through layers

As the back and side parts of the tank are next to the other tanks, conduction through the saturated soil and the *HDPE*-wall, which separates the cooling gap from the porous medium has to be considered. This requires the definition of the thermal conductivity coefficient  $k$ ,

$$\frac{1}{kA} = \frac{1}{\alpha_1 A_1} + \dots + \frac{1}{\alpha_i A_i} \quad (3.16)$$

Considering  $s$  as the wall thickness in meter and  $A$  the reference area in square meter.  $\alpha_i$  is calculated, following

$$\alpha_i = \frac{\lambda_i}{s_i} \quad (3.17)$$

The heat losses are calculated for steady state conditions at  $t = 28.81 d$ . Temperatures of the walls were measured randomly at different locations and postprocessed by means of *Tecplot 360 2009<sup>TM</sup>*. The total sum of heat losses was determined to  $22.3 kW$  due to the global energy balance of the experiment, cf. Section 3.8.5. The heat losses of the tank can be estimated applying the introduced approaches (Tab. 3.10).

Table 3.10: Heat losses at steady state ( $t = 28.81 d$ )

Part	Conduction [kW]	Radiation [kW]	Convection [kW]	Total [kW]
Top		0.46	0.19	0.65
Bottom		0.79	0.9	1.69
Front		1.98	5.03	7.01
Back	7.61			7.61
Sides	5.40			5.40
Sum	13.1	3.24	6.11	22.4

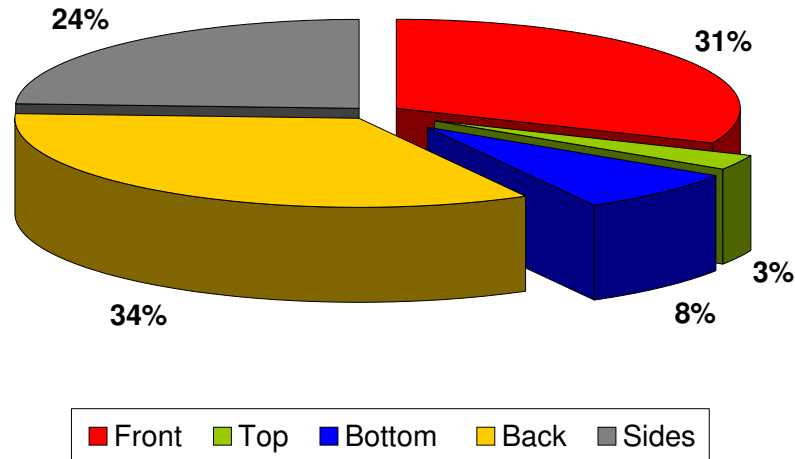


Figure 3.27: Energy loss percentage of single tank parts

The calculated total heat loss of about  $22.4 kW$  matches the heat losses determined by the energy balance. As temperatures were extrapolated and averaged per tank wall area, the calculations can only be considered as an estimation. Figure 3.27 visualizes the percentage of the total energy loss contributed by the single parts of the tank.

### 3.9 Comparison of 1D Numerical Model and Experiment

The observed heat distribution of the experiment was compared to the vertical temperature development simulated by a 1D numerical model. GUIDRY (2010) [15] set up a 1D transient model which was originally developed for heat conduction in solid media (SCHNEIDER (1955) [30]).

The purpose of the model is the simulation of the heat distribution in a low permeable layer by steam override in order to determine the heating-up time and the temperature levels in the layer.

The principle of the model is the subdivision of the system into a number of regular physical and geometrical volumes to consider the heat processes for one cell between the two surrounding cells. The relevant processes for the simulation of the heat propagation implemented in the model are heat convection, heat conduction and the heat loss to the environment. The change in internal energy over time is then equal to the difference between the injected heat and the heat loss. This results in a temperature increase for transient condition. A constant temperature at the bottom of the first cell and at the top of the last cell simulates the steam injection at the bottom and the temperature of the environment at the top. For detailed information it is referred to GUIDRY (2010) [15].

The 1D model successfully simulated the heat distribution of the flume experiment. The calculated final temperatures on different heights in the flume as well as the temperature trend over time was reproduced correctly.

The model was additionally adapted to the tank in order to simulate the heat distribution observed in this experiment (Fig. 3.28). Figure 3.29 is the spreadsheet which contains the input data of the model responsible for the simulation of the heat distribution.

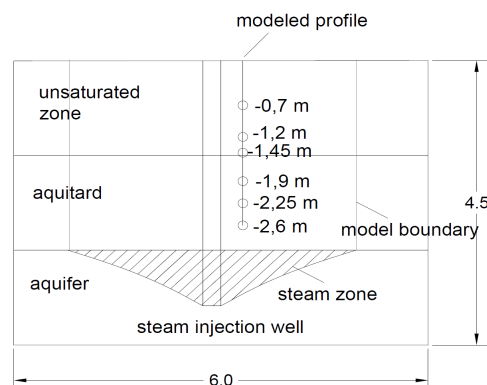


Figure 3.28: Set-up of 1D model for the tank simulation

Input data - Small tank constant injection		
<b>Model Dimensions</b>		
cells depth	0.34	m
cells length	0.34	m
total steam zone diameter	3.10	m
distance from end of steam zone	1.24	m
Total steam area	7.55	m <sup>2</sup>
<b>Soil characteristics</b>		
<b>Soil 2 - aquitard - mixture M2</b>		
porosity	0.46	-
water saturation	1	-
<b>Soil 3 - TCE - PCE layer middle sand</b>		
porosity	0.46	-
water saturation	1	-
<b>Soil 4 - unsaturated zone - middle sand</b>		
porosity	0.31	-
water saturation	0.3	-
<b>Heat transfer</b>		
Thermal conductivity dry sand	0.3	W/mK
Thermal conductivity water	0.59846	W/mK
Heat capacity water	4184.1	J/kgK
Heat capacity dry sand	850	J/kgK
Heat capacity air	1005	J/kgK
Thermal cond. Soil 2	0.437	W/mK
Thermal cond. Soil 3	0.437	W/mK
Thermal cond. Soil 4	0.263	W/mK
<b>Overall volumetric heat cap.</b>		
Cv Soil 2	3098231	J/m <sup>3</sup> K
Cv Soil 3	3098231	J/m <sup>3</sup> K
Cv Soil 4	1934692	J/m <sup>3</sup> K
average soil temperature	70	oC
average water density	977.76	kg/m <sup>3</sup>
soil density	2650	kg/m <sup>3</sup>
T environment	26	oC
Constant aquifer temperature	105	oC
surrounding soil temperature	26	oC
initial soil temperature	26	oC
surrounding soil thermal conductivity	1.13	W/mK
heat transfer coefficient air	65	W/m <sup>2</sup> K
<b>Height of the cells (cm)</b>		
-2.6	57.5	98.63
-2.25	40	92.29
-1.9	35	85.96
-1.45	37.5	79.65
-1.2	60	73.40
-0.7	70	67.24
<b>Steam injection</b>		
steam mass flux	44.0	kg/h
steam flow	73.956	m <sup>3</sup> /h
<b>Water thermal conductivity</b>		
	0.679	W/mK
<b>Steam properties</b>		
steam density	0.59817	kg/m <sup>3</sup>
dynamic viscosity	1.22E-05	kg/ms
Pr number	1.75	
<b>Soil grain size</b>		
d50	3.00E-05	m

Figure 3.29: 1D model spreadsheet for the simulation of the tank experiment

However, the model was not able to reproduce neither the maximum temperature nor the temperature trend correctly. Figure 3.30 shows the temperature trendlines of the experiment and the 1D model. The fast increase of the temperature results from the heat convection term determined by the steam injection rate. The contribution of the heat conduction term is negligible compared to the convection. This explains the temperature plateau as the convective term gets reduced after a certain time and no further temperature increase is achieved by the conduction term.

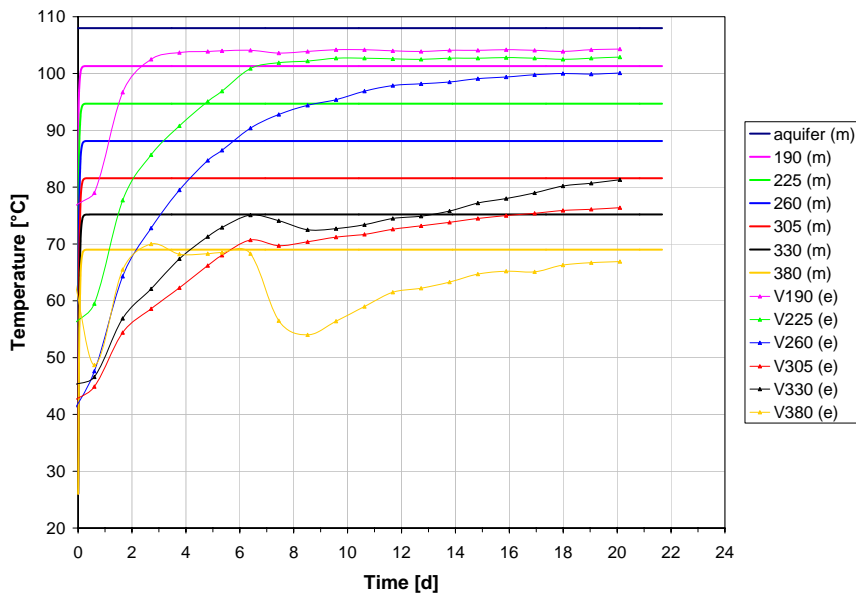


Figure 3.30: Comparison of temperature trendlines of 1D model and experiment

The main shortcoming of this model is the non-implementation of the heat mass balance. The model is not able to determine whether steam entered a cell or not. This prevents the consideration of a decline of the heat transfer coefficient from one cell to the next. The heat transfer coefficient is responsible for the convection and, therefore, the fast heat transport. A reduction of the heat transfer coefficient by hand yielded a better approximation to the experimental curves due to the fact that heat conduction increased but also resulted in a significant decrease of the maximum temperature.

The model could be successfully applied to the flume experiment due to the fact that convective processes were responsible for the heat distribution. In the tank experiment, however, the heat conductive process predominated the heating of the low permeable layer, which is responsible for the unsatisfactory applicability of the model.

## 3.10 Follow-Up Investigations

According to Section 3.8.3, it is assumed that an amount of about 3.5 kg of PCE remained in the saturated zone of the tank. Although the emissions by groundwater were significantly reduced from 1.8  $\frac{mg}{l}$  to 0.3  $\frac{mg}{l}$ , further remediation is necessary to achieve the desired complete recovery. Due to the limitation of the continuous steam injection technique to remediate the lower parts of the saturated zone, the technique has to be adapted or changed. The following observations emphasize the demand for a remediation technique modification:

- a) Decline of contaminant concentration in soil vapour extraction
- b) Steam injection achieved no further contaminant removal
- c) Contaminant removal from the unsaturated zone was higher in comparison with the saturated zone
- d) Partitioning of contaminant in the saturated zone
- e) Assumption: contaminant partitioned in lower sections or boundary areas, which were unaffected by the steam

Two thermally enhanced remediation options are (1) the intermitted steam injection technique and (2) the steam injection after complete drainage of the tank. The intermitted steam injection technique is derived from the cyclic steam injection which is a commonly applied technique in the petroleum industry to increase oil production (KLINGINGER (2010) [22]). In our case of remediation, steam is injected until the saturated zone is heated and steam breaks through at the extraction wells. The shutdown of steam injection then induces a fast increase of contaminant concentration in the extracted soil vapour, cf. Section 3.8.3. Due to high vacuum extraction further contaminant can be removed in an energy optimized way.

The drainage of the tank transforms the former saturated into an unsaturated zone. This benefits the steam propagation as buoyancy forces occurring in the saturated zone are not present. Hence, horizontal steam propagation is more wide-spread and the remediation of the former saturated zone is more efficient. As a matter of course, realization of this technique in the field is not as simple as in the experiment. However, lowering of the groundwater level can be achieved by means of sheet piling in combination with groundwater extraction wells, which then are able to extract the groundwater and the condensed steam enriched with contaminants.

## 4 Numerical Simulation

This part of the thesis describes the set-up of a numerical model for simulations of steam injection into a porous medium. It is intended to reproduce the heat distribution observed during the experimental investigation (Sec. 3.7). The results of the simulation are then compared with the results from the experiment. Since the main interest lies in the heat distribution, only the aqueous and the gaseous phase are considered. These two phases consist of the components air and water. Furthermore, any non-aqueous phases/components are neglected in the simulation. Investigations on steam propagation conducted by OCHS ET AL. (2003) [27] illustrated that the presence of a *NAPL* has no significant effect on the propagation of the steam front. Further, *NAPL* distribution was not investigated during the experiment, which is of importance if the simulation of contaminant distribution is of interest. However, two components have to be considered because the model domain comprises the unsaturated zone in addition to the saturated zone. The consideration of only one component (water) would be conform if only saturated zones are present. According to these statements the choice was made for a non-isothermal, two-phase, two-component modeling approach (*2p2cni*). Figure 4.1 shows the present phase states and their corresponding relation due to mass transfer processes. Modeling steam injection into saturated zones might cause various

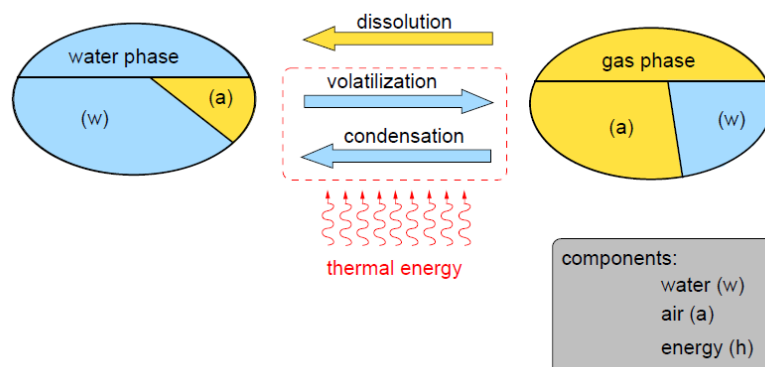


Figure 4.1: Phase states and mass transfer processes of a *2p2cni* model, taken from OCHS (2007) [28]

difficulties, for example numerical instabilities if the air component is not present. For further insight related to model stability, extensive investigations on simulating steam injection into saturated zones were accomplished by OCHS (2010) [28].

## 4.1 MUFTE-UG

The simulations were realized by means of *MUFTE-UG*. *MUFTE* is the abbreviation for Multiphase Flow, Transport and Energy model, containing physical model concepts and discretization methods for isothermal and non-isothermal multiphase-multicomponent flow and transport processes in porous and fractured media (HELMIG ET AL. (1998) [17]). *UG* stands for Unstructured Grid and comprises the data structures and solvers for the discretization of partial differential equations. *MUFTE-UG* was developed at the Universität Stuttgart (*IWS*) in co-operation with the Universität Heidelberg. The spatial discretization uses the *BOX* method where boxes are constructed around each node allowing fluxes to be calculated at their borders. The total flux between node  $i$  and  $j$  then is composed by the sum of all fluxes of the subcontrol volumes related to node  $i$  and  $j$ . For further insight on discretization techniques, I refer to HELMIG & HUBER (1998) [18].

## 4.2 Primary Variables

In order to describe our multiphase system a defined set of independent variables is needed, denoted as primary variables. The remaining variables, known as secondary variables, required to solve the non-linear system equations can then be derived by means of constitutive relationships such as (1) the capillary pressure constraint (Eq. 2.14) and (2) the saturation constraint (Eq. (2.6)). In Table 4.1, the different phase states with the corresponding primary variables for a  $2p2cni$  model are listed.

Table 4.1: Phase states and primary variables of the  $2p2cni$  model

Phase state	Present phases	Primary variables
Water phase	w	$x_w^a, p_g, T$
Gas phase	g	$x_g^w, p_g, T$
Both phases	w,g	$S_w, p_g, T$



### 4.3 Mathematical Model of a Non-Isothermal System

Balance equations are used in order to describe the behaviour of fluids in a porous medium. The balance equations comprise generally mass, momentum and energy. Considering non-isothermal, two-phase, two-component systems, not only mass but also energy has to be conserved in each phase and component. On the local scale (*REV*) the momentum balance is represented by the extended Darcy's law substituting the NAVIER-STOKES-Equation which describes flow on the pore scale. In the applied model we have to consider a gas phase consisting of air and steam and a water phase composed of water and dissolved air. In order to be able to solve the strongly coupled differential equations various simplifications such as the assumption of local thermodynamic equilibrium are used. As the explicit derivation of the REYNOLDS Transport Theorem and the balance equations are beyond the scope of this thesis, I refer for detailed information to HELMIG (1997) [16] and CLASS (2001) [10].

#### 4.3.1 Continuity Equation

According to mass conservation within a finite control volume following the continuity condition  $(\frac{dm}{dt})_{\Omega} = 0$ , one can formulate the mass balance equation for both components  $\kappa$ ,

$$\underbrace{\phi \frac{\partial}{\partial t} \left( \sum_{\alpha} \rho_{mol,\alpha} x_{\alpha}^{\kappa} S_{\alpha} \right)}_{\text{accumulation term}} - \underbrace{\sum_{\alpha} \nabla \cdot \left( \frac{k_{r,\alpha}}{\mu_{\alpha}} \rho_{mol,\alpha} x_{\alpha}^{\kappa} \mathbf{K} (\nabla p_{\alpha} - \rho_{mass,\alpha} \mathbf{g}) \right)}_{\text{advection term}} - \underbrace{\nabla \cdot (D_{pm}^{\kappa} \rho_{mol,g})}_{\text{diffusion term}} - \underbrace{q^{\kappa}}_{\text{sink/source term}} = 0, \quad (4.1)$$

with the porosity  $\phi$  and the intrinsic permeability  $\mathbf{K}$  of the porous media, the molar density  $\rho_{mol,\alpha}$  and mass density  $\rho_{mass,\alpha}$ , the saturation  $S_{\alpha}$ , the pressure  $p_{\alpha}$ , the relative permeability  $k_{r,\alpha}$  and the viscosity  $\mu_{\alpha}$  of the phase  $\alpha$ .  $x_{\alpha}^{\kappa}$  describes the mole fractions of the component  $\kappa$  in the particular phase  $\alpha$ .  $q^{\kappa}$  denotes the source/sink term and  $D_{pm}^{\kappa}$  the diffusion coefficient of component  $\kappa$ .

#### 4.3.2 Energy Equation

In accordance with the first law of thermodynamics, the energy of a system cannot be lost but only transferred from one state to another. Hence, a change of the system internal energy  $U$  is due to transport of energy across the borders and/or work performed by/to the system itself. In a porous medium, thermal energy is stored within the porous matrix and exchanged to and between the fluids.

With the assumption of local thermal equilibrium, which is reasonable for small pores and, therewith, small velocities, the temperatures of all phases are equal within

an averaging volume and, therefore, one equation for thermal energy is sufficient.

$$\begin{aligned}
 & \overbrace{\phi \frac{\partial}{\partial t} \left( \sum_{\alpha} \rho_{mass,\alpha} u_{\alpha} S_{\alpha} \right) + (1 - \phi) \frac{\partial}{\partial t} (\rho_s c_{p,s} T)}^{\text{accumulation term}} \\
 & - \overbrace{\nabla \cdot (\lambda_{pm} \nabla T)}^{\text{conduction term}} \\
 & - \underbrace{\sum_{\alpha} \nabla \cdot \left( \frac{k_{r,\alpha}}{\mu_{\alpha}} \rho_{mass,\alpha} h_{\alpha} \mathbf{K} (\nabla p_{\alpha} - \rho_{mass,\alpha} \mathbf{g}) \right)}_{\text{convection term}} \\
 & - \underbrace{\sum_{\kappa} \nabla \cdot (D_{pm}^{\kappa} \rho_{mol,g} h_{mol,g} M^{\kappa} \nabla x_g^{\kappa})}_{\text{diffusion term}} - \underbrace{q^h}_{\text{sink term}} = 0
 \end{aligned} \tag{4.2}$$

Where  $u_{\alpha}$  denotes the specific internal energy,  $h_{\alpha}$  the specific enthalpy,  $T$  the temperature, mass density  $\rho_{mass,\alpha}$  and specific heat capacity  $c_{p,s}$ .  $\lambda_{pm}$  is the thermal conductivity of the porous medium. Heat radiation is not considered in this approach as radiation in a porous medium is neglected in this application.

## 4.4 Model Set-up

In order to achieve a precise simulation of a physical problem it is indispensable to establish an accurate model. Thus, the established model has to include the characteristic processes as well as a robust numerical model. Furthermore, a well-thought-out model set-up completes the circuit. This model set-up involves

- geometrical parameters (grid of defined size, reproducing the processes with accuracy avoiding extensive computational resources)
- the boundary and initial conditions
- input parameters to describe the system (e.g. soil parameters)

The steam injection simulations were accomplished simulating the cross-section shown in Figure 4.2 over the height of the tank subtending the injection wells *I1* and *I2*. The corresponding cut through the tank shows the area reproduced in the simulation can be seen in Figure 4.3. The model measures a total length of about 5.7 m divided into three parts (1.83454 m + 2.03417 m + 1.83454 m) and 4.5 m of height. For reasons of simplification of the grid, the injection wells into the unsaturated zone are located at the same horizontal distance as the wells into the saturated zone. Furthermore, the extraction wells were moved to the left and right boundary at their corresponding height. In the following, the properties of the model set-up are discussed in detail as well as difficulties which emerged during the build-up process.

### 4.4.1 Two-Dimensional Approach

The decision for establishing a two-dimensional model was made because the realization of the experiment together with the set-up of a three-dimensional model would have been beyond the time frame of this thesis. The simulation of three-dimensional processes on a two-dimensional approach turned out to be the major challenge. This so-called downgrading of dimension can be declared responsible for the major error in the simulation. On the other hand, this may justify simplified implementations of other processes, e.g. implementing only linear capillary-pressure-relation, as the hereby produced errors are negligible compared to the error provoked by the downgrading.

The occurring difficulty can be easily illustrated. Steam injection into a porous medium is a radially symmetric process and the horizontal steam front propagation is highly dependent on the distance to the injection well. The further the front proceeds the larger gets the front area where the steam condenses and thereby heats the surrounding porous medium. This results in a continuous reduction of the propagation velocity. The consideration of only two dimensions prevents an accurate integration of this effect. Furthermore, the adjusted steam rates in the experiment have to be implemented into the simulation. In the experiment, the steam front propagated radially leading to the difficulty of adaption of the steam rate in the simulation.

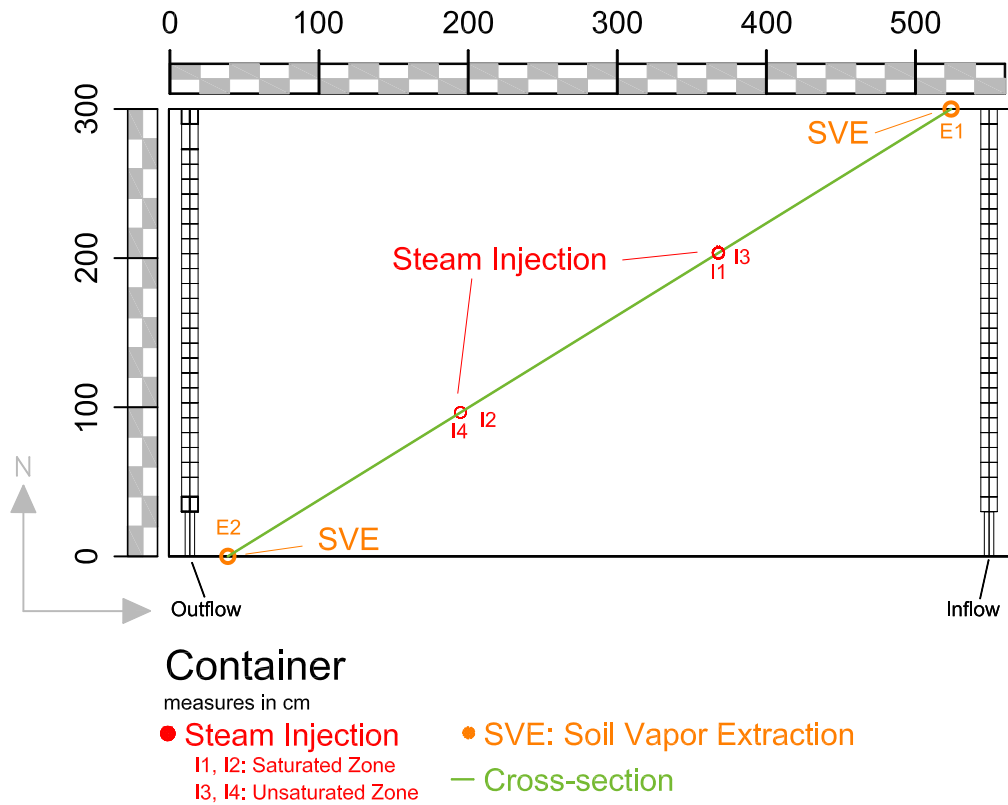


Figure 4.2: Topview of tank and cross-section

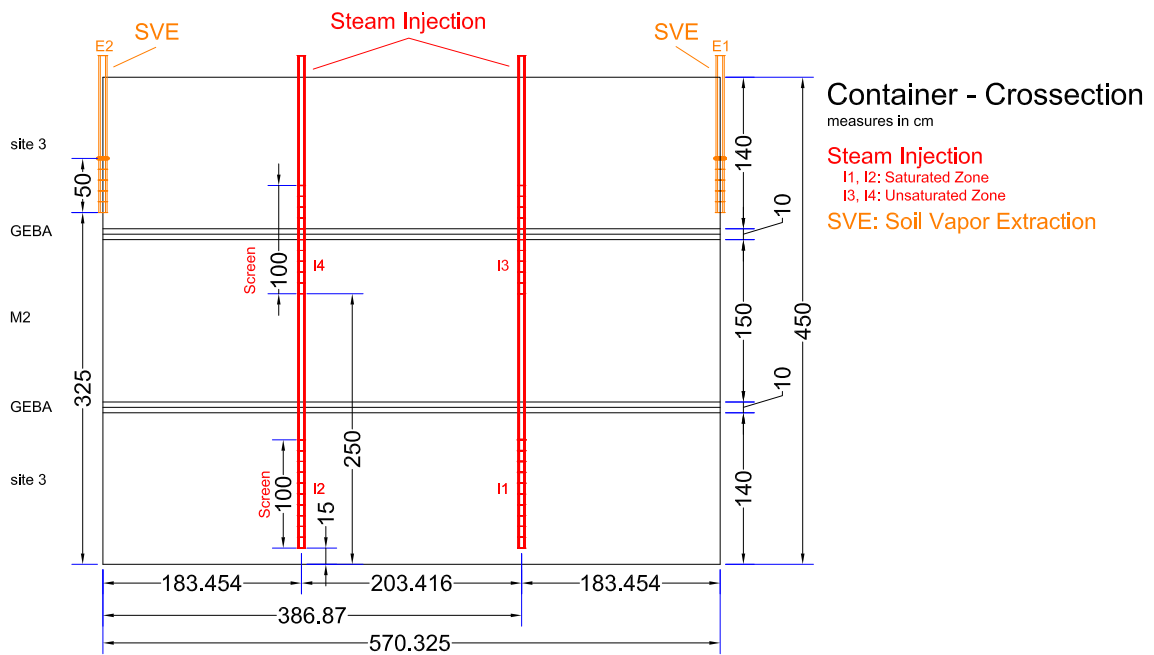


Figure 4.3: Front view of cross-section

Figure 4.4 illustrates the approach to determine the steam rate as well as its enthalpy of the simulation for the corresponding steam rate of the experiment. In general, the geometry of a two-dimensional simulation takes into account a user-defined length and height as well as standard depth of one meter. This was applied to the cross-section widening it to one meter of width over the entire length. After drawing an orthographic line at the central point between the two wells, an imaginary circle can be drawn with its center at the injection well subtending the points of intersection of the orthographic line and the widened borders of the cross-section. Assuming that the steam rate of the experiment corresponds to the circle, hence, the steam rate implemented in the simulation corresponds directly to the angle  $\varphi$  of the corresponding segment of the circle. As steam propagates towards opposite directions from the well, two similar segments of the circle have to be taken into account. This results in a factor  $f$  applied to the steam rate and enthalpy of every steam injection well (Eq. (4.3)).

$$\dot{m}_{sim} = \frac{2\varphi}{360} \cdot \dot{m}_{exp} = f \cdot \dot{m}_{exp} \quad (4.3)$$

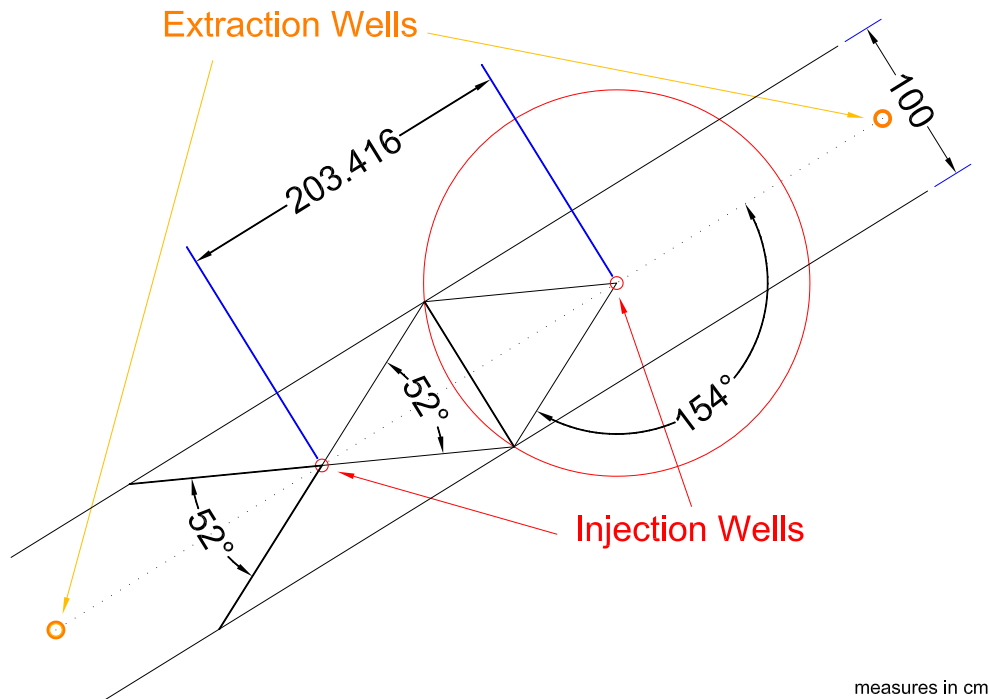


Figure 4.4: Approach to determine steam flow rate from experimental rate

### 4.4.2 Grid

One basic part of a numerical model is the grid, defining the number and location of the nodes where the equations are solved. The grid set-up is user-defined and different geometries and methods are available in order to achieve an effective grid providing local refinement if necessary.

In our case, a grid of rectangles is refined four times resulting in an average element size of around five centimeters due to the inequality of the boundary distance.

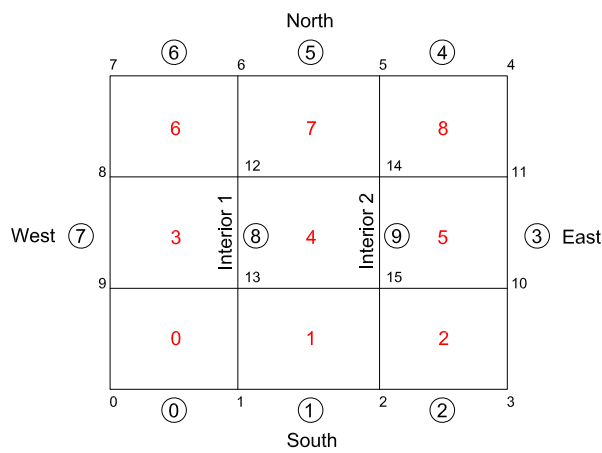


Figure 4.5: Grid set-up

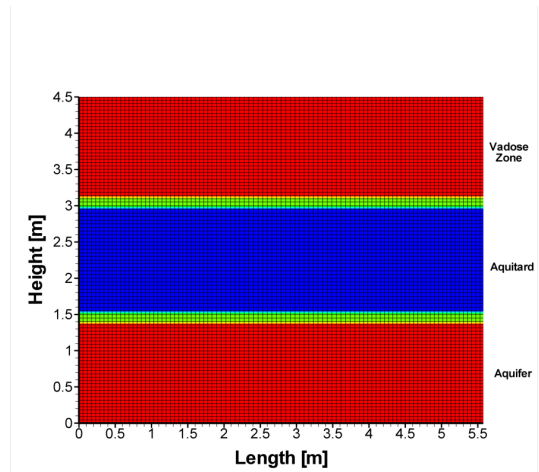


Figure 4.6: Refined grid

### 4.4.3 Model Parameters

The model parameters consist of the physical parameters of the wetting and non-wetting phase as well as the soil materials, which were used in the experiment. The model reproduces the different layers of materials which differ in their properties. In total, the properties of three different soils, *site 3* (1), *M2* (2) and *GEBA* (3), introduced in Section 3.4, were implemented in the model. However, first simulations showed that intrinsic permeability of *M2* has to be higher and, therefore, was set to  $1.0 \cdot 10^{-13} \text{ m}^2$ . The colored areas in Figure 4.6 mark the location of **site 3**, **GEBA** and **M2**. Anisotropy of the permeability is not considered in the model. The yellow bars result from *Tecplot 360 2009<sup>TM</sup>* averaging. Table 4.2 and 4.3 list the applied parameters.

Table 4.2: Physical parameters of wetting and non-wetting phase

Phase	Matter	Density $\rho_{mass,\alpha}$ [ $\frac{kg}{m^3}$ ]	Diffusion coefficient $D_{pm}^\kappa$ [ $\frac{m^2}{s}$ ]
Wetting	Water	1000	$1.0 \cdot 10^{-9}$
Non-wetting	Air	<i>Ideal gas law</i>	$2.6 \cdot 10^{-5}$

Table 4.3: Physical parameters of soils

Parameter	Unit	site 3	M2	GEBA
Density	[ $\frac{kg}{m^3}$ ]	2650	2650	2650
Porosity	[-]	0.31	0.4	0.46
Intrinsic permeability	[ $m^2$ ]	$1.75 \cdot 10^{-11}$	$1.0 \cdot 10^{-13}$	$1.1 \cdot 10^{-11}$
Heat capacity	[ $\frac{J}{kgK}$ ]	960	920	840
Thermal conductivity $S_w = 0$	[ $\frac{J}{m^3K}$ ]	0.44	0.44	0.44
Thermal conductivity $S_w = 1$	[ $\frac{J}{m^3K}$ ]	1.8	2.1	1.8
Residual water saturation	[-]	0.19	0.2	0.16
Residual gas saturation	[-]	0.05	0.05	0.05
Van Genuchten $\alpha$	[ $\frac{1}{Pa}$ ]	0.6	0.06	0.08
Van Genuchten $n$	[-]	6	1.5	5

#### 4.4.4 Initial and Boundary Conditions

Besides the grid and the model parameters, the formulation of adequate initial and boundary conditions is required in order to define the system. Initial conditions (Tab. 4.4) have to be defined for each point in the model domain at the beginning of the simulation according to the set of primary variables. The initial groundwater table is at the top of the *M2* layer at a height of 3.1 m. Additionally, the capillary fringe is implemented for  $3.1 \leq y \leq 4.5$  m adopting the function *Invert PC* which calculates the corresponding saturation  $S_w$  from the capillary pressure ( $p_c = 9.81 \frac{m}{s^2} * 1000 \frac{kg}{m^3} * (y - 3.1 m)$ ).

Boundary conditions (BC) define the interaction between the model domain and the surrounding environment. The applied boundary conditions in the model are of type *Neumann* and *Dirichlet*, cf. e.g. BEAR AND CHENG (2010) [7].

The four boundaries are divided into ten subparts as a result of the model set-up (4.5) consisting of three northern, three southern, one western, one eastern and two inner ones. The west and east boundaries are of type *Dirichlet* with fixed water saturations and hydrostatic pressure head or atmospheric pressure, respectively, and

Table 4.4: Initial conditions of model domain

Height [m] [m]	Saturation $S_w$ [-]	Pressure $p_w$ [Pa] [Pa]	Temperature $T$ [K] [K]
$0 \leq y < 1.4$	$1 - S_{gr,1}$	$P_{atm} + \rho g(3.1 - y)$	298.15
$1.4 \leq y < 1.5$	$1 - S_{gr,3}$	v.s.	v.s.
$1.5 \leq y \leq 3$	$1 - S_{gr,2}$	v.s.	v.s.
$3 < y \leq 3.1$	$1 - S_{gr,3}$	v.s.	v.s.
$3.1 < y \leq 4.5$	$Invertp_c(S_w)$	$P_{atm}$	v.s.

Table 4.5: *Dirichlet* Boundary conditions at east/west boundary

Boundary	Height [m]	Saturation $S_w$ [-]	Pressure $p_w$ [Pa]	Temperature $T$ [K]
East	$0 \leq y < 3.1$	$1 - S_{g,r1}$	$P_{atm} + \rho g(3.1 - y)$	313.15
West	$0 \leq y < 3.1$	$1 - S_{g,r1}$	$P_{atm} + \rho g(3.15 - y)$	313.15
Both	$3.1 \leq y < 3.2$	$S_{w,r1}$	$P_{atm}$	298.15
Both	$3.2 \leq y \leq 3.7$	$S_{w,r1}$	$P_{atm} - 9500$	298.15
Both	$3.7 < y \leq 4.5$	$S_{w,r1}$	$P_{atm}$	298.15

fixed temperatures. The extraction wells in the unsaturated zone are located at the east and west boundary in the range of  $3.25 \leq y \leq 3.75$  m. The extraction wells are simulated by reducing the pressure ( $p_w = p_{atm} - 9500$  Pa) at the specific location to simulate the vacuum as observed in the experiment, and thereby induce self-adjusting fluxes leaving the system. No-flow *Neumann* BC is applied to the south and north boundary for mass fluxes, impeding any mass transfer towards the surroundings. To allow for energy losses via the north boundary, *Dirichlet* BC is assigned with fixed temperatures of about  $T_{North} = 298.15$  K. The energy loss caused by the groundwater flow in the experiment is estimated by a constant temperature at the south boundary ( $T_{South} = 313.15$  K) self-adjusting a corresponding energy loss.

The steam injection wells at the inner boundaries for  $0.15 \leq y \leq 1.15$  m are of type *Neumann* determined by the mole fluxes of water and air and the corresponding enthalpy flux calculated from the steam rate of the experiment using the introduced approach (Sec. 4.4.1). The enthalpy of the injected steam is composed by 95% of saturated steam and 5% of water at 100°C (condensate). Apart from that, the inner boundaries are defined as “internal“ without taking account of any specifications.



#### 4.4.5 Energy Loss Approach

The introduced boundary conditions define the interaction between the model domain and the surrounding environment. As can be observed in the experiment, heat losses of the tank via the walls can not be neglected and, therefore, are implemented in the model. This results in self-adjusting energy fluxes by means of fixed temperatures at the walls. Furthermore, in a 2-d model, these energy losses do not only occur at the four actual boundaries, but also within the model domain at the "front" and the "back" which has to be taken into account. The implementation was realized following a linear approach given below:

$$q_l = f_l * (T_{node} - T_{init}) \quad (4.4)$$

where  $q_l$  [ $\frac{J}{s}$ ] is the energy flux,  $f_l$  a dimensionless energy loss factor,  $T_{node}$  [K] the temperature of the node and the specific time and  $T_{init}$  [T] the temperature at the beginning of the simulation (initial condition). The experiment was conducted with a model domain energy loss factor of 0.1. Energy losses within the model domain are processed in the model as sink terms implemented in the function *Source*.

## 4.5 Simulation Results

In this section, the results of the steam injection simulation are explained and discussed in detail. The procedure of the model development was the comparison of the heat distribution of the simulations with the experiment. Thereby emerging meanderings then resulted in modifications of the parameters responsible for the unsatisfactory reproduction. The parameters of importance for the heat distribution are the permeability and the thermal conductivity of the soils as well as the energy loss factor applied to the domain. Findings during the development process of the model such as the sensitivity of input parameter to heat distribution are discussed herein.

### 4.5.1 Estimates for Input Parameters

First simulations of steam injection into saturated zone with the developed model showed a rough trend of the accuracy of the model in reproducing the experimental observations. The simulations showed a decreased vertical heat propagation in the low permeable zone compared to the experiment. This confirmed the already stated assumption that the hydraulic permeability of the low permeable  $M2$  layer differs from the adopted hydraulic permeability of about  $k_{f,M2} = 2.4422 \cdot 10^{-7} \frac{m}{s}$  determined by HIESTER AND BAKER (2009) [19]. As a result of this, simulations with different intrinsic permeabilities of the  $M2$  layer were conducted in order to reproduce a more accurate heat distribution. The intrinsic permeability of about  $K_{M2} = 1.0 \cdot 10^{-13} m^2$  represented a satisfactory reproduction of the heat distribution.

Due to the fact that heat conduction gains relevance for heat distribution inside of a low permeable zone, thermal conductivity of the material can be added to the parameters of interest. Following the approach developed by SOMERTON (1974) [31], the thermal conductivity parameter of the porous medium in saturated conditions is of relevance as the low permeable layer is fully saturated at initial state. In the literature, values of  $\lambda_{pm}^{S_w=1}$  can be found in the range of  $1.17 \frac{W}{mK}$  (SOMERTON) and  $4 \frac{W}{mK}$  (THE ENGINEER TOOLBOX).  $\lambda_{pm}^{S_w=1} = 2.1 \frac{W}{mK}$  was chosen to approximate the reproduction of heat conduction. Furthermore, simulations to investigate the influence of the energy loss factor were conducted.

### 4.5.2 Sensitivities of Input Parameters

In the determination process of the input parameters, various simulations were conducted taking account of the alteration of input parameters concerning the low permeable  $M2$  layer. The herein observed effects on the heat distribution or propagation, respectively, were investigated and are discussed below. The standard configuration of the simulation was determined by the steam injection rate of about  $\dot{m}_{inj} = 25 \frac{kg}{h}$  at  $I1$  and  $I2$ . The intrinsic permeability of about  $K_{M2} = 1.0 \cdot 10^{-13} m^2$ ,  $\lambda_{pm,M2}^{S_w=1} = 2.1 \frac{W}{mK}$  for thermal conductivity, porosity  $\phi_{M2} = 0.4$  and neglected energy losses within the domain. The procedure was the modification of only one parameter at a time to be

able to quantify its effect. Figure 4.7 to 4.10 illustrate the influence of the parameter modification on the heat propagation. For better visualization, the temperature isoline at  $373.15\text{ K}$  ( $100^\circ\text{C}$ ) is drawn in the plots.

Table 4.6: Configuration of  $M2$  parameters

Parameter	Unit	Standard	Variation 1	Variation 2
Intrinsic permeability	$[m^2]$	$1.0 \cdot 10^{-13}$	$7.5 \cdot 10^{-14}$	$2.5 \cdot 10^{-13}$
Thermal conductivity	$\frac{W}{km}$	2.1	1.17	3.0
Porosity	$[-]$	0.4	0.3	0.5
Heat loss factor	$[-]$	0	0.5	1

- **Permeability**

Hydraulic conductivity describes the rate at which a fluid flows through a porous medium. Considering steam injection, hydraulic conductivity can then be considered as a main parameter responsible for heat distribution mainly driven by convection. The hydraulic conductivity of an aquifer is determined by field tests, e.g. slug test (BOUWER AND RICE (1976) [9]). In many cases permeability differs by orders of magnitude as a cause of heterogeneities. With this background knowledge the effect on heat distribution as a result of an increased/decreased intrinsic permeability of the low permeable zone  $M2$  to about  $K_{M2} = 7.5 \cdot 10^{-14}\text{ m}^2$  and  $2.5 \cdot 10^{-13}\text{ m}^2$ , respectively, was investigated. Figure 4.7 compares the effect of the altered intrinsic permeability on the heat propagation in the low permeable  $M2$  layer at  $t = 3\text{ d}$ . The increase of the intrinsic permeability from  $1.0 \cdot 10^{-13}\text{ m}^2$  to  $2.5 \cdot 10^{-13}\text{ m}^2$  resulted in a significant acceleration of the heat propagation in the low permeable layer. In contrast, reducing the hydraulic permeability to  $7.5 \cdot 10^{-14}\text{ m}^2$  hindered the propagation of the steam front in the aquitard. Further, the steam front velocity was reduced and the steady state condition was already reached after 52 hours.

- **Porosity**

Porosity is a soil parameter which is determined by the averaging process over a defined volume and is defined as the fraction of the volume of voids over the total volume. On the local scale, however, porosity is not equal at each location but differs due to inequality of grain size and possible mechanical impacts, e.g. compression. The porosity of the low permeable  $M2$  layer was determined to  $\phi_{M2} = 0.4$  (HIESTER ET AL. (2009) [19]). Therefore, effects on the spreading of the heated zone were investigated for the porosities  $\phi = 0.3$  and  $0.5$  (Fig. 4.8). The difference in heat propagation is almost negligible considering these modified values of porosity. One can observe a minimal faster expansion of the steam region for the reduced porosity  $\phi = 0.3$  than for the other configurations.

- **Thermal Conductivity**

Simulations with distinct values of the thermal conductivity parameter were conducted in order to investigate its impact on the heat distribution. Figure 4.9 depicts the effect of thermal conductivity of the saturated porous medium from  $\lambda_{pm,M2} = 2.1 \frac{W}{mK}$  to  $1.17 \frac{W}{mK}$  (SOMERTON) and  $3.0 \frac{W}{mK}$ . A heat distribution snapshot after three days is chosen where two temperature levels ( $373K$  and  $333K$ ) demonstrate the heat distribution. A reduced thermal conductivity yielded a more “well-defined“ steam front whereas an increase resulted in a more wide-heated area in front of the steam region. Furthermore, the higher thermal conductivity resulted in a more wide-spread heated region in front of the steam front but also in a less far propagated steam front and vice versa.

- **Energy Loss Factor**

The energy losses at the boundaries observed in the experiment were estimated by a self-adjusting flux as a result of fixed temperatures at the boundaries. Within the model domain energy losses were implemented by means of a simple, linear approach using the energy loss factor  $f_l$ . In Figure 4.10, snapshots of the simulation reflecting the influence of the heat loss approach inside the model domain on the heat distribution are shown. Simulations were conducted with  $f_l = 0, 0.5,$  and  $1$ . It is evident that the influence of the energy loss within the model domain has a strong effect determined by the magnitude of the factor. This arises from the applied sink term to each node element of the model domain.

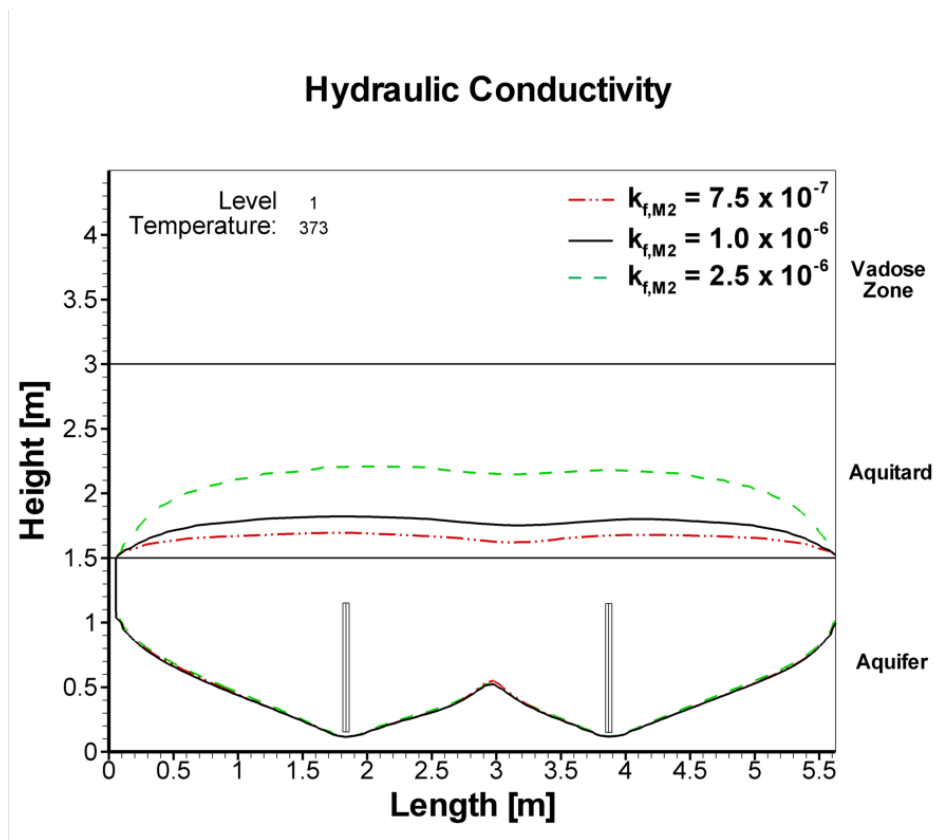


Figure 4.7: Effects of intrinsic permeability  $K_{M2}$  on the heat propagation;  $t = 3d$

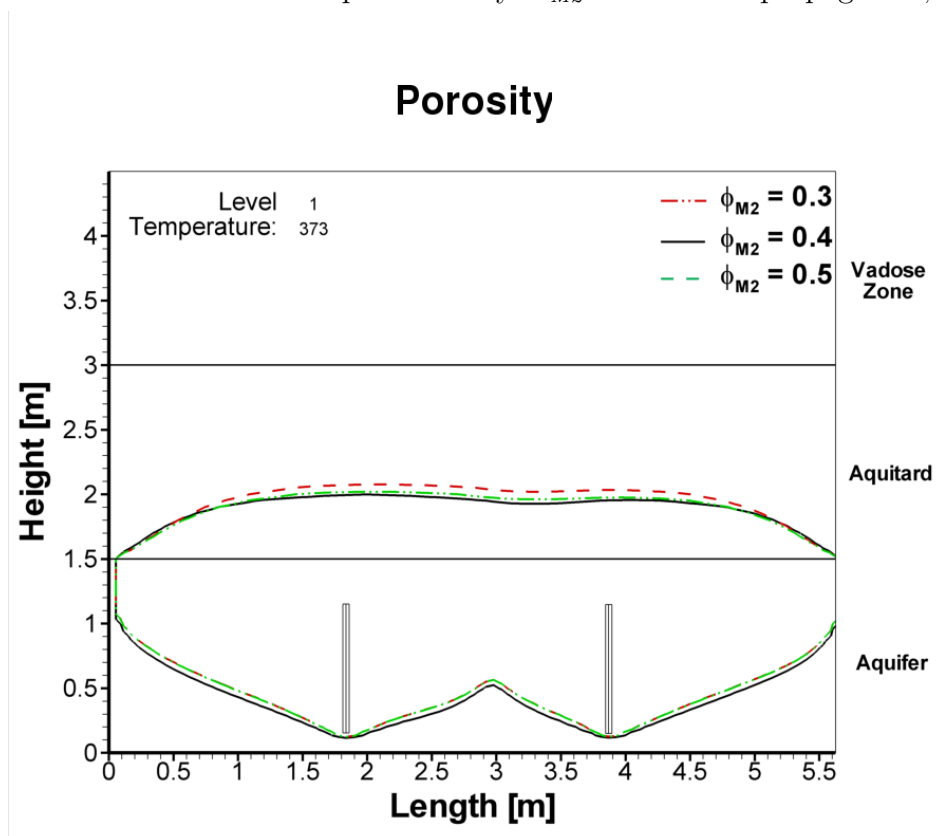


Figure 4.8: Effects of porosity  $\phi_{M2}$  on the heat propagation;  $t = 5d$

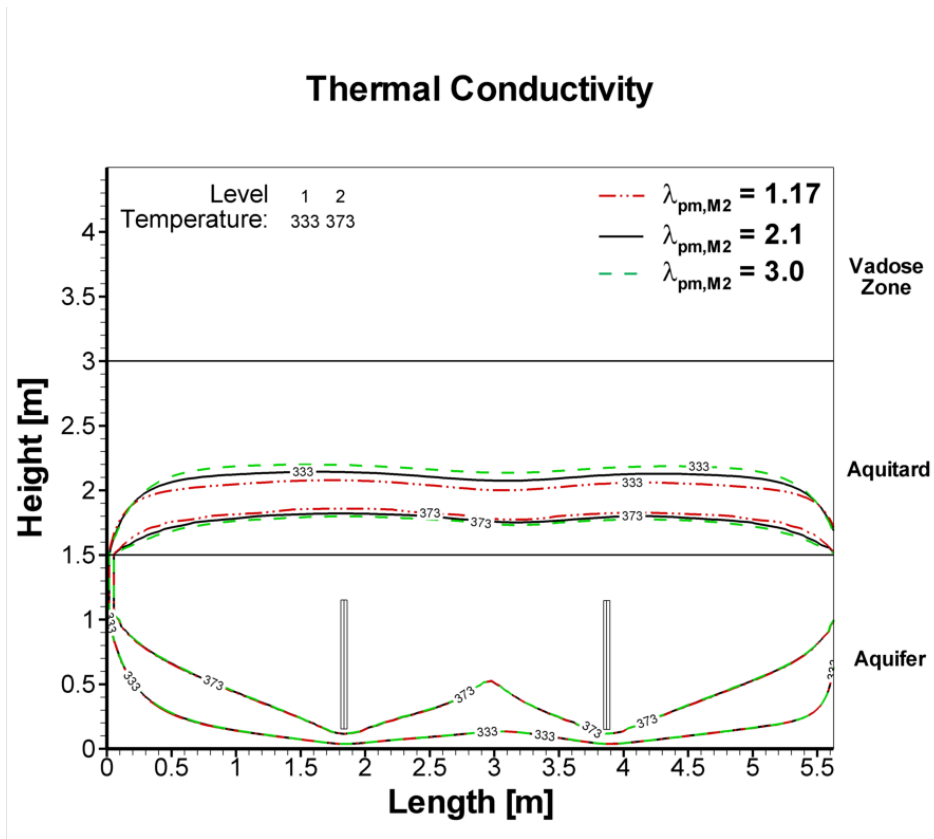


Figure 4.9: Effects of thermal conductivity  $\lambda_{pm,M2}^{S_w=1}$  on the heat propagation;  $t = 3d$

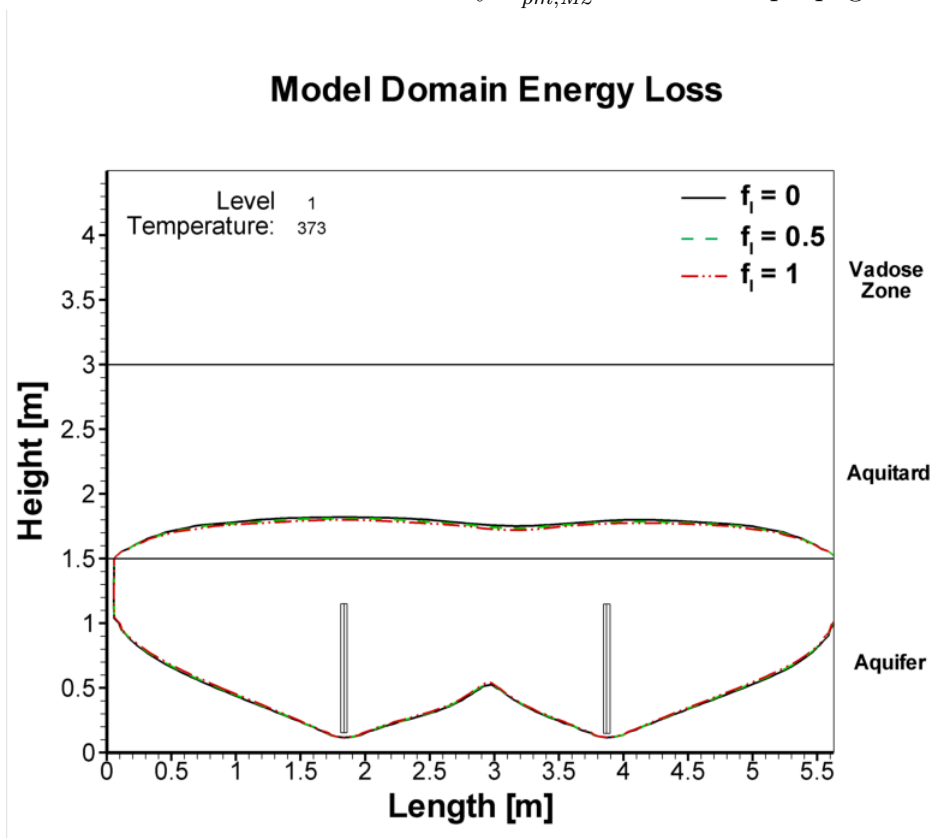


Figure 4.10: Effects of model domain energy loss  $f_l$  on the heat propagation;  $t = 3d$

#### 4.5.2.1 Discussion of Sensitivity Analysis

Comparing Figure 4.7 to 4.10, one can easily observe the influence of the parameter modifications. An increase of the intrinsic permeability resulted in a faster distribution of the steam front (area at temperature of about 100°C) and, therefore, a more far-reached heating of the aquitard after the equal period. An increased thermal conductivity affected only the area of the model domain in front of the heat front, having almost no influence on the vertical velocity of the front distribution. Considering this, it is certain that for better permeable soils heat conduction is a negligible process. Contrary to this, if the purpose is the heating of a very low permeable soil where heat convection is reduced enormously, the significance of the conduction process rises considerably concerning the heat distribution.

In addition to the intrinsic permeability, porosity affected directly the propagation of steam, however, only to a minor extent. A decreased porosity implies a smaller volume available for fluid transport, accelerating heat convection. Compared to the thermal conductivity, both parameters showed only a marginal influence on heat distribution compared to the intrinsic permeability. The energy loss factor of the model domain can be denoted as a calibration parameter to balance emerging reproduction errors as a result of the downgrade from three to two dimensions. One observed a reduced vertical heat distribution as an effect of the applied energy losses leading also to a faster approach towards steady state condition. In conclusion, the intrinsic permeability appeared to be the main soil parameter of importance for heat distribution matters followed by the porosity and the thermal conductivity.

## 4.6 Comparison of Experiment and Simulation

The model, set up in Section 4.4 was applied for simulations of steam injection conducted in the experiment, cf. Chapter 3. The specific approach was based on parameters known from the physical features of the experimental set-up and parameters evaluated during running of the experiment. The model was further calibrated by the ongoing experimental measurements to adjust parameters and calculations accordingly. Another variable that had to be taken into account in the simulation was the inconsistency of steam supply during the running of the experiment, cf. Figure 3.11. Thus, changes in flow rate had to be considered and, therefore, were implemented into the simulation.

### 4.6.1 Comparison of Heat Distribution

In this section the simulation results are compared to the heat distribution observed in the experiment and the mismatch is discussed. The parameters applied in the model are given in Section 4.4. Figures 4.12 to 4.15 depict the heat distribution of the experiment and the simulation by comparison. The snapshots show a relatively high deviation of the heated region when comparing simulation and experiment. It is certain that the visualization of the horizontal heat distribution in the experiment is underestimated. This can be explained by the shift of the steam injection wells cross-section which was not in line with the temperature sensors. The further from the center, i.e from the sensors the further the inaccuracy increased as temperature at each node in the tank was determined by means of the *Kriging* method. The vertical heat distribution, however, is more precisely represented. Premature heating of the vadose zone and the upper part of the aquitard was induced by heat conduction originating from the steam injection wells. The absence of temperature sensors above a height of 2.6 m around the injection well *I1* lead to the visible asymmetry at a later date. In the simulation, however, horizontal steam propagation is assumed to be overestimated due to the fact that a two-dimensional model was used.

Comparing simulation and experiment, the reproduction of vertical heat distribution was largely correct up to 15 days of steam injection. Afterwards, the heating of the vadose zone was observed in the simulation but not in the experiment. Heat distribution reached steady state in the experiment after 28 days. The simulation showed as well a trend towards steady state after 28 days, however, the vadose zone was then already heated to a large extent. The additional steam injection into the vadose zone resulted in the heating of the main part of the unsaturated zone as shown in the simulation snapshot at  $t = 31d$ . Whereas in the experiment, only a marginal heat expansion was observed. The impact of the extraction wells is assumed to play a major role responsible for this behaviour. The extraction wells in the numerical model, located at the west and east boundaries induced a faster horizontal expansion as a result of the applied vacuum.



In the experiment, the extraction wells were located at planes which lie in different depths, based on this view. Hence, horizontal heat expansion in the vadose zone was reduced as the heat flux pointed into the depth towards the extraction wells.

In Figure 4.11, the temperature trendlines at the top of the aquitard ( $H = 2.95 \text{ m}$ ) of the experiment and the simulation are visualized. The time difference in reaching the target temperature of about  $90^\circ\text{C}$  between the simulation and the experiment was about one day.  $90^\circ\text{C}$  was reached in the simulation after 14.91 days and 15.93 days, respectively, in the experiment.

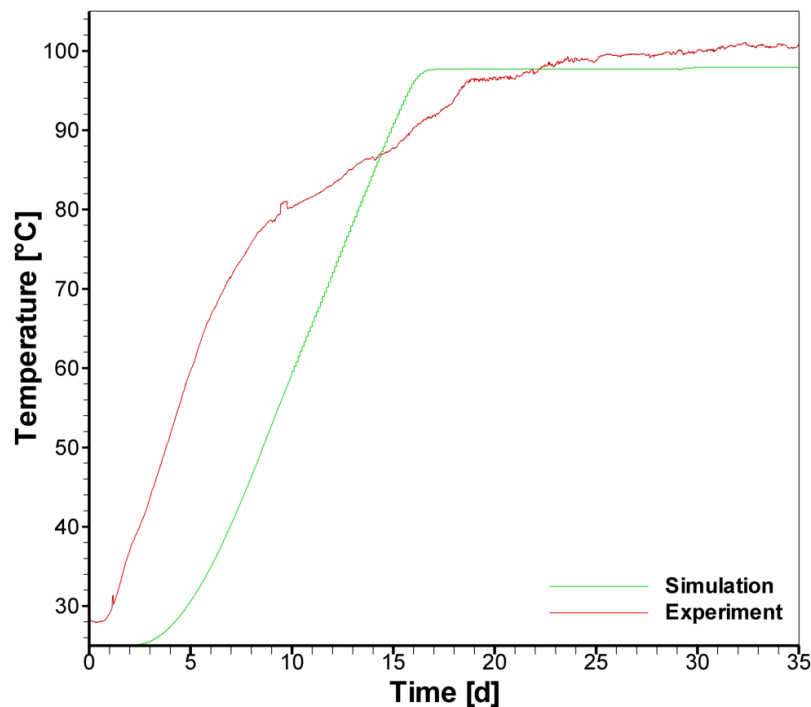


Figure 4.11: Temperature trend of simulation and experiment

The experiment showed an earlier temperature increase compared to the simulation and a more distinctive deceleration after the steam rate reduction at  $t = 8.8 \text{ d}$ . The deceleration, however, was not reproduced in the simulation. Furthermore, we observe that heat conduction in the simulation affected only a defined region in front of the steam front. Whereas in the experiment, the heat conduction had a more far-reaching influence. In the experiment, the spot of interest at the top of the aquitard was affected additionally by the lateral heating from the injection wells. This explains the earlier temperature rise and the higher sensitivity to the steam rate change.

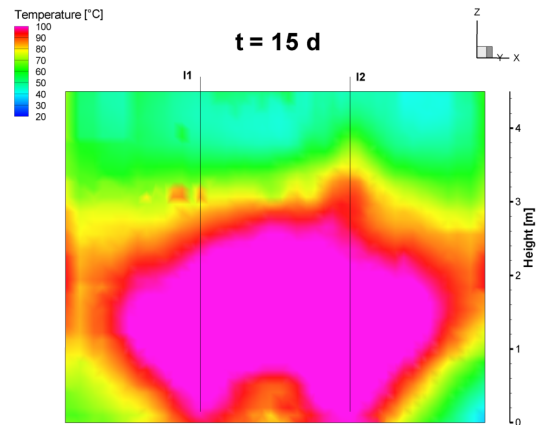
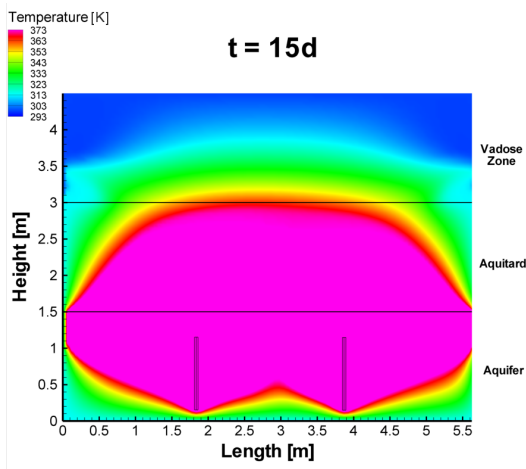
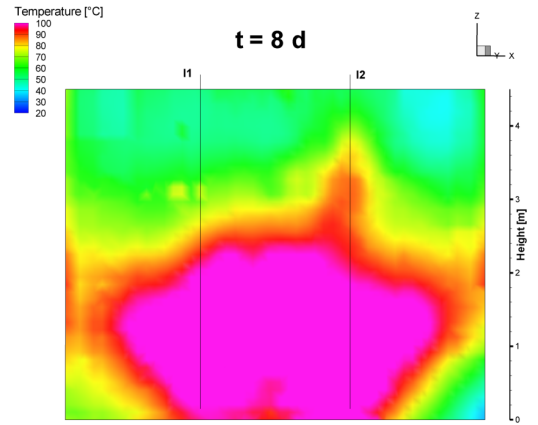
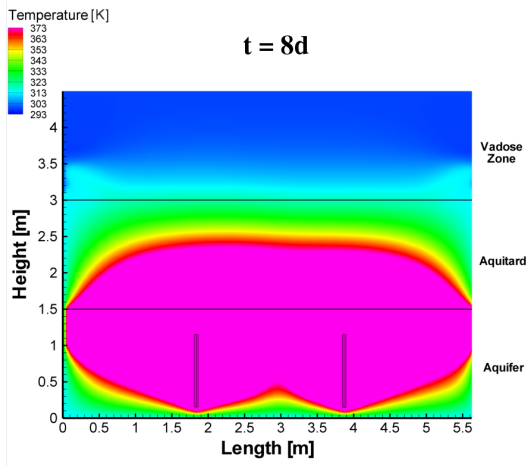
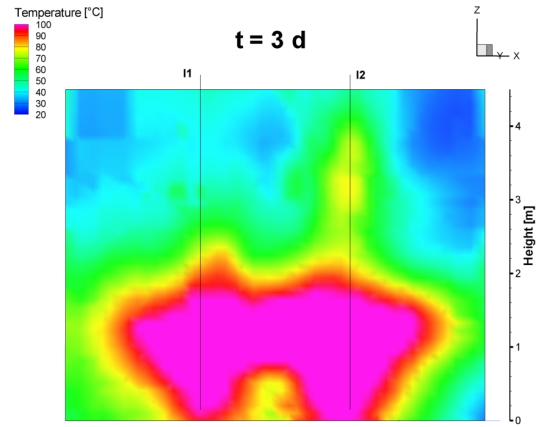
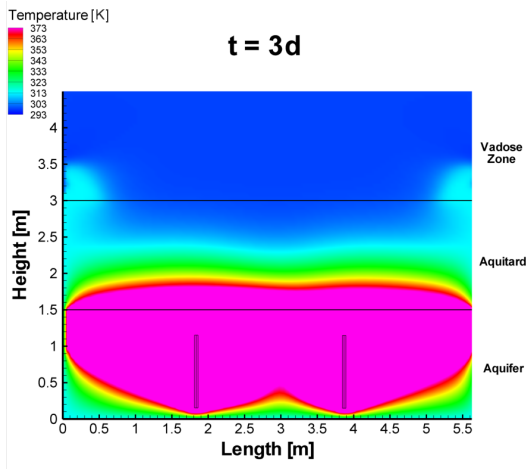


Figure 4.12: Simulation

Figure 4.13: Experiment

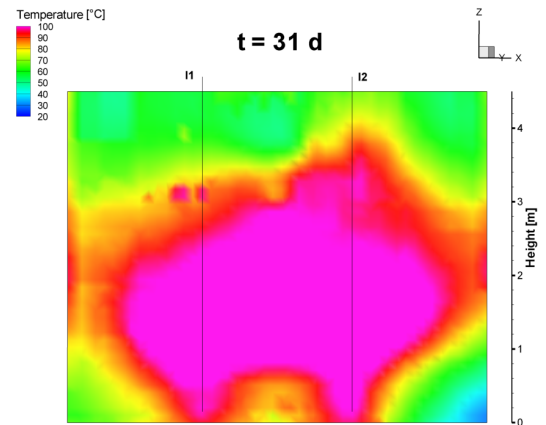
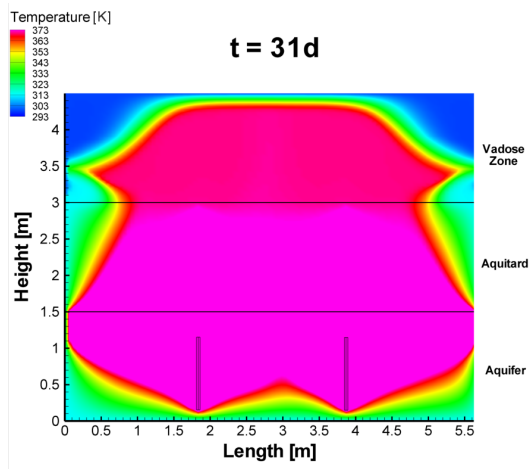
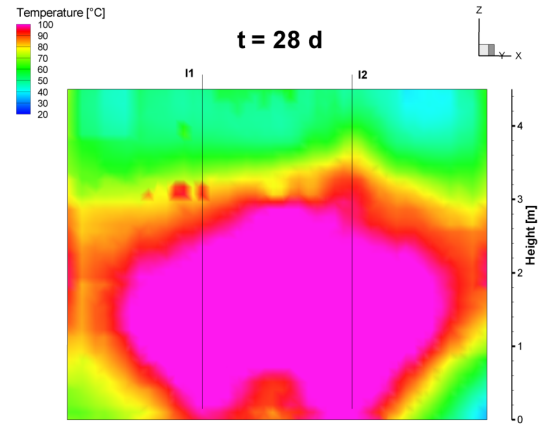
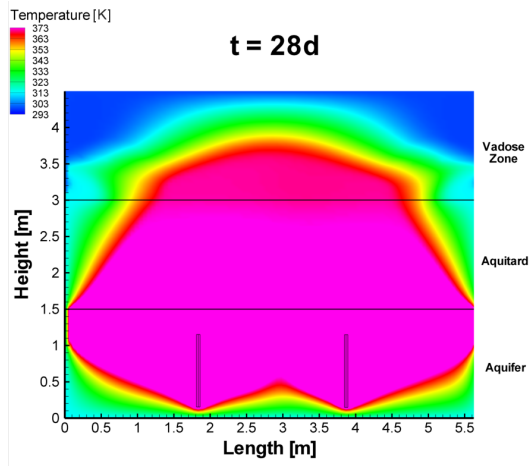
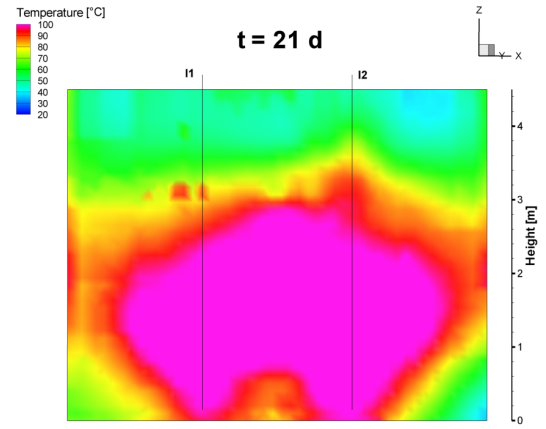
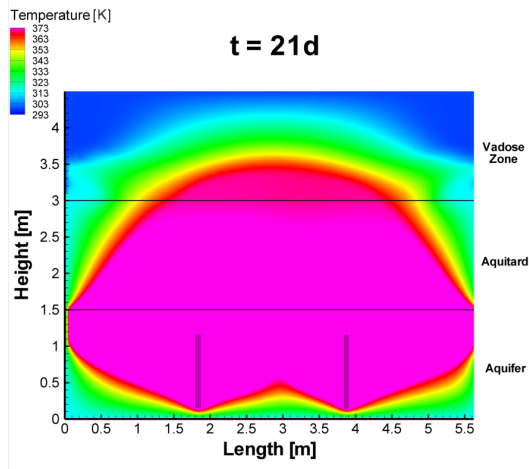


Figure 4.14: Simulation

Figure 4.15: Experiment

### 4.6.2 Effect of Steam Injection Discontinuity

This section describes the effects of the implementation of steam flow variation as observed in the experiment and, therewith, also steam generator breakdowns at the beginning of the experiment. The discontinuity of steam injection and the breakdowns, respectively, caused significant difficulties during the simulation procedure. When steam injection stopped, no more energy was injected into the system and the established steamed zone started to collapse. Steam condensed and water flowed back into the cells previously consisting of steam provoking a cooling of the already heated region. This caused strong oscillations of gas phase pressure and had an impact on the solvers which led to an increased simulation time because of the reduction of time steps. For this purpose, the pressure trend over time was recorded at the node with the coordinates  $(x, y) = (1.84 \text{ m}, 0.635 \text{ m})$  at the steam injection.

Figure 4.16 depicts the pressure trend for a constant injection rate ( $\dot{m}_{inj} = 25 \frac{\text{kg}}{\text{h}}$ ) as well as the experiment-adapted rate ( Fig. 3.11). Pressure trend of experiment-adapted injection rate revealed pressure drops caused by the two steam injection breakdowns after 28.6 and 35.5 hours as well as pressure jumps provoked by changes in injection rate. In Figure 4.17 and 4.18, the heat distribution and water saturation trend after 28, 36 and 40 hours of steam injection are depicted (steam breakdown at  $t = 28.6 \text{ h}$ ). One can observe a decline in temperature and by then heated region as well as a total collapse of the steamed zone as former steam condensed. This is illustrated by the water saturation. The lower water saturation in the aquitard was caused by ascending air displacing the water.

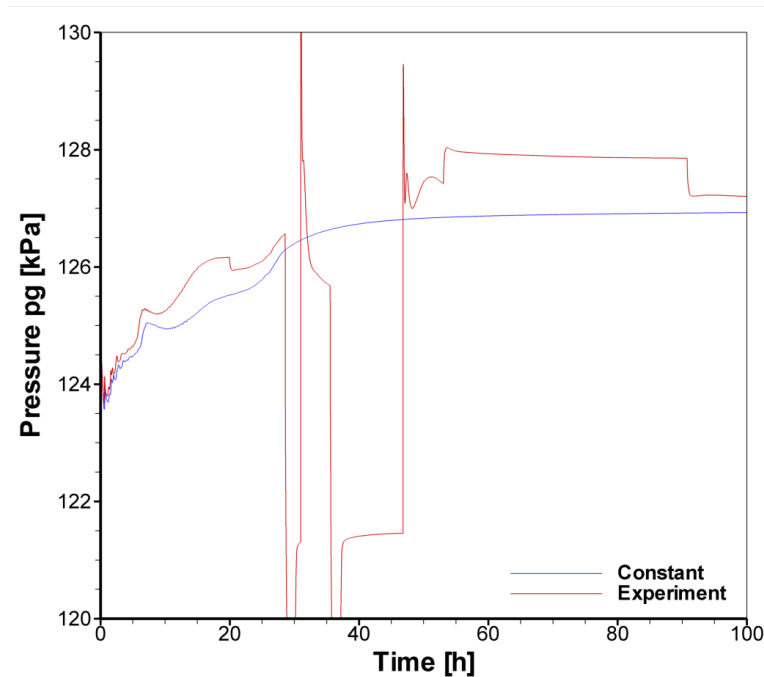


Figure 4.16: Pressure trend at injection node

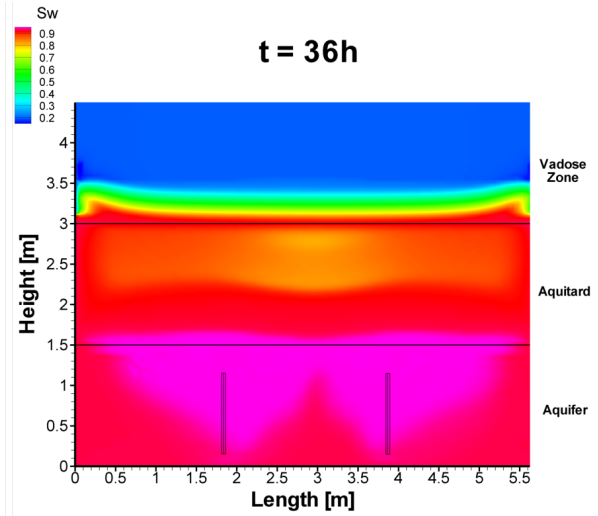
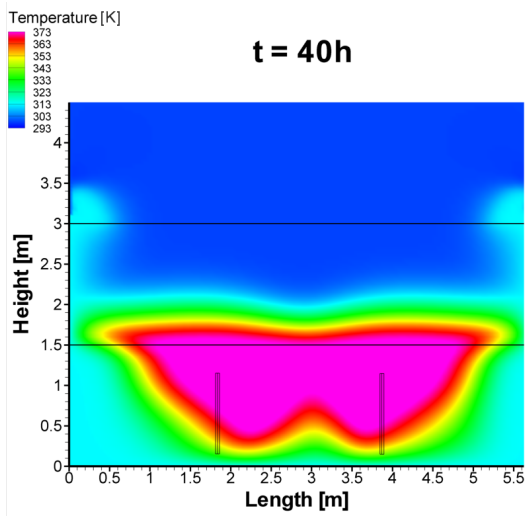
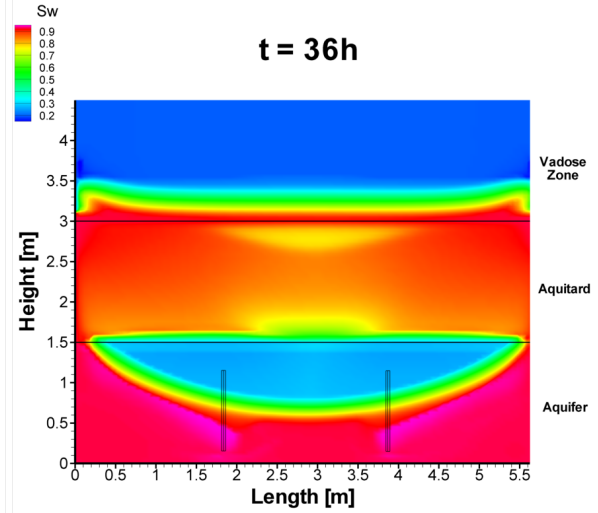
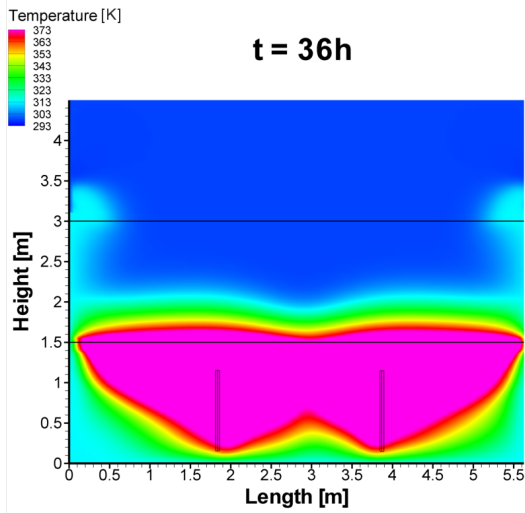
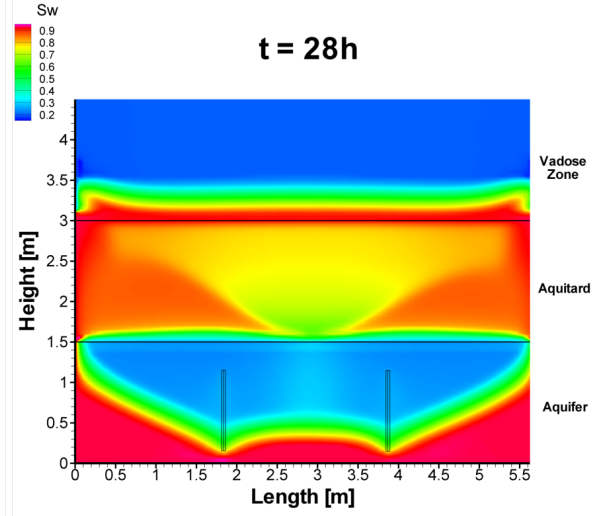
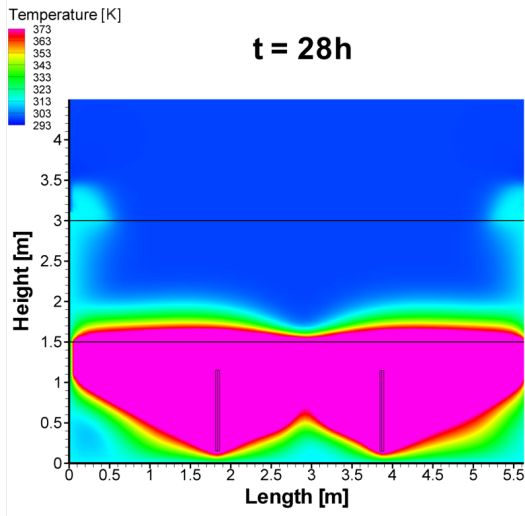


Figure 4.17: Heat distribution trend ( $T$ )

Figure 4.18: Water saturation trend ( $S_w$ )

## 4.7 Shortcomings of Model

Establishing a two-dimensional simulation model for a three-dimensional problem can present an outstanding challenge to the modeller. It was selected in order to reduce computing time and as a result of the given time frame for the realization of the experiment and the numerical model. However, an application of a two-dimensional concept yields often satisfying simulations for an aquifer, since groundwater flow, for example, can be considered as an unidirectional process. Hence, the third dimension can then be neglected and an accurate reproduction is still guaranteed. Steam injection, however, is a radial process and, therefore, neglecting the third dimension is only applicable under certain circumstances. For example, this may comprise steam injection into a wide-stretched aquifer to impede direct interactions between the steam front and the boundaries or in comparison with a two-dimensional experiment. In our case, none of these examples can be applied which has to be considered when conclusions on the accuracy of the simulation are drawn.

One of the main shortcomings of the simulation is the determination of the steam flow rate applied to the simulation in order to correspond to the flow rate of the experiment (Sec. 4.4.1). The simulation approach can only be regarded as an estimation, since inaccuracies are introduced by reducing the process to two dimensions. Furthermore, during the first simulations it became evident that the boundaries represent a major source of variation, generating in particular difficulties in the accurate reproduction of the experimental conditions. In the experiment only saturated steam was injected. However, problems occurred during simulations when air fell below a certain flow rate ( $\dot{n}_a = 0.001 \frac{\text{mol}}{\text{s}}$ ). This affected directly the computing time which increased enormously or resulted in a simulation crash if less air was injected. OCHS ET AL. (2010) [26] identified the behaviour as a result of the local disappearance of the air component leading to convergence problems. In order to avoid the occurrence of this problem the injection of air was allowed in the simulations.

Due to the fact that steam propagated until reaching the boundaries caused difficulties in the correct assignment of the boundary condition. This can be explained in the following way. During the experiment, the injected steam applied an overpressure displacing the aquifer water in all directions. The displaced water then left the tank via gravity flow. Thus, this directly affected the prevailing pressure in the aquifer responsible for the vertical pressure gradient. This experimental condition could not be directly applied in the model with the available boundary conditions. In addition, water was hindered in flowing into the third dimension. The following scenarios shall demonstrate the two options.

- *Dirichlet Boundary Condition*

Assigning *Dirichlet BC* considering fixed water saturation, (hydrostatic) pressure and temperature, heat distribution is assumed to be underestimated. The low permeable layer in the vertical center of the model domain hinders the injected steam in rising. Thus, it accumulates below the aquitard displacing water which

leaves the system via the boundaries ( $0 \leq y \leq 1.5$  m) and reduces the actual pressure. The underestimation of the pressure then reduces the pressure gradient responsible for the vertical steam propagation and, therewith, heat distribution.

- *Neumann Boundary Condition*

Assigning *Neumann BC* considering no-flow condition for mass fluxes results in the opposite effect. Since there is no possibility for the water to leave via the boundaries, pressure rises until the pressure gradient suffice for pushing the water and steam, respectively. Thus the overpressure in the aquifer is overestimated and, therewith, results in a faster heat distribution in the aquitard.

It became evident that assigning *Dirichlet BC* is closer to reality than *Neumann* no-flow condition and was applied in the model.

Furthermore, the groundwater flow observed in the experiment from one to the other end of the tank, passed the cross-section reproduced in the simulation. The fixed groundwater inflow with a temperature of around 18°C (from the degasing installation), imposed a cooling effect at the bottom side of the steamed zone. However, the temperature gradient between steam and groundwater flow was not equal at different points of the cross-section in the experiment as the groundwater flow did not pass the cross-section perpendicularly (Fig. 4.2). The flow in the model could only be implemented from one boundary to the opposite. Groundwater outflow in the experiment was self-adjusted by the gravity flow which could only be implemented by means of *Dirichlet BC* leading to the introduced problems. Hence, the cooling effect was applied by defining constant temperature at the south boundary provoking an energy flux leaving the system. Further unpredictabilities due to the quantification of the cooling effect have to be considered.

The consideration of energy losses within in the model domain into the third dimension were implemented following the approach introduced in Section 4.4.5. However, the determination is arbitrary as they were not determined experimentally and no further knowledge exists. Thus, the energy loss factor leaves ample room for further calibration and provides a mean to reduce the overestimation of the heat distribution.

## 5 Summary and Conclusion

Contamination of the subsurface by contaminants and possible remediation techniques are important topics in environment related discussions, nowadays. Different techniques such as enhanced soil vapour extraction have been developed and improved to achieve a best possible contaminant recovery for the unsaturated zone. Distribution of the injected heat, e.g. in form of steam, is of utmost interest. The reason lies in the desired evaporation of the contaminants by heat transfer and, therewith, the boiling and transfer to the gas phase.

For this purpose, an experimental investigation was conducted. The large scale remediation experiment was carried out in a container ( $81m^3$ ) of the *VEGAS* where an aquifer, overlaid with an aquitard and a vadose zone is rebuild. The contaminant recovery was achieved by soil vapour extraction technique, which was enhanced by steam injection into the saturated zone (aquifer) and the unsaturated zone (vadose zone), respectively. The two steam injection techniques, *steam override* and *steam sandwich* were investigated. Two steam injection (*SI*) wells into the saturated and the unsaturated zone, respectively, and two soil vapour extraction (*SVE*) wells were emplaced. Hydraulic and major material parameters of the used soil filling materials were determined during former experimental investigations (HIESTER & BAKER (2009) [19]). The steam injection into saturated zone (*steam override*) below the low permeable aquitard resulted in week-wise steam breakthrough conditions. The desired heating of the aquitard was realized.

After 29 days of *steam override*, steady state was reached, meeting the condition of exceeding the target temperature of about  $90^\circ\text{C}$  (reached after 16 days) at the top of the aquitard between the two injection wells. The target temperature was set to the given value as the azeotropic boiling point of a mixture consisting of tetrachloroethene and water is reached at around  $88^\circ\text{C}$ , ensuring vaporization. Further tests concerning additional steam injection into the vadose zone (*steam sandwich*) were conducted in order to investigate heat distribution and contaminant removal. The *sandwich-heating* resulted in only a limited expansion of heat in the unsaturated zone as a reason of the close distance between the injection wells and the soil vapour extraction wells. The *SVE* wells extracted the injected heat instantaneously and continuously. In addition, no increase in contaminant removal was observed, which argued for a successful remediation of the unsaturated zone. However, due to the fact that heat propagation was limited, an accumulation of contaminant in the unsaturated zone is possible. This assumption is supported by the measured high contaminant concentrations in the extracted condensate from the unsaturated zone



which were exceeding the aqueous equilibrium concentration of the gas phase. A total mass of about 3.0 kg of tetrachloroethene was removed at the end of the experiment after 66 days of duration. This corresponds to a removal percentage of about 46% of the previous estimated initial contaminant amount in the container by the soil vapour extraction and the groundwater. The *SVE* extracted 2.7 kg (88%) of the total contaminant mass, whereas the groundwater removed 0.3 kg (11%). 1 percent was removed with the extracted condensate from the unsaturated zone. The contaminant concentration in the soil vapour extraction decreased by 99%. In the groundwater outflow, the concentration decreased by 85% from the initial concentration of 1.8 to 0.36  $\frac{mg}{l}$ . The comparative high contaminant removal of the groundwater at the end of the experiment compared to the *SVE*, point to a persisting contamination of the saturated zone especially at the margins of the tank.

Closing the mass balance was found difficult since a vertical subsidence of the contaminant to the bottom of the tank since 2008 (LEUBE (2008) [24]) handicapped the contaminant removal. A complete remediation of the subsoil could not be achieved.

In conclusion, the experiment demonstrated applicability of the *steam override* method concerning heat distribution in low permeable layers and the remediation of contaminants from low permeable layers. The *steam sandwich* method can be applied to ensure a continuative remediation of the unsaturated zone and to increase the temperature at the top of the low permeable layer.

Former numerical or experimental investigations (GUIDRY (2010) [15]) predicted a non-compliance concerning the heating of the low permeable layer (aquitarde) and the simulated results using the present parameters. This suggests a higher hydraulic permeability than the one determined for the *M2* material used during packing the aquitarde formation. This assumption was confirmed by the numerical simulations. In addition, the fast increase of temperature observed in the low permeable layer and the unsaturated zone at the beginning of the steam injection suggests possible fractures in the low permeable layer resulting in preferred steam flow paths.

The comparison of the heat distribution of the one dimensional numerical model and the experiment yielded a strong deviation. The 1D model was not able to simulate the heat distribution correctly. The model was originally set up to simulate the heat distribution of the flume experiment (GUIDRY (2010) [15]) where heat convection played a major role in the heat distribution. In the tank experiment, however, heat conduction was the predominant process. At that time, the 1D model can not be applied for the dimensioning of field applications. Further investigations on the 1D model in order to enhance the simulation accuracy of the temperature development are suggested. This would involve the extension of the convective term based on the energy balance or the implementation of an advective term, respectively.

The second part of this work is the set-up of the two-phase, two-components, non-isothermal, numerical model set-up. The model was able to reproduce the

relevant processes for heat distribution in the low permeable layer. However, several shortcomings emerged during the set-up progress which have negative effects on the stability and prediction accuracy. Due to the fact that the model considers only two dimensions, a cross-section of the physical model was simulated in order to observe vertical heat distribution. The steam injection rates applied in the model were derived from the experiment. The developed approach has to be considered one of the main uncertainties when regarding reproduction accuracy. This is aggravated by the above mentioned incomplete knowledge concerning the hydraulic conductivity of the low permeable layer. During simulations, the conductivity was set to a value fitting the heat distribution. The fact that steam propagated as far as the walls of the container resulted in further problems reflected in the correct assignment of the boundary conditions and estimation of energy losses. Finally, vertical heat distribution was reproduced with a deviation of about one day faster considering the target temperature ( $90^{\circ}\text{C}$ ) at the top of the aquitard for the applied set of parameters. Hence, a change in soil parameters or steam injection flow rate, for example, may result in an incorrect reproduction of the heat distribution and may only give a rough estimation. For this reason, predictability of heat distribution for altered input parameters is disputable and has to be taken with caution.

The model set-up turned out to be very sensitive to changes in input parameters and, therefore, has to be considered a very soft model. Ideas for improvement are, for example, further investigations and a new calibration of the 2D model by means of a field application where a larger model domain can be simulated in order to avoid direct interactions with the boundaries. An increase in predictability of heat distribution and stability of the simulation could also be achieved by a more complex numerical model. A major improvement would be obtained by considering all three spatial dimensions. This would exclude the uncertainties induced by steam injection rate determination and provide the reproduction of a fully radial steam propagation. Furthermore, boundary conditions could be assigned correctly taking into account the actual soil vapour extraction well locations as well as the groundwater inlet and outlet. However, these advantages are accompanied by the construction of an extensive three-dimensional numerical grid and, therewith, a higher demand of computing power. The lavishness of the grid construction is ascribed to local refinements around the injection wells, necessary to increase reproduction accuracy and stability of the numerical model.

# Bibliography

- [1] *Dortmund Data Bank*. ([www.ddbst.com](http://www.ddbst.com)).
- [2] *United States Environmental Protection Agency: On-line Tools for Site Assessment Calculation*. ([www.epa.gov/athens/learn2model/part-two/onsite/](http://www.epa.gov/athens/learn2model/part-two/onsite/)).
- [3] *Risk Science Programm ;Intermedia Transport Factors for Contaminants Found at Hazardous Waste Sites: TETRACHLOROETHYLENE*. Technical Report, Department of Environmental Toxicology, University of California, 1994.
- [4] *In Situ Thermal Treatment of Chlorinated Solvents: Fundamentals and Field Applications*. Technical Report, U.S. Environmental Protection Agency, 2004.
- [5] BAEHR, H.D. and S. KABELAC: *Thermodynamik - Grundlagen und technische Anwendungen*. Springer Verlag, 2010.
- [6] BAEHR, H.D. and K. STEPHAN: *Wärme- und Stoffübertragung*. Springer Verlag, 2010.
- [7] BEAR, JACOB and ALEXANDER H.-D. CHENG: *Modeling Groundwater Flow and Contaminant Transport*. Springer Verlag, 2010.
- [8] BETZ, CHRISTOPH: *Wasserdampfdestillation von Schadstoffen im porösen Medium: Entwicklung einer thermischen In-Situ-Sanierungstechnologie*. PhD thesis, Universität Stuttgart, 1998.
- [9] BOUWER, HERMAN and R. C. RICE: *A Slug Test for Determining Hydraulic Conductivity of Unconfined Aquifers With Completely or Partially Penetrating Wells*. Water Resources Research, Vol. 12, No.3, 1976.
- [10] CLASS, H.: *Theorie und numerische Modellierung nichtisothermer Mehrphasenprozesse in NAPL-kontaminierten porösen Medien*. PhD thesis, Institut für Wasserbau, Universität Stuttgart, 2001.
- [11] CLASS, H., P. BASTIAN and R. HELMIG: *Numerical Simulation of Non-Isothermal Multiphase Multicomponent Processes in Porous Media. 1. An Efficient Solution Technique*. Advances in Water Resources, 25:533 – 550, 2002.
- [12] COOPER, HILTON H., JOHN D. BREDEHOEFT and ISTAVROS S. PAPADOPULOS: *Response of a Finite Diameter Well to an Instantaneous Charge of Water*. Water Resources Research, Vol. 3:263–269, 1967.

- [13] DAVIS, E. L.: *How Heat Can Enhance In Situ Soil and Aquifer Remediation: Important Chemical Properties and Guidance On Choosing the Appropriate Technique*. EPA, /540/S-97/502, 1997.
- [14] FÄRBER, ARNE: *Wärmetransport in der ungesättigten Bodenzone: Entwicklung einer thermischen in-situ Sanierungstechnologie*. PhD thesis, Institut für Wasserbau, Universität Stuttgart, 1997.
- [15] GUIDRY, ALINE M.: *Steam injection into saturated zone - Experimental investigation of thermal in-situ remediation of a CHC contamination (source zone) in low permeability zones using steam flow*. Master's thesis, University of Stuttgart, 2010.
- [16] HELMIG, R.: *Multiphase Flow and Transport Processes in the Subsurface*. Springer Verlag, 1997.
- [17] HELMIG, R., H. CLASS, R. HUBER, H. SHETA, R. EWING, R. HINKELMANN, H. JAKOBS and P. BASTIAN: *Architecture of the Modular Program System MUFTE-UG for Simulating Multiphase Flow and Transport Processes in Heterogeneous Porous Media*. *Mathematische Geologie*, 2:123–131, 1998.
- [18] HELMIG, R. and R.U. HUBER: *Comparison of Galerkin-type discretization techniques for two-phase flow in heterogeneous porous media*. *Advances in Water Resources* 21, 8:697–711, 1998.
- [19] HIESTER, U. and R. S. BAKER: *Large-Scale Physical Models of Thermal Remediation of DNAPL Source Zones in Aquitards*. SERDP Project ER-1423 Final Report, Vegas, Universitat Stuttgart. TerraTherm, Inc., Fitchburg, MA, 2009.
- [20] INGENIEURE, VEREIN DEUTSCHER (editor): *VDI-Wärmeatlas*. Springer, 2006.
- [21] KARICKHOFF, S. W.: *Semi-Empirical Estimation of Sorption of Hydrophobic Pollutants of Natural Water Sediments and Soils*. *Chemosphere*, 10(8):833–846, 1981.
- [22] KLINGINGER, CHRISTOPH: *Cyclic Steam Injection into the Subsurface - Solarthermal Steam Generation for Enhanced Oil Recovery*. Master's thesis, Institut für Wasserbau, Universität Stuttgart, 2010.
- [23] KRUSEMAN, G. P. and N. A. RIDDER: *Analysis and Evaluation of Pumping Test Data*. 2000.
- [24] LEUBE, PHILIPP: *Experimentelle Untersuchungen der Prozesse auf technischer Skala bei der In-Situ-Reinigung gering durchlässiger, gesättigter Böden mit festen Wärmequellen*. Master's thesis, Institut für Wasserbau, Universität Stuttgart, 2008.

- 
- [25] LIDE, DAVID R.: *Handbook of Chemistry and Physics*. Web Version hbcpnbase.com/, 2010/11.
- [26] OCHS, S., H. CLASS, A. FÄRBER and R. HELMIG: *Methods for Predicting the Spreading of Steam Below the Water Table During Subsurface Remediation*. Water Resources Research, 46, 2010.
- [27] OCHS, S.O., R.A. HODGES, R.W. FALTA, T.F. KMETZ, J.J. KUPAR, N.N. BROWN and D.L. PARKINSON: *Predicted Heating Patterns During Steam Flooding of Coastal Plain Sediments at the Savannah River Site*. Environmental & Engineering Geoscience, 1:51–69, 2003.
- [28] OCHS, STEFFEN OLIVER: *Steam injection into saturated porous media - process analysis including experimental and numerical investigations*. PhD thesis, Institut für Wasserbau, Universität Stuttgart, 2007.
- [29] REID, R.C., J.M. PRAUSNITZ and B.E. POLING: *The Properties of Gases and Liquids*. McGraw-Hill Book Company, 1987.
- [30] SCHNEIDER, J. P.: *Conduction Heat Transfer*. Addison-Wesley Pub. Co., 1955.
- [31] SOMERTON, W.H., A.H. EL-SHAARANI and S.M. MOBARAK: *High temperature behaviour of rocks associated with geothermal type reservoirs*. Society of Petroleum Engineers, 1974.
- [32] TRÖTSCHLER, OLIVER, KAROLIN WEBER and HANS-PETER KOSCHITZKY: *Simultaneous Remediation of the Saturated and Unsaturated Zones by Steam-Air Injection and Alcohol Flushing*. Technical Report, Institut für Wasserbau, Universität Stuttgart, 2004.



# A PCE Concentrations

## A.1 Groundwater and FLS1 Samples

Time [d]	Groundwater		FLS1	
	PCE [ $\mu\text{g/l}$ ]	TCE [ $\mu\text{g/l}$ ]	PCE [ $\mu\text{g/l}$ ]	TCE [ $\mu\text{g/l}$ ]
-47.0	1810	< 1	-	-
-42.2	1821	< 1	-	-
-35.2	1755	< 1	-	-
-32.2	1925	< 1	-	-
-28.2	2554	1	-	-
-25.2	2720	3	-	-
-21.2	3318	2	19	< 1
-18.2	1859	1	4	< 1
-14.2	1211	1	2	< 1
-11.2	1089	< 1	1	< 1
-7.2	1397	< 1	1	< 1
-4.2	1638	< 1	1	< 1
-0.2	1799	< 1	20	< 1
0.8	2403	< 1	20	< 1
2.8	3290	2	6	< 1
4.8	2697	3	845	1
6.8	1552	2	1831	1
9.8	1207	3	520	< 1
13.8	921	3	1515	< 1
16.8	766	3	1400	< 1
19.8	667	2	1101	< 1
23.8	702	3	1685	1
27.8	667	4	1451	1
30.8	860	8	415	< 1
34.8	576	7	312	< 2
37.8	482	6	223	< 3
41.8	507	7	214	< 4
44.8	480	10	129	< 5
48.8	375	8	155	< 6
50.8	475	11	187	< 7
52.8	426	13	143	< 8
55.8	427	17	117	< 9
57.8	362	15	108	< 10
59.8	422	18	93	< 11
64.8	400	87	290	< 12
65.8	387	21	11	< 13





## A.2 Concentration Comparison of SVE and FLS1

Henry Coefficient of PCE (20°C):

**0.579**

Time	Concentration Gas Phase	Equilibrium Concentration (Aqueous Phase)	FLS1
[d]	[mg/m <sup>3</sup> ]	[mg/m <sup>3</sup> ]	[mg/m <sup>3</sup> ]
4.8	145	84	845
6.8	165	96	1831
9.8	91	53	520
13.8	68	39	1515
16.8	28	16	1400
19.8	22	13	1101
23.8	16	9	1685
27.8	14	8	1451
30.8	13	7	415
34.8	14	8	312
37.8	11	6	223
41.8	22	13	214
44.8	10	6	129
48.8	17	10	155
50.8	22	13	187
52.8	23	13	143
55.8	20	11	117
57.8	19	11	108
59.8	17	10	93
62.8	12	7	49
64.8	2	1	290



## B Slugtest Data

### Injection Well I1

Drawdown [m]	Time [s]
0.00	0
0.04	1
0.14	2
0.25	3
0.34	4
0.43	5
0.51	6
0.59	7
0.67	8
0.74	9
0.80	10
0.87	11
0.92	12
0.97	13
1.02	14
1.07	15
1.10	16
1.14	17
1.18	18
1.20	19
1.24	20
1.27	21
1.29	22
1.32	23
1.35	24
1.37	25
1.39	26
1.40	27
1.42	28
1.43	29
1.45	30
1.46	31
1.47	32
1.49	33
1.50	34
1.51	35
1.52	36
1.53	37
1.54	38
1.55	39
1.56	40
1.56	41
1.56	42
1.57	43
1.58	44
1.58	45
1.59	46
1.60	47
1.60	48
1.61	49
1.61	50
1.62	51
1.63	52
1.63	53

Drawdown [m]	Time [s]
1.63	54
1.63	55
1.64	56
1.64	57
1.65	58
1.65	59
1.65	60
1.65	61
1.66	62
1.66	63
1.66	64
1.66	65
1.66	66
1.67	67
1.66	68
1.66	69
1.67	70
1.67	71
1.67	72
1.67	73
1.67	74
1.67	75
1.67	76
1.68	77
1.67	78
1.67	79
1.68	80
1.67	81
1.67	82
1.68	83
1.68	84
1.68	85
1.68	86
1.67	87
1.68	88
1.68	89
1.68	90
1.68	91
1.69	92
1.68	93
1.68	94
1.68	95
1.68	96
1.68	97
1.68	98
1.68	99
1.68	100
1.68	101
1.69	102
1.68	103
1.69	104
1.68	105
1.69	106
1.69	107

**Injection Well I2**

Drawdown [m]	Time [s]
0.00	0
0.00	1
0.04	2
0.12	3
0.19	4
0.24	5
0.30	6
0.36	7
0.41	8
0.45	9
0.51	10
0.55	11
0.59	12
0.63	13
0.67	14
0.71	15
0.75	16
0.78	17
0.82	18
0.84	19
0.87	20
0.90	21
0.93	22
0.96	23
0.98	24
1.00	25
1.02	26
1.05	27
1.07	28
1.09	29
1.11	30
1.13	31
1.15	32
1.16	33
1.17	34
1.20	35
1.20	36
1.22	37
1.23	38
1.25	39
1.26	40
1.27	41
1.28	42
1.29	43
1.30	44
1.31	45
1.32	46
1.33	47
1.34	48
1.35	49
1.35	50
1.36	51
1.37	52
1.38	53

Drawdown [m]	Time [s]
1.39	54
1.39	55
1.40	56
1.40	57
1.41	58
1.42	59
1.42	60
1.43	61
1.44	62
1.44	63
1.45	64
1.45	65
1.45	66
1.46	67
1.47	68
1.47	69
1.48	70
1.48	71
1.48	72
1.48	73
1.49	74
1.49	75
1.50	76
1.49	77
1.50	78
1.50	79
1.50	80
1.51	81
1.51	82
1.52	83
1.52	84
1.52	85
1.52	86
1.53	87
1.53	88
1.53	89
1.54	90
1.54	91
1.55	92
1.55	93
1.54	94
1.55	95
1.55	96
1.56	97
1.56	98
1.56	99
1.56	100
1.56	101
1.56	102
1.56	103
1.56	104
1.56	105
1.57	106
1.57	107

Drawdown [m]	Time [s]
1.58	108
1.57	109
1.57	110
1.57	111
1.57	112
1.57	113
1.58	114
1.58	115
1.58	116
1.58	117
1.58	118
1.58	119
1.58	120
1.58	121
1.58	122
1.58	123
1.58	124
1.59	125
1.58	126
1.58	127
1.58	128
1.58	129
1.59	130
1.59	131
1.59	132
1.59	133
1.59	134
1.59	135
1.59	136
1.59	137
1.59	138
1.59	139
1.59	140
1.60	141
1.59	142
1.59	143
1.59	144
1.59	145
1.59	146
1.59	147
1.60	148
1.59	149
1.59	150
1.60	151
1.60	152
1.60	153
1.59	154
1.60	155
1.60	156
1.60	157
1.60	158
1.60	159
1.60	160
1.60	161